

# SHAPING SINGLE PHOTONS

PETER NISBET-JONES  
ST. JOHN'S COLLEGE

---

A thesis submitted in partial fulfilment of  
the requirements of the degree of  
Doctor of Philosophy at the University of Oxford



Clarendon Laboratory  
Supervisor: Axel Kuhn  
February 2012



# SHAPING SINGLE PHOTONS

PETER NISBET-JONES

D.PHIL, HILARY 2012

ST. JOHN'S COLLEGE

---

The possibility of creating a scaleable quantum network by interconverting photonic and atomic qubits shows great promise. The fundamental requirement for such a network is deterministic control over the emission and absorption of photons from single atoms. This thesis reports on the experimental construction of a photon source that can emit single-photons with arbitrary spatio-temporal shape, phase, and frequency.

The photon source itself is a strongly-coupled atom cavity system based on a single  $^{87}\text{Rb}$  atom within a macroscopic high-finesse Fabry-Perot cavity. It operates intermittently for periods of up to  $100\ \mu\text{s}$ , with single-photon repetition rates of 1.0 MHz and an efficiency of almost 80%. Atoms are loaded into the cavity using an atomic fountain, with the upper turning point near the centre of the cavity mode. This ensures long interaction times without any disturbances introduced by trapping potentials. The photons' indistinguishability was tested, with a two-photon Hong-Ou-Mandel visibility of 87%.

This ability to both generate, and control, the photons' properties, for example producing photons with symmetric or multi-peaked spatio-temporal shapes, allows for the production of photons in an  $n$ -time-bin superposition state where each time-bin has an arbitrarily defined amplitude and phase. These photons can be used as photonic qubits, qutrits and qquads, and their properties have been tested using a small linear-optics network.



## ACKNOWLEDGMENTS

---

Before I begin I would like to take the opportunity for a few notes of thanks. First, Dr. Axel Kuhn for his guidance and support, to the EPSRC and St. John's College for all the financial support that I have received, and to Jerome Dilley, we started with an empty room and built everything from scratch; this thesis would not have been possible without them. I would also like to thank the innumerable people who have provided ideas and help and kept me sane. Finally - and most importantly - I would like to thank my wife.

## PUBLICATIONS

---

- [1] Himsworth, M., Nisbet, P., Dilley, J., Langfahl-Klabes, G. & Kuhn, A. EIT-based quantum memory for single photons from cavity-QED. *Appl. Phys. B* **103**, 579 (2011).
- [2] Nisbet-Jones, P. B. R., Dilley, J., Ljunggren, D. & Kuhn, A. Highly efficient source for indistinguishable single photons of controlled shape. *New J. Phys.* **13**, 3036 (2011).
- [3] Dilley, J., Nisbet-Jones, P., Shore, B. W. & Kuhn, A. Single-photon absorption in coupled atom-cavity systems. *Phys Rev A* **85**, 023834 (2012).
- [4] Nisbet-Jones, P. B. R., Dilley, J., Holleczek, A., Barter, O. & Kuhn, A. Quantum Homodyning of Photonic Qubits, Qutrits and Ququads Emitted on Demand from an Atomic Source. *arXiv* **quant-ph**, 1203.5614v1 (2012).



## CONTENTS

---

1	INTRODUCTION	1
1.1	Why do We Care?	1
1.2	A Single Photon Pistol	6
I A DETERMINISTIC SOURCE OF SINGLE PHOTONS		11
2	THE EXPERIMENTAL SETUP	13
2.1	The Cavity	14
2.2	Atom-Cavity Parameters	22
2.3	Cavity Stabilization	24
2.4	Atoms	29
2.5	Putting it all together	33
2.6	Conclusion	41
3	PHOTONS	43
3.1	Experimental Optimization	44
3.2	Photons	50
3.3	Photon Statistics	50
3.4	Conditioning	57
3.5	Photon Production Efficiency	60
3.6	Hong-Ou-Mandel Interferometry	66
3.7	Conclusion	76
II MAKING THESE PHOTONS DO SLIGHTLY ODD THINGS		79
4	CONTROLLING A PHOTON'S AMPLITUDE	81
4.1	Calculating a STIRAP Pulse	81
4.2	Numerical Simulation of Rubidium	87
4.3	Variations from the Fountain	92
4.4	Photon Shapes from Well Coupled Atoms	97
4.5	A Gallery of Single Photons	101
4.6	Conclusion	104
5	CONTROLLING THE FREQUENCY AND PHASE	107
5.1	Time-Resolved Hong-Ou-Mandel Interference	107
5.2	A Twin-Peak Photon	113
5.3	Changing a Photon's Frequency	114
5.4	Changing a Photon's Phase	118
5.5	Arbitrary Qubit Preparation	122
5.6	Experimentally Realizable Circuits	131
5.7	Conclusion	136
6	CONCLUSIONS AND OUTLOOK	139
6.1	Outlook	140
BIBLIOGRAPHY		145

## ACRONYMS

---

AOM	Acousto-Optical Modulator
APD	Avalanche Photo-Diode
AWG	Arbitrary Waveform Generator
FSR	Free Spectral Range
FWHM	Full Width Half Maximum
HOM	Hong-Ou-Mandel
LIAD	Light Induced Atomic Desorption
LOQC	Linear Optical Quantum Computing
MOT	Magneto-Optical Trap
PDH	Pound-Drever-Hall
PID	Proportional-Integral-Differential
PBS	Polarising Beam-Splitter
QC	Quantum Computing
QIP	Quantum Information Processing
QM	Quantum Mechanics
SH	Sample and Hold
SPCM	Single Photon Counting Modules
STIRAP	Stimulated Raman Adiabatic Passage
TDC	Time-Digital Converter
TEM	Transverse Electro-Magnetic mode
UHV	Ultra High Vacuum

## INTRODUCTION

---

### 1.1 WHY DO WE CARE?

The Gedanken experiments of Einstein and Bohr [1], which form the basis of much of Quantum Mechanics, were for many years thought to be exactly that, Gedanken. It was assumed that we would never be able to see single quantum particles such as atoms and photons, let alone manipulate and experiment upon them at will. Technological advances in the last few decades however have managed to make these experiments commonplace for many quantum particles, for example single atoms [2–4], ions [5, 6], electrons [7, 8] and even single photons [9, 10].

As the predictions of Quantum Mechanics (QM) seem to be at odds with the Classical world [11, 12] many people have tried to reconcile the two, in particular the apparent non-locality of entangled states [13–15]. However recent experimental work has shown that fundamental particles do indeed behave in this non-intuitive way [16–18]. Having determined QM’s veracity at the level of single quanta the next challenge is to try to scale this up, slowly increasing the number of particles - whilst keeping the control that we already have - to explore the Quantum-Classical Boundary [19–21]. It was through trying to understand the apparent contradictions of QM, and in particular the phenomenon of entanglement, that it was realised that there existed the possibility to exploit these unusual behaviours for practical

purposes; two of the most powerful ideas have been Quantum Cryptography (QC) [22] and Quantum Information Processing (QIP) [23, 24].

Due to the ability of quantum systems to exist in a superposition of many different states, it is possible for a Quantum computer to solve certain types of problems exponentially faster than a classical computer, scaling with increased size at a rate of  $2^N$  rather than the classical scaling of  $2N$ . The most famous of these problems are the Deutsch-Jozsa (constant/balanced) [25], Grover (database search) [26, 27], and Shor (prime factorisation) [28] algorithms, and it has also been shown that it is possible to create a universal computer [29, 30]. In addition to the dream of a full Quantum computer, an interesting subset is the idea of quantum simulations, where instead of calculating the solutions to a particular problem one creates an entirely different system - over which there is complete control - which displays the same dynamics as the initial problem [31–33]. By studying the controllable system we can then hope to gain insight to the more complex system. Recent experiments have simulated relativistic quantum effects using trapped ions [34–36] and it is thought that using these techniques might allow us to simulate large quantum systems which quickly become intractable using classical computers.

There are many quantum systems which can be used for QIP - indeed any two-level quantum system can be thought of as a qubit, the quantum generalization of a classical bit. The general criteria for a useful system of qubits was laid out by DiVincenzo [37]: the system must be scaleable, initializeable, have a long coherence time, allow universal computations and each qubit must be measurable. Whilst no perfect qubit has yet been made, current research is being conducted in many systems including Rydberg atoms [38–42], quantum dots [43–47], superconducting circuits [48–52], and nitrogen

vacancy centres in diamond [53–56]. The two most advanced technologies however involve trapped atoms/ions and single photons.

Single photons have proved extremely successful in quantum communication, transferring quantum information over 144 km in free space [57, 58] and violating Bell’s inequalities, [16, 59, 60] and distributing quantum keys over 122 km in standard telecom fibre [61–63]. Recently, thanks to the Linear-Optics-Quantum-Computation (LOQC) scheme [64–68] which relies only on linear optics such as beam-splitters and wave-plates, along with projective measurements, photonic qubits and gates have been manipulated and produced [69–73] and quantum factorisation algorithms have been demonstrated [74, 75].

Atomic qubits have also provided some compelling demonstrations of quantum interactions, where entanglement has been shown in neutral atoms [76, 77] and chains of up to 14 ions [78–80]. Building on the proposal for ion-trap quantum gates [81], C-NOT and phase gates have been created [82, 83], and calculations performed [84] with large scale systems [85].

Having now described some of the things that have been done using both atomic and photonic qubits the natural question that springs to mind is ‘Why do we need yet *another* one?’ The answer to this is simple - we don’t - what we actually need is a way to get the systems that we currently have to talk to one another. Imagine we own a futuristic universal atomic quantum computer. We perform a calculation - a result is found - and this result is stored in the internal state of a particular atom. We would now like to give this atom to one of our colleagues, who just happens to own an identical quantum computer, and what is more not only do they have this computer in the same room as ours they have very conveniently put it inside the same vacuum chamber as our own. It cannot be done. The atomic qubits can only be transferred between two atoms which are being held in the same trap

[86, 87]; to transfer an atomic state between isolated traps one must turn to another information carrier - photons [88].

So now let us take a look at photonic qubits. Photons are great for quantum communication as you do not need any special apparatus to transmit them - just point your emitter in the direction that you want to send the quantum information and off it goes [58]. Unfortunately the reasons for this simplicity (photons move at the speed of light and are only weakly interacting) are also photonics qubits' greatest downfalls: computation is probabilistic [64] and the maximum time for which a qubit can be stored [89, 90] is six orders of magnitude less than can be achieved with atoms [91].

What we would like to have is a technique to deterministically interconvert the atomic and photonic qubits. If we owned such a device the task of creating a scaleable quantum computer would be simplified as one could then use the best features of both systems whilst minimising their problems.

#### 1.1.1 *Using Cavity-QED*

The processes of stimulated and spontaneous emission are usually thought of as two distinct phenomena. The theory of Quantum-Electrodynamics (QED) [92] shows that they are actually the same effect, the seemingly stochastic spontaneous emission is simply the result of a stimulated emission by vacuum fluctuations of the quantized electromagnetic field. It was discovered by Purcell [93] (and then formalized for the interaction of a single atom in the Jaynes Cummings Model [94]) that this interaction with the vacuum is not fixed but is instead dependent on the number of electro-magnetic modes with which the atom is interacting. This logically led to the idea that if one vacuum interaction was engineered to be significantly dominant over the rest,

for example using a resonant cavity, it would be possible to cause an atom to coherently interact with that mode [95–97].

In their seminal paper [98] Cirac *et al.* proposed a quantum network consisting of a mixture of static nodes (an atom in a cavity) and photonic ‘flying-qubits’. As the vacuum stimulated emission process is coherent, it is possible to use these photons to distribute a quantum state through a quantum network. The arbitrary initial internal state of an atom is coherently transferred to a photon, this photon then leaks out of the cavity, propagates along a transmission line to another atom in another cavity, and then in a time-reversed counterpart of the emission process can be mapped onto the quantum state of the second atom. This has been expanded into the idea of a ‘quantum internet’ of distributed quantum systems [99], where QIP tasks can be performed on the static nodes [100–102] and qubits distributed around the network using photons.

The first experimental demonstration of a deterministic C-QED photon source only occurred in 2002 [103] and following this there has been rapid progress of the field, with photons being emitted from atoms trapped in dipole traps for up to 30 seconds [104–106] and indefinitely in ion traps [107]. Cavity based trapping [108, 109] and cooling [110, 111] techniques have also been demonstrated. The photons, which can have a controlled polarisation [112], are characterised using two-photon interference [113–115]. Of particular interest for applications in QIP have been the demonstrations of the state-mapping of an atomic to photonic qubit [116] and the storage of arbitrary states of light (so far limited to weak coherent pulses) using the desired time-reversed emission process [117, 118]. A complete review of cavity-based photon sources can be found in Kuhn *et al.* [119].

## 1.2 A SINGLE PHOTON PISTOL

The deterministic coupling of a single atom to a single photon relies on a vacuum-Raman transition in a three level  $\lambda$ -type system shown in Figure 1.1. In our experiment this is formed using the two hyperfine ground states of  $^{87}\text{Rb}$  along with the  $F' = 1$  excited state. The ground state  $|u\rangle$  is coupled to the excited state  $|x\rangle$  via an electric-dipole interaction with a laser pulse of Rabi frequency  $\Omega(t)$ , and the other ground state  $|g\rangle$  is coupled to the same excited state via the electric-dipole of the vacuum mode of a Fabry-Perot cavity,  $g$ . The cavity population is described by the state  $|n\rangle$  and thus the combined atom-cavity system can be written as the set of product states  $|i, n\rangle$  where  $i \in \{u, x, g\}$ .

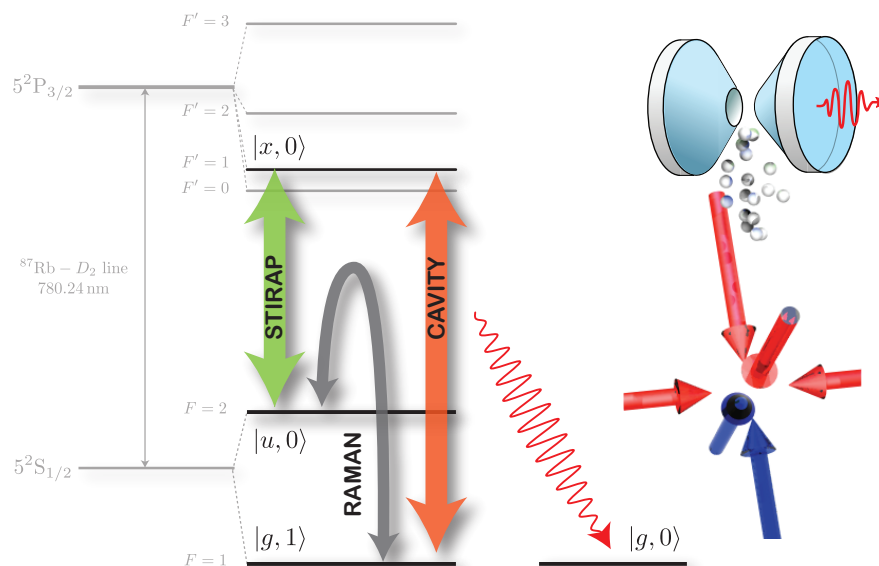


Figure 1.1: The concept of a single photon pistol: A single  $^{87}\text{Rb}$  atom is placed inside a high-finesse cavity using an atomic fountain. A coherent Raman transition is then driven within this atom by the vacuum field of the cavity and an external laser pulse. This transition produces a single photon which is subsequently emitted from the cavity.

To produce a photon, the system is initialised in the ground state  $|u, 0\rangle$  and driven by the laser on the  $|u\rangle \rightarrow |x\rangle$  transition - this leaves the intra-cavity photon number  $|n\rangle$  unchanged. Meanwhile, as the cavity is also resonant with the state  $|x\rangle$  it pumps the atom to the state  $|g\rangle$  and in doing so a single photon is produced in the cavity mode  $|n\rangle = |1\rangle$ . There exists an eigenstate of this interaction in which the excited state  $|x, 0\rangle$  does not appear and the system is coherently transferred from  $|u, 0\rangle$  to  $|g, 1\rangle$ ,

$$|\phi_1^0\rangle \propto \frac{2g|u, 0\rangle - \Omega(t)|g, 1\rangle}{\sqrt{4g^2 + \Omega^2(t)}} \quad (1.1)$$

where  $g$  is the atom-cavity interaction and  $\Omega(t)$  is the Rabi of the laser pulse. This ‘dark’ eigenstate (so called because it cannot fluoresce) can be used to coherently transfer population from  $|u, 0\rangle$  to  $|g, 1\rangle$  via a stimulated Raman transition[97]. The system starts with all of the population in the state  $|u, 0\rangle$  and provided that the pump pulse rises slowly, the population will be coherently transferred to the state  $|g, 1\rangle$ , placing a photon in the cavity mode. Once the system has been transferred to the state  $|g, 1\rangle$  the finite cavity decay causes the photon to be emitted from the cavity, leaving the atom in the state  $|g, 0\rangle$  where it is decoupled from further evolution. A full discussion of the theory can be found in Kuhn et al.[120].

The only dynamic variables in the entire system are the Rabi frequency of the driving laser  $\Omega(t)$  and the populations of the states (and hence the photon’s spatio-temporal envelope as this is proportional to the state  $|g, 1\rangle$ ). If this Rabi frequency changes then the photon must change in turn; it is this fact that will be utilised throughout this thesis to demonstrate control over single photons.

The most pressing experimental requirement for this process to occur is to have the atom-cavity system in the strong coupling regime - i.e. that the coherent interaction with the cavity mode dominates over the incoherent

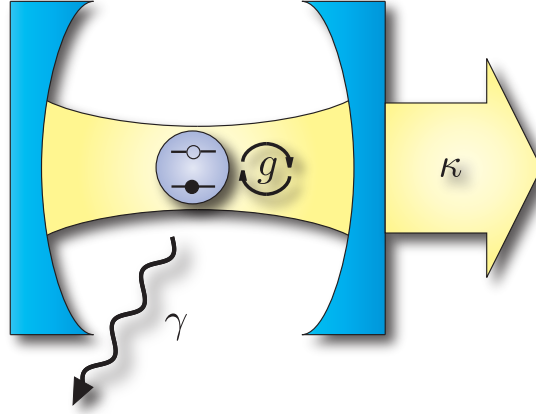


Figure 1.2: Coupling in C-QED: An atom-cavity system experiences three coupling rates:  $g$  the exchange of excitation between the atom and the cavity,  $\kappa$  the decay of the cavity field, and  $\gamma$  the decay of the atomic amplitude.

decay. This behaviour is governed via three parameters: the free space decay  $\gamma$ , the cavity decay  $\kappa$ , and the interaction between the atom with the vacuum mode of the cavity given by

$$g_0 = \frac{\mathbf{d} \cdot \mathbf{E}}{\hbar} = \sqrt{\frac{d^2 \omega_0}{2\hbar \epsilon_0 V}}, \quad (1.2)$$

where  $d$  is the electric-dipole moment of the transition,  $E$  is the electric field of the cavity mode,  $\omega_0$  is the transition frequency and  $V$  is the volume of the cavity mode. To be in the strong-coupling regime this atom-cavity interaction must dominate the two decay rates,  $g_0 \gg \kappa\gamma$ , and is more formally defined by the atom-cavity co-operativity being greater than 1.

$$C = \frac{g^2}{2\kappa\gamma} > 1 \quad (1.3)$$

### 1.2.1 *Thesis Summary*

This thesis describes the design, construction and subsequent utilisation of a cavity-based single photon source to produce photons of defined shape, frequency and phase. In Part [i](#) the construction and initial characterisation of the photon source is presented. This consists of [Chapter 2](#) where the construction of the required optical cavity, atom trap and lasers is described, and [Chapter 3](#) where the production and characterisation of single photons is shown. The photon statistics, which demonstrate that the source acts as a single-photon emitter, are presented along with a measurement of the efficiency of the source. Using two-photon interference we also examine the indistinguishability of the emitted photons. In Part [ii](#) we present control over the emitted photons. The production of photons with an arbitrarily defined spatio-temporal amplitude - i.e. physical shape, is demonstrated in [Chapter 4](#), and in [Chapter 5](#) control over the photons' frequency and phase is shown. This can be thought of as a form of arbitrary qubit generation. Finally an outlook for future experiments is presented in [Chapter 6](#).



## Part I

### A DETERMINISTIC SOURCE OF SINGLE PHOTONS

In the following chapters the design, construction and characterisation of a deterministic single-photon source is presented. The source, which is based on a single atom being driven through a vacuum-STIRAP transition within a high finesse Fabry-Perot cavity, exhibits high efficiencies and sub-Poissonian statistics. The emitted photons are also found to be indistinguishable.



## THE EXPERIMENTAL SETUP

---

Although it can take a while to build, the heart of any C-QED experiment is simple: a single atom sitting between two mirrors. Comparing this to many other physics experiments it is quite basic, yet it is a versatile tool for studying quantum interactions.

The cavity (Figure 2.1) is formed from two highly reflective dielectric mirrors glued to shear piezo crystals. It features great simplicity of construction and also has the advantages of good optical access and high mechanical stability. Single  $^{87}\text{Rb}$  atoms are probabilistically loaded into the cavity using an atomic fountain; the atoms are captured and cooled to a few  $\mu\text{K}$  in a Magneto-Optical Trap (MOT) located approximately 8 mm below the cavity, and then launched towards it using a moving molasses technique.

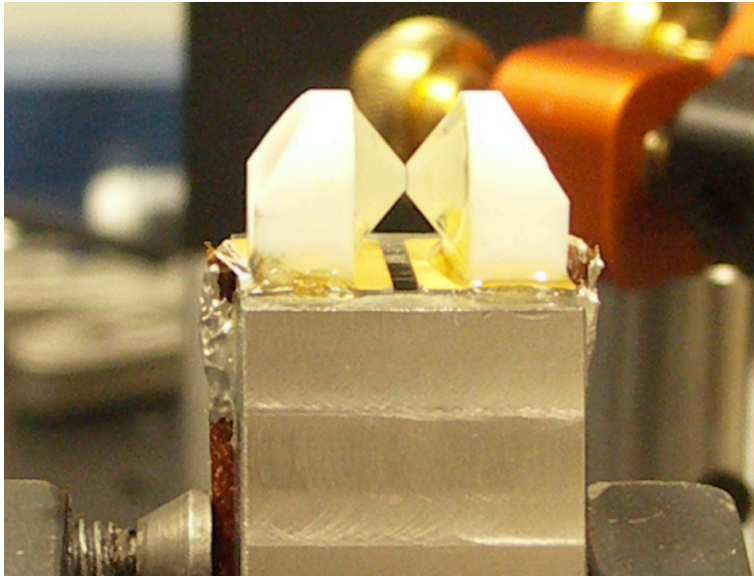


Figure 2.1: The high-finesse cavity before it was incorporated into the vacuum system.

The design, construction and characterisation of the cavity is discussed in Section 2.1, which allows us to calculate the atom-cavity parameters in Section 2.2. The required stabilisation of the cavity is described in Section 2.3. The loading and launching of  $^{87}\text{Rb}$  atom is discussed in Section 2.4. Finally, in Section 2.5 the experimental arrangement as a whole is summarised.

## 2.1 THE CAVITY

### 2.1.1 Mirrors

The cavity required for a single photon source relies on two properties which are not obviously compatible. Firstly, to ensure that the system can evolve via the coherent ‘dark’ state (Section 1.2) the interaction must take place in the strong-coupling regime ( $g > \{\kappa, \gamma\}$ ), which requires mirrors with the highest possible reflectivity. Secondly we would like a high photon out-coupling probability into a single mode, which requires mirrors with a low reflectivity. This conflict can be overcome by using a pair of asymmetric mirrors as if one of the mirrors has a significantly larger transmission than the other then it is through this mirror that any light within the cavity mode will preferentially leak out, thus doubling the photon collection probability. Although this does entail a reduction in the cavity’s finesse, with mirror reflectivities at the part-per-billion level it is possible to remain in the strong-coupling regime whilst obtaining out-coupling into a single mode of  $> 95\%$ . As the cavity linewidth, and thus the co-operativity, of the system is dependent only on the mean reflectivity of the two mirrors, it is unaffected by the asymmetry.

Plots of the photon emission probability and atom-cavity co-operativity are shown in Figure 2.2. It can be seen that if we have cavity mirrors with transmissions of  $T_1 = 1$  ppm, and  $T_2$  as a few tens of ppm, we can remain in

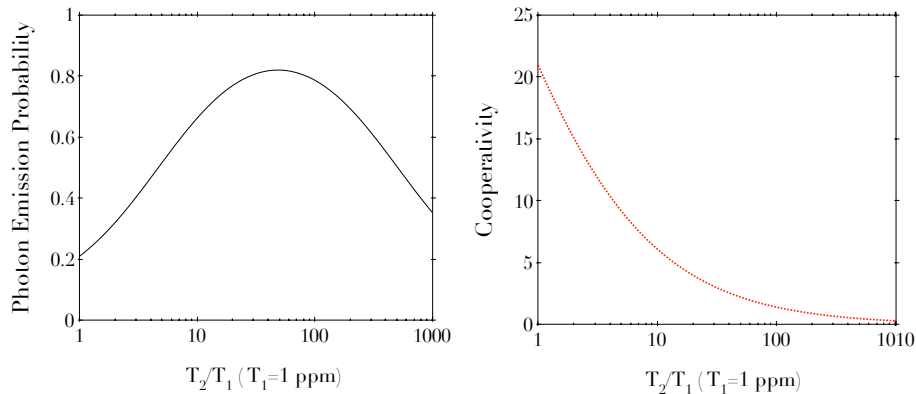


Figure 2.2: The effect of changing the cavity transmission  $T = \sqrt{T_1 T_2}$  on the photon emission probability,  $P_E = \frac{T_1}{T_1 + T_2 + 2l} \left( \frac{g^2}{g^2 + \kappa\gamma} \right)$ , and the cooperativity for an asymmetric Fabry-Perot cavity. We assume that one mirror ( $T_1$ ) is as good as technically possible (1 ppm) and seek the optimum transmission of the other mirror. The values of  $g, \kappa, \gamma$  are taken from this experiment and provide technical, but not fundamental, limits to the photon emission.

the strong-coupling regime and obtain a total emission probability (photon creation and emission) of  $P_E \approx 80\%$ .

#### 2.1.1.1 Cavity Design

The cavity design is similar to those used by the Meschede [4] and Kimble [104] groups (Figure 2.3). The high reflectivity mirrors are aligned in free space with a separation of about  $75 \mu\text{m}$  and held together with vacuum compatible epoxy. Fine adjustments of the resonator length (Section 2.3.1) were achieved using a shear piezo actuator.

The mirrors were manufactured by Research-Electro-Optics Inc in Boulder, Colorado. They consist of a cylindrical substrate of BK7 glass with a diameter of  $\varnothing = 7.75 \text{ mm}$  and a depth of  $d = 4 \text{ mm}$ . The front face is polished to give a spherically concave surface with a radius of curvature of  $R_c = 5 \text{ cm}$  and surface roughness of  $\lambda/20$ ; the rear surface of the substrate is flat. A dielectric reflective coating is deposited on the front face of both mirrors and

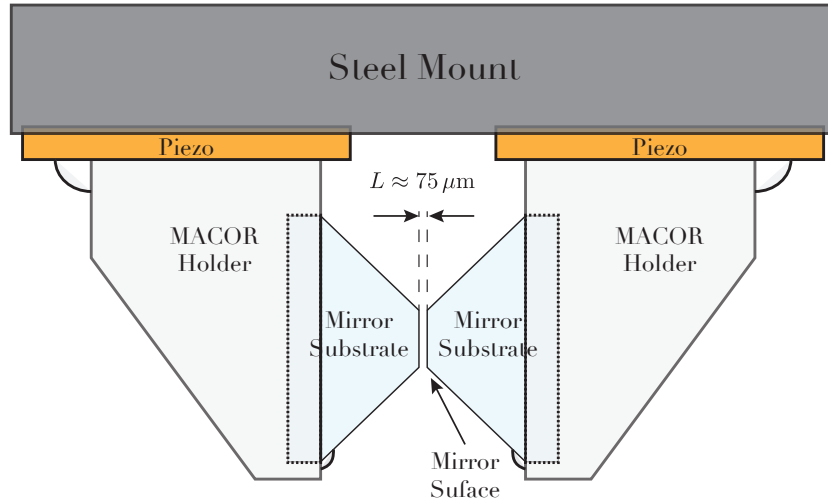


Figure 2.3: A schematic diagram of the high finesse cavity

an anti-reflective coating on the rear of the lower reflectivity out-coupling mirror. The mirrors were then machined down to a truncated cone with a mirror surface diameter of  $\varnothing = 1 \text{ mm}$  by Hellma Optics GmbH. This coning serves two purposes. Firstly, it allows for a much smaller cavity volume and hence greater  $g_0$  (Section 2.2); with a 5 cm radius of curvature the center of the unconed mirror lies  $150 \mu\text{m}$  below the mirror's outer rim (the sag height), resulting in a minimum cavity length of twice this,  $L = 300 \mu\text{m}$ . By coning the mirrors to  $\varnothing = 1 \text{ mm}$  the sag height is reduced to  $2.5 \mu\text{m}$  and we can achieve a  $< 100 \mu\text{m}$  cavity length. Secondly this coning allows us to form a MOT much closer to the cavity mode without scattering a lot of light off the mirrors (Figure 2.13). Although reducing the MOT-cavity distance makes no difference to the atom-cavity interaction time, it means that any deviation from a perfectly vertical launch is less important.

The mirrors are mounted in ceramic holders (MACOR) and then affixed to shear piezo crystals (*Noliac CSAP03*) which give a  $1.5 \mu\text{m}$  stroke at  $\pm 320 \text{ V}$ , sufficient travel to use each piezo to scan over a free spectral range.

The actuators were electrically contacted to the cavity mount via their bottom surfaces using an conductive epoxy (*Epotek-H20E*), providing the ground point for the battery powered locking electronics; the top surfaces are connected to the control electronics via a vacuum feedthrough and Kapton wire. It was originally intended to use the two piezos independently, a high voltage offset would be applied to one, and the locking modulation (Section 2.3.1) would then be applied to the other. Unfortunately, during the vacuum system bakeout one of the piezos developed an electrical short; however the inbuilt redundancy of the design allowed us to apply both signals to the remaining piezo actuator.

The cavity mount is a solid non-magnetic steel block which locates the cavity in the center of the vacuum chamber. The mounting block was bolted directly to the vacuum chamber, which was in turn bolted to the laser table. There is no further vibration damping or isolation as it was not found to be necessary (Section 2.3.2).

### 2.1.2 Cavity Characterization

The cavity spectrum, which can be interrogated using the experimental setup shown in Figure 2.4, is easily understood using simple ray tracing

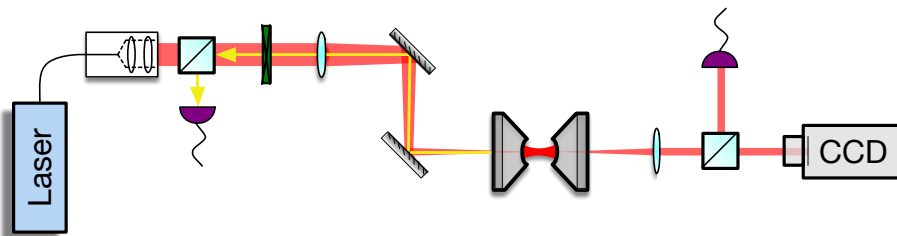


Figure 2.4: Cavity characterisation optics: The cavity resonance is probed with a mode-matched laser and the transmission and reflection spectra are observed. The output is split using a 50/50 beam-splitter to monitor the transmitted power (amplified photodiode) and a mode structure (CCD).

between the mirrors. Two lossless mirrors, with electric field reflectivities and transmissions,  $\sqrt{R_1}, \sqrt{T_1}$  and  $\sqrt{R_2}, \sqrt{T_2}$ , are separated by a distance  $L$ . A laser beam with field amplitude  $E_0$  incident on the first mirror will be partially reflected or transmitted with the fractions  $E_0\sqrt{R_1}$ , and  $E_0\sqrt{T_1}$  and this splitting will continue each time the beam hits a mirror. As the laser is a coherent beam (assuming  $\infty$  coherence length) the total beam power on reflection or transmission is simply the sum of all the beam fractions with the relevant integer multiple of the round trip phase  $\phi = 2L\frac{2\pi}{\lambda} = 2L\frac{\omega}{c}$ . By defining  $T = \sqrt{T_1}\sqrt{T_2}$  and  $R = \sqrt{R_1}\sqrt{R_2}$ , and using the infinite sum of a geometric series  $1 + x + x^2 + x^3 + \dots = \frac{1}{1-x}$ , this can be written as,

$$\begin{aligned} E_R &= E_0(-\sqrt{R_1} + T_1\sqrt{R_2}e^{i\phi} + T_1R\sqrt{R_2}e^{2i\phi} + T_1R^2\sqrt{R_2}e^{3i\phi} \dots) \\ &= E_0\left(\frac{T_1\sqrt{R_2}e^{i\phi}}{1 - Re^{i\phi}} - \sqrt{R_1}\right), \end{aligned} \quad (2.1)$$

$$\begin{aligned} E_T &= E_0(T + TRe^{i\phi} + TR^2e^{2i\phi} + TR^3e^{3i\phi} + \dots) \\ &= E_0\frac{T}{1 - Re^{i\phi}}, \end{aligned} \quad (2.2)$$

where  $E_R$  and  $E_T$  are the reflected and transmitted field amplitudes.

The cavity has a periodic spectrum (shown in Figure 2.5), with maxima in the transmission spectra when the phase is equal to a multiple of  $2\pi$  and all the reflected beams destructively interfere. When drawn in frequency space the periodicity of the spectrum is given by  $\Delta\omega_{FSR} = 2\pi\frac{c}{2L}$  and is called the Free Spectral Range (FSR). The linewidth of each resonance peak,  $\Delta\omega_{FWHM}$ , is related to the FSR by a factor dependent solely upon the mirrors' reflectivity.

$$\Delta\omega_{FSR} = \Delta\omega_{FWHM} \cdot \frac{\pi\sqrt{R}}{1-R} \quad (2.3)$$

This factor is known as the finesse and is the usual ‘number of merit’ for Fabry-Perot resonators [119].

$$\mathcal{F} = \frac{\pi \sqrt{R}}{1 - R}. \quad (2.4)$$

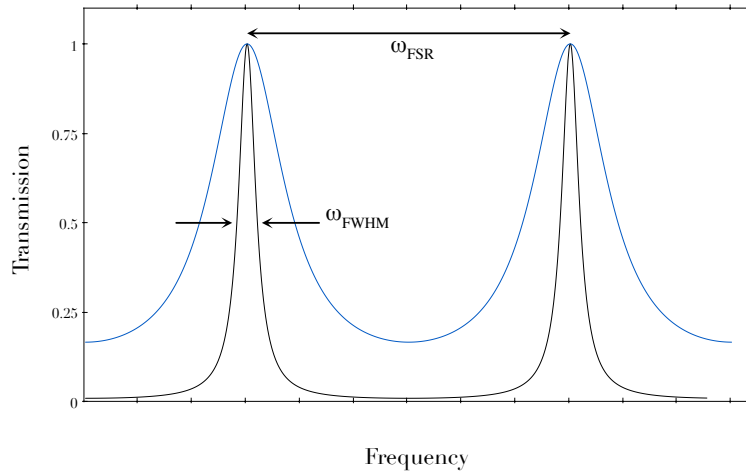


Figure 2.5: Finesse of a Fabry-Perot cavity: The finesse of a cavity is the ratio of its linewidth ( $\omega_{FWHM}$ ) and mode separation ( $\omega_{FSR}$ ). As the finesse increases from  $\mathcal{F} = 2$  (blue) to  $\mathcal{F} = 10$  (black) the individual peaks can be more easily resolved.

### 2.1.3 Cavity Decay Rate

The most obvious method to determine the cavity field decay  $\kappa$  is to directly observe the decay in the intensity of the light emitted from a cavity that is initially on resonance. This method has the advantage of being independent of the probe laser linewidth and has the ability to observe birefringent effects caused by the mirrors’ surfaces. However, previous measurements of this type have shown that for clean, unstressed mirrors the birefringent mode splitting is insignificant at our expected finesse [121]. Also, the laser that is used to probe the cavity has a linewidth of only 200 kHz compared with the expected 10 MHz cavity decay rate, so it should not introduce a significant

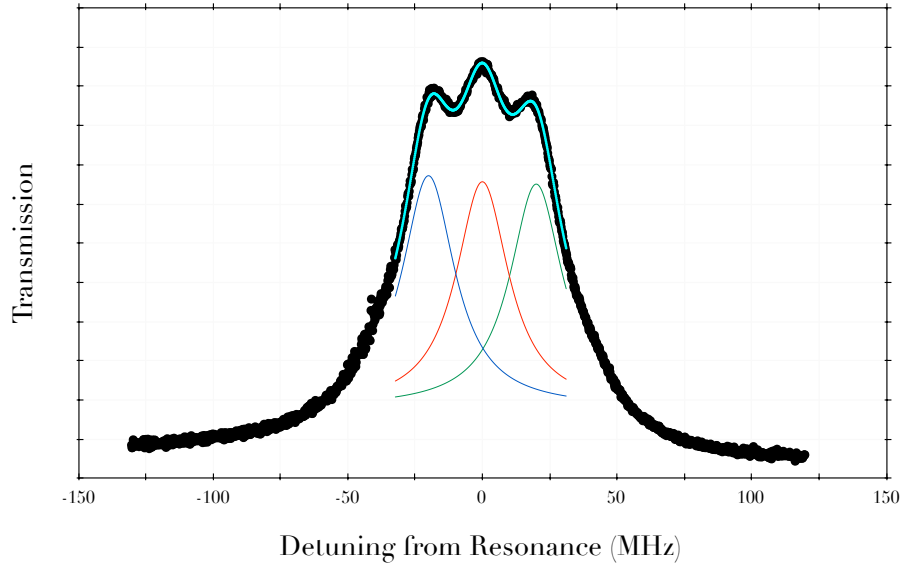


Figure 2.6: Cavity linewidth: the frequency of the laser is swept across the cavity resonance and its transmission is observed. There are three peaks, the carrier (red), and two 20 MHz sidebands (blue, green). These sidebands are used as a frequency scale to measure the cavity linewidth. As the linewidth is similar to the sideband separation, in order to resolve the three lines the amplitudes of the sidebands and carrier must be approximately equal.

error. In light of this, a simpler method - measuring the width of a cavity resonance - can be used to determine  $\kappa$ .

A transmission peak is observed by scanning the cavity length over resonance, but this lacks an accurate frequency scale and so the linewidth cannot be directly observed. To resolve this the laser current is modulated at 20 MHz which puts sidebands onto the carrier frequency (Section 2.3.1) and the fixed 40 MHz separation of these sidebands can be used as a reference.

The resultant transmission profile is shown in Figure 2.6 along with a fit of the three Lorentzian peaks from which it is composed. The FWHM of the fit is measured to be,

$$\Delta\omega_{\text{FWHM}} = 2\pi \cdot (23.74 \pm 0.02) \text{ MHz}. \quad (2.5)$$

### 2.1.4 Cavity Length

So long as it is small enough to ensure that the atom-cavity exhibits strong-coupling (Equation 1.2), the cavity length is not particularly important. A length of  $75 - 150 \mu\text{m}$  gives a good  $g_0$  as well as having sufficient clearance to squeeze the STIRAP beam between the mirrors. Consequently the cavity assembly is imprecise and we calculate the length afterwards by measuring the FSR.

With an expected cavity length of length of  $100 \mu\text{m}$  the FSR would be  $2\pi \cdot 1.5 \text{ THz}$ . As this is much greater than the mode-hop free tuning-range of the laser we cannot measure it directly, so we use instead the spacing of the higher order Transverse Electro-Magnetic (TEM) modes shown in Figure 2.7. The mode structure is described by the paraxial wave equation

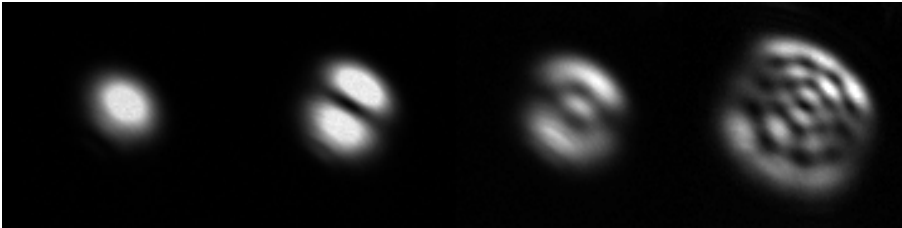


Figure 2.7: Transverse modes of the cavity: due to the cavity curvature the degeneracy of the Ince-Gaussian transverse modes is lifted. The cavity is locked to the fundamental Gaussian mode during experimental runs.

with boundary conditions imposed by the mirror surfaces, taking the form of the set of Ince-Gaussian polynomials [122] (these are the general forms - with an elliptical symmetry - of which the Hermite or Laguerre-Gaussian polynomials are limiting cases). For a cavity of length  $L$  and curvature  $R_c$  the degeneracy of these modes is lifted by the Gouy phase causing spacing of

$$\Delta\omega_{trans} = \frac{1}{\pi} \Delta\omega_{FSR} \cdot \arccos\left(1 - \frac{L}{R_c}\right) = \frac{c}{L} \arccos\left(1 - \frac{L}{R_c}\right) \quad (2.6)$$

This separation should be of the order of 10 GHz, a frequency change that is both easily inside the laser's mode-hop free tuning range, and yet is well above the resolution limit of our wavelength meter.

The separation between the fundamental and first order mode was measured to be,

$$\Delta\omega_{trans} = 2\pi \cdot 35 \text{ GHz}. \quad (2.7)$$

Solving Equation 2.6 with this mode spacing gives a cavity length of  $L = 74 \mu\text{m}$ , which in turn corresponds to a free spectral range of

$$\Delta\omega_{FSR} = 2\pi \cdot 2.0 \text{ THz} \quad (2.8)$$

and a finesse of,

$$\mathcal{F} = \frac{\Delta\omega_{FSR}}{\Delta\omega_{FWHM}} = \frac{2.0 \times 10^{12}}{23.7 \times 10^6} = 85,000. \quad (2.9)$$

This is significantly lower than we were expecting from the specified properties of the mirrors, and indeed whilst building the cavity we measured a Finesse of  $\mathcal{F} = 160,000$ . It is thought that the mirrors were damaged during the vacuum bakeout increasing the losses and thus the cavity linewidth (Section 2.4.1).

## 2.2 ATOM-CAVITY PARAMETERS

The fundamental transverse mode of the cavity ( $TEM_{00}$ ) has a standing-wave Gaussian profile given by the function,

$$\psi(x, r) = \sin\left(\frac{2\pi \cdot x}{780 \text{ nm}}\right) \cdot \exp\left(-\frac{r^2}{\omega_0^2}\right), \quad (2.10)$$

where  $\omega_0$  is the mode waist and is related to the cavity length and mirror curvature by

$$\omega_0^2 = \frac{\lambda}{2} \sqrt{\frac{L}{2} \left( R - \frac{L}{2} \right)}. \quad (2.11)$$

As the cavity length is short compared to its Raleigh range ( $\approx 1$  mm) the radial divergence of the mode can be neglected and the cavity mode can be simplified to a cylindrical shape. The mode volume  $V$  is found by integrating over the  $TEM_{00}$  profile leading to

$$V = \frac{\pi \omega_0^2}{4} L. \quad (2.12)$$

Finally, using the values from [123], the atom-cavity parameters can be calculated as shown in Table 2.1.

Name	Symbol	Value	Unit
Cavity Length	$L$	74	$\mu\text{m}$
Radium of Curvature	$R_C$	5	cm
Mirror Diameter	$\varnothing$	1	mm
Central Clearance	-	69	$\mu\text{m}$
Mode waist	$\omega_0$	18.4	$\mu\text{m}$
Mode size at mirror	$\omega$	18.4	$\mu\text{m}$
Mode Volume	$V$	$2 \times 10^4$	$\mu\text{m}^3$
Linewidth	$\Delta\omega_{FWHM}$	23.7	$2\pi \cdot \text{MHz}$
Free Spectral Range	$\Delta\omega_{FSR}$	2.0	$2\pi \cdot \text{THz}$
TEM Splitting	$\Delta\omega_{trans}$	35	$2\pi \cdot \text{GHz}$
Finesse	$\mathcal{F}$	85,000	-
Atom-Cavity Coupling	$g_0$	15	$2\pi \cdot \text{MHz}$
Cavity Decay	$\kappa$	12	$2\pi \cdot \text{MHz}$
Atomic Decay	$\gamma$	3	$2\pi \cdot \text{MHz}$
Co-operativity	$C$	3	-
Photon Saturation	$n_0$	0.02	-

Table 2.1: Properties of the High-Finesse Cavity

### 2.3 CAVITY STABILIZATION

Once the basics of alignment are taken care of, the primary difficulty with a high-finesse cavity is the mechanical stability. The previously calculated cavity parameters provide an idea of the required stability criteria. To scan over one FSR the mirrors only have to move by  $\Delta L = \frac{\lambda}{2}$ , therefore to shift the cavity frequency by  $\Delta\omega_{FWHM}$  we require a length change of only  $\Delta L = \frac{\lambda}{2} \cdot \frac{1}{\mathcal{F}} = 4.5 \text{ pm}$ . We would ideally like to have the cavity stable to within a small fraction of the resonance peak as this ensures that the cavity and STIRAP laser are always Raman-resonant. This means that the cavity must be stable to within 100 fm for the entire time that the atom cloud interacts with the cavity.

#### 2.3.1 Active Stabilization

To achieve this imposing stability criterion we have to actively stabilize the cavity length. To do this we use the Pound-Drever-Hall (PDH) technique [124], where we beat the light reflected from the cavity against two reference beams each detuned from the carrier by 20 MHz. These beams (created as sidebands to the carrier frequency) were also used as a frequency scale for measuring the cavity linewidth (Section 2.1.3)

The lock scheme electronics are shown in Figure 2.8. The laser is locked to the desired frequency using another PDH circuit (not displayed) and has an instantaneous frequency jitter of  $\sim 200 \text{ kHz}$  (as this is significantly below the cavity locking criterion, its contribution to the measured error signal is considered to be negligible). A 20 MHz voltage controlled oscillator (VCO) is used to modulate the laser diode's current to produce the sidebands. The beat between the carrier and sidebands is detected by a photodiode looking

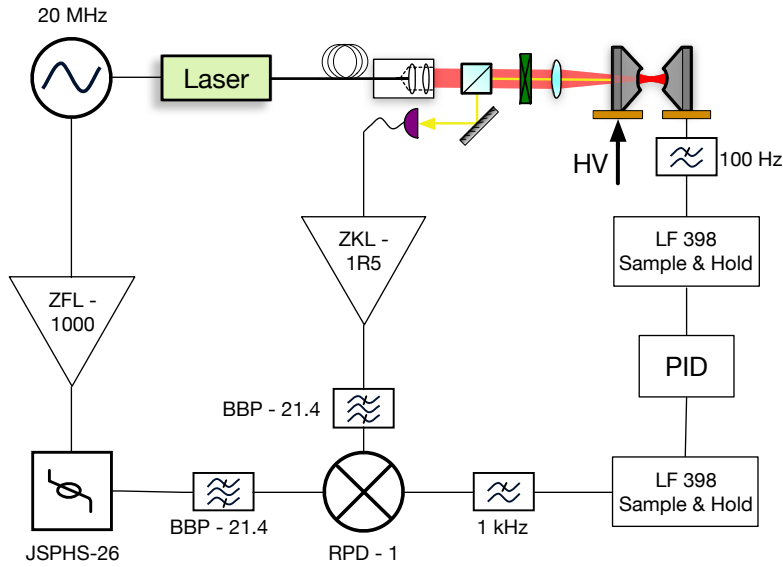


Figure 2.8: Frequency stabilization of the cavity: the cavity length is stabilised using a home-built PDH modulator, PID, and Sample-and Hold circuits. Feedback from this circuit is applied to one of the cavity piezos to ensure that the cavity is always resonant with the stabilisation laser. A high-voltage offset is used to set the cavity length approximately on resonance.

at the reflection from the cavity mirror, isolated using polarization optics. The beat signal is amplified by a *Minicircuits ZKL-1R5* 40 dB wideband amplifier and the DC-offset is removed with a 20 MHz band-pass filter. The signal is de-modulated by mixing it with the same 20 MHz oscillation used to create the sidebands using a *Minicircuits RPD - 1*. This is a type of common mode rejection and ensures that any low frequency jitters on the 20 MHz VCO exist on both inputs to the mixer and are not mapped onto the resulting error signal. The VCO signal is amplified by a *Minicircuits ZFL-1000* and is then tuned by a *Minicircuits JSPHS-26* 180° narrow-band phase shifter to allow the optimum error signal to be obtained.

The phase shifts measured as the cavity moves over a resonance are very small. A symmetric and lossless Fabry-Perot cavity will induce a  $\pi$  phase

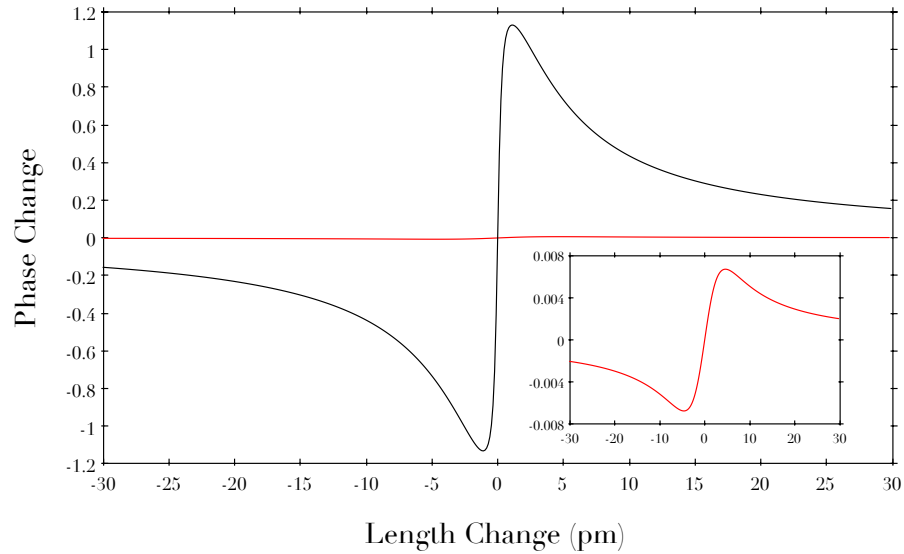


Figure 2.9: Phase change across a resonance peak: the change in phase which is detected by the PDH circuit is dependent on the symmetry of the cavity mirrors. For a cavity with constant finesse and losses, changing from mirrors with equal reflectivity (black) to the asymmetric mirrors used in this experiment (red) results in a large drop in the phase shift. A close-up of the asymmetric case is shown in the insert.

shift in the reflected beam over a resonance peak, whereas the extreme asymmetry of our design results in a phase shift of only  $\pi/250$ . This is shown in Figure 2.9 where the expected phase change across resonance for a cavity of our finesse is displayed. The entire apparatus must therefore be very stable as any small movements will add significant noise to the error signal. All the optics are mounted on 1" steel posts and beam distances are minimized wherever possible; when the cavity lock is in operation even the laminar air flow box on the laser table must be switched off as the air currents cause large scale oscillations in the ‘DC’ level of the error signal. The fiber which transports the light from the laser to the cavity must also have an angled polish (APC). Using a fiber with a flat polish (PC) resulted in a large low frequency noise contribution at  $\sim 0.5\text{--}1$  Hz as the reflections off the fiber ends themselves created an etalon within the fibre. Even this was not quite enough

however, so the fibre length was reduced to 7 cm, the minimum possible which could easily be obtained and yet still act as a spatial filter [125].

It was not found possible to completely remove all of the noise from the error signal at its source, however fluctuations larger than the error signal amplitude were eliminated at low frequencies. To remove high frequency noise a 1 kHz low pass filter was placed on the output of the phase detector and a 100 Hz low pass filter was placed just before the piezos. In addition, all of the cavity locking electronics (as well as an HV amplifier for the DC offset) were run off three 24 V lead-acid batteries to remove 50 Hz noise. With this locking circuit in place it was possible to keep the cavity stabilized on the resonance peak indefinitely.

### 2.3.2 *Passive Stability*

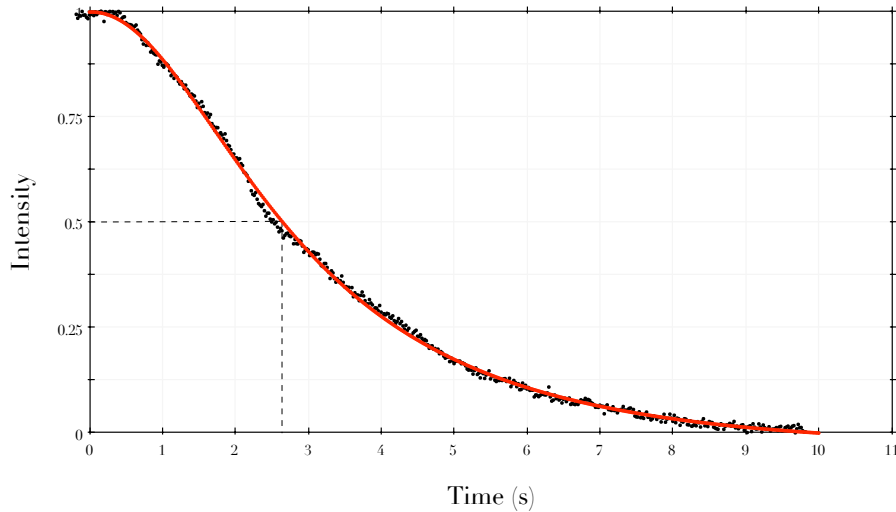


Figure 2.10: Drift of the cavity length: the transmitted intensity of the cavity after the active stabilisation is turned off at  $t = 0$  is shown (mean signal from five repetitions). As the cavity length drifts it moves away from resonance with the laser, causing the transmitted intensity to fall. The measured transmission is shown in black and a theoretical fit in red.

As we are trying to interact an atom with the cavity vacuum field there can be no light within the cavity during experimental runs. This means that the laser to which we lock the cavity must be switched off and the cavity must have sufficient passive stability to remain on resonance over a period of  $\sim 20$  ms whilst no feedback is being applied. The passive stability of the cavity is shown in Figure 2.10. It is clear that the cavity has sufficient passive stability to remain on resonance during the interaction time.

### 2.3.3 *Sample and Hold*

The locking signal that is applied to the piezos is “paused” during the interaction time using a Sample and Hold (SH) circuit (*National Semiconductor LF-398*). This circuit, usually used as an analog-digital converter, follows an analog input whilst at logical 1 and then freezes its output to the last sampled value of the analog signal when at logical 0. This is achieved by sampling the voltage over a capacitor, when the logical input drops to 0 the analog input is disconnected and the voltage over the “hold” capacitor is used as the output. An idealised example of this is shown in Figure 2.11.

There are two SH circuits used in the locking electronics (Figure 2.8), one before and one after the PID. The SH after the PID is used to freeze the voltage across the piezo, once the piezo voltage has been frozen the cavity is disconnected from the locking electronics and the cavity locking beams can be switched off. The error signal from the PDH is frozen using the SH before the PID, pulling the PID voltage to zero and stopping the integrator drifting when the locking beam is switched off. This results in a reliable re-lock of the cavity after each experimental run.

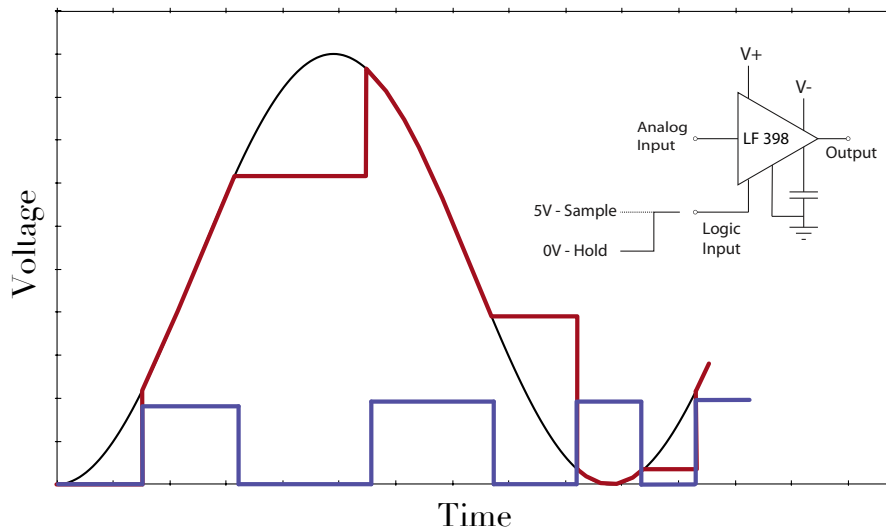


Figure 2.11: Idealized behaviour of a Sample and Hold circuit: an analog input (black sinusoid) is monitored by the S.H., when the logic input (blue) is at 5V the output voltage of the circuit (red) follows the input but when the logical input is 0V the output is kept constant at the last sampled value. A simplified circuit is shown in the insert.

## 2.4 ATOMS

Only half of the challenge in an atomic C-QED system is building a high-finesse cavity - the other half is putting a single atom inside it. If we would like to have an atom remain in the cavity mode for any appreciable time then that atom must be cold; at room temperature a rubidium atom will move at  $\sim 200 \text{ ms}^{-1}$  meaning that it will traverse the cavity mode in under a microsecond, far too short a time to use it for useful photon production. We therefore turn to the workhorse of almost all atomic physics experiments, the Magneto-Optical Trap, to cool the rubidium atoms.

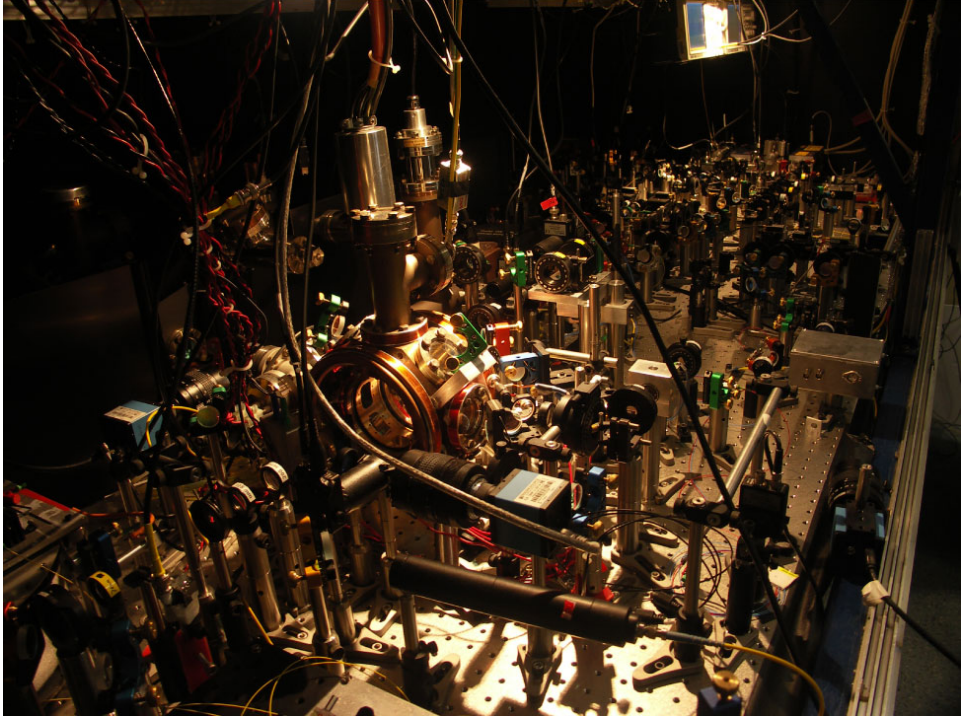


Figure 2.12: Photograph of the experimental apparatus: the vacuum chamber can be seen in the centre along with the MOT and STIRAP optics. The lasers and AOMs can be seen back right and the single photon collimation optics in the left foreground.

#### 2.4.1 *Vacuum Chamber*

As with all cold atom experiments, in order to ensure that the cold atoms are not heated by collisions with a background gas, we must work in an ultra-high vacuum (UHV pressures on the order  $10^{-9} - 10^{-12}$  mbar). This is achieved inside a steel and glass chamber via multiple pumping and baking steps using a rotary-vane pump, a turbo-molecular pump, an ion getter pump (*Vacom IGP-25S*), and a titanium sublimation pump (*Vacom TSP*). The vacuum chamber is made of non-magnetic stainless steel and is surrounded by three pairs of magnetic field coils to compensate for stray fields and thus keep  $B = 0$  within the cavity.

An Alvatec metal vapour dispenser was used to provide rubidium atoms for the experiment. As alkali metals are highly reactive the rubidium is sealed with a layer of indium, during the bakeout procedure this indium seal must be heated until it evaporates and releases the rubidium. The dispenser is pointed directly at the MOT to provide a high atom flux for use in the fountain, unfortunately this also means that it is pointing directly at the cavity mirrors. We suspect that the mirror surfaces received a coating of indium when the seal melted, increasing the mirror losses, thus increasing  $\kappa$  and lowering the finesse (Section 2.1.4).

#### 2.4.2 *Atomic Fountain*

Although various methods of trapping a single cold atom have been developed, both for C-QED experiments and other purposes, they are all very complex. Trapping a single atom is hard, not only must you trap it but you must do so without any external fields which could distort the idealized three level system used to produce the photons. We have therefore decided to sidestep this problem by not trapping an atom at all.

Instead, we form a MOT just below the cavity and then throw the atoms up into the cavity mode. If the impulse applied to the atoms is correct then (ignoring any remaining thermal spread) the atoms will have just enough energy to reach the cavity mode before turning and falling back down towards the MOT. This will give us the longest possible un-trapped interaction time. With an accurate fountain and a low atom density it is possible to load single atoms into the cavity mode. A nice analogy of this is to throw a bag full of tennis balls at a wall with a small window. Most of the balls will hit the wall and bounce away, but if you are lucky a single ball will sail cleanly through the open window.

We must concede that this loading method is probabilistic, but once an atom is found within the cavity mode the stream of photon emissions is deterministic and with a long interaction time this creates a quasi-stable source. The probability of more than one atom interacting with the cavity can be kept negligible using low atom densities.

### 2.4.3 *Magneto-Optical-Trap*

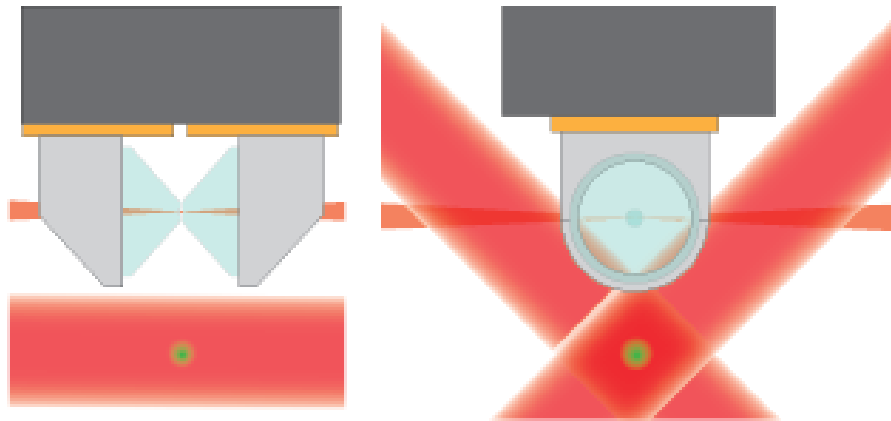


Figure 2.13: Schematic view of the high-finesse cavity integrated into our atom-trapping experiment. All elements and laser beams are drawn approximately to scale. In addition to the arrangement of the MOT beams ( $\varnothing = 8$  mm), the cavity locking beam (and hence the beam path of the emitted photons) can be seen in the side projection. The STIRAP beam (perpendicular to the cavity mode) can be seen in the end projection.

The  $^{87}\text{Rb}$  fountain was constructed by Jerome Dille and comprehensive details can be found in his thesis [126]. Around  $10^6$  atoms are prepared in a standard 6-beam MOT approximately 8 mm below the centre of the cavity (Figure 2.13). The MOT is configured with four beams in the vertical plane - each  $45^\circ$  from the vertical - and a pair of beams along the horizontal. The pair of beams which hit the MOT from above and the pair which hit the MOT from below are controlled separately.

The MOT (Figure 2.14) is loaded for  $\approx 100$  ms and is assisted by UV light-induced desorption (LIAD) [127, 128], allowing for fast loading rates with a relatively low background pressure of  $10^{-10}$  mbar. Following this, the MOT coils are switched off and the frequencies of the upper and lower pairs of beams are detuned relative to each other. This cools the atoms into a moving rest frame with a velocity  $v = \sqrt{2\lambda\Delta f}$ , where  $\Delta f$  describes the relative beam detuning between the upper and lower beams and  $\lambda$  is the laser wavelength. Fine control over the frequencies of these beams (tens of kHz) leads to fine control over the launching velocity, and varying the velocity of the launch allows the throw to be tuned so that the turning point of the atomic motion is in the cavity mode. Using simple ballistic flight arguments and assuming a cavity mode diameter of  $d = 30 \mu\text{m}$  one could, in theory, achieve maximum interaction times of  $t_{int} = 2\sqrt{2d/g} \approx 4$  ms. This assumes that the atom perfectly traverses an anti-node of the cavity field with zero horizontal velocity, however the finite size and temperature of the atom cloud along with the accuracy of the fountain limit the achievable interaction time to  $100 - 400 \mu\text{s}$ .

## 2.5 PUTTING IT ALL TOGETHER

### 2.5.1 Lasers

The laser system of the experiment consists of two diode lasers (Toptica *DL-100*), one used to excite transitions in the  $F = 1 \rightarrow F'$  manifold and the other to excite the  $F = 2 \rightarrow F'$  manifold (Figure 2.15). The lasers are locked using the PDH technique to the  $C_{1,2}$  and  $C_{1,3}$  crossover lines found in sub-Doppler pump-probe spectroscopy [129], these lie midway between the  $F' = 1$  and  $F' = 2/3$  hyperfine levels. The lasers are monitored using Fabry-Perot

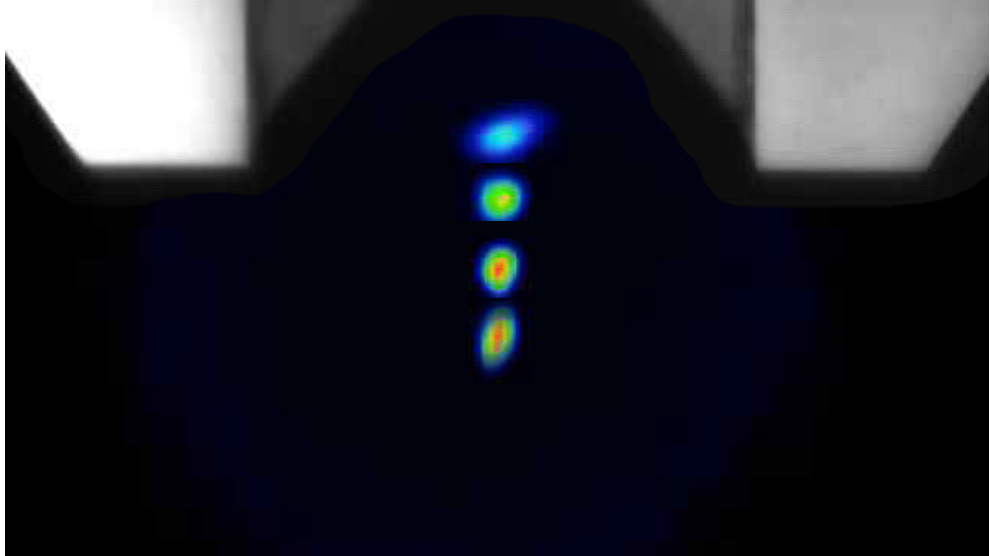


Figure 2.14: A series of false colour absorption images of the atom cloud being thrown towards the cavity at  $\approx 5$  ms intervals. The cavity mirrors and mounts can be seen at the top of the photograph.

interferometers to ensure single mode operation and a Toptica-HighFinesse wavelength meter.

Individual beams for use in the experiment are tuned to their relevant frequencies using Acousto-Optical Modulators (AOMs). As the frequencies of the MOT beams must be changed at various times during experimental runs, the frequency shifts for these beams are performed with the AOMs in double-pass configuration eliminating the change in pointing angle.

The alignment of all the beams is crucial. The upper and lower MOT beams must be completely symmetric so that all forces on the atoms are balanced and the fountain will throw the atoms vertically, furthermore the cavity beams are all aiming at very small targets (a  $\omega = 19 \mu\text{m}$  spot for the cavity locking beam and the  $d = 75 \mu\text{m}$  gap between the mirrors for the STIRAP and cavity re-pump beams). We have therefore decoupled the bulk of the optics - lasers, AOMs etc - from the experiment itself using polarization maintaining optical fibers. This also has the added benefit of

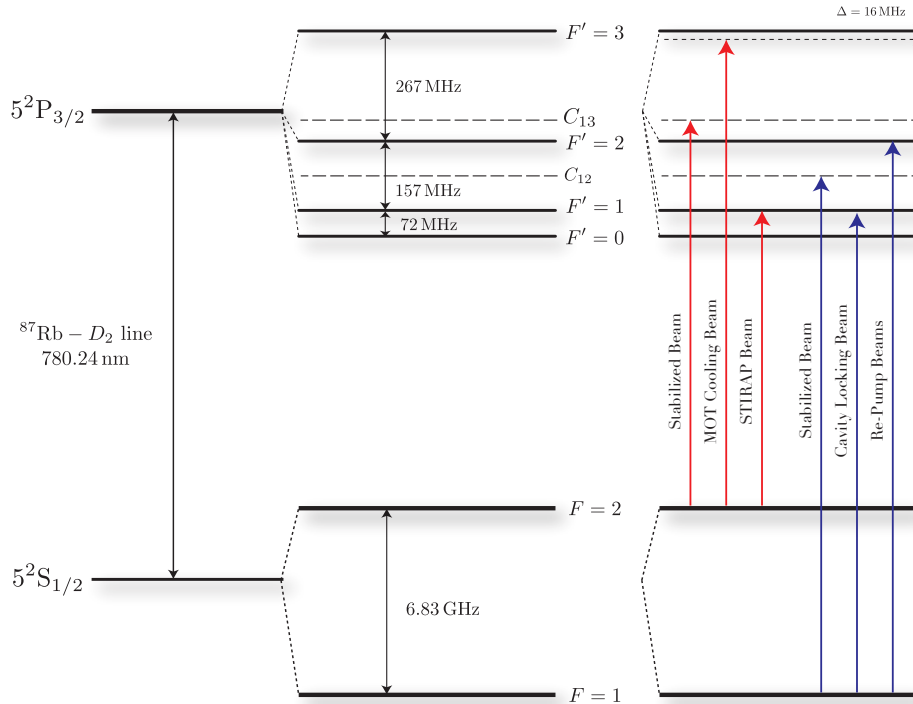


Figure 2.15: Hyperfine energy structure of the  $^{87}\text{Rb}$   $D_2$  line. The  $F = 1 \rightarrow F'$  and  $F = 2 \rightarrow F'$  transitions are each addressed with a Toptica DL-100 laser stabilised to a crossover line and then shifted to the necessary frequencies via AOMs.

acting as a spatial filter, removing the higher order modes leaving only the fundamental Gaussian beam (Figure 2.16).

### 2.5.2 STIRAP Driving and Re-pump Pulses

The STIRAP laser beam used to drive the atom in the cavity is controlled by an AOM (*Crystal Technologies - 3110-122*) controlled by an arbitrary waveform generator (A.W.G. *Agilent N6031A*, 1.25 Gs/s) and a wideband amplifier (*Minicircuits ZHL-1A+*). This amplifier chain, along with the intrinsic properties of the AOM itself, results in a large non-linearity. As we would like to accurately shape the amplitude of the photons' spatio-temporal mode we must be able to drive the atom-cavity with an exact pulse - to



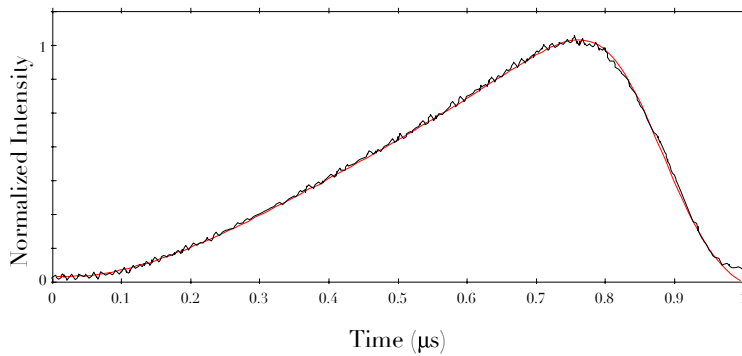


Figure 2.17: Normalizing the STIRAP AOM: non-linearities in the AOM amplifier chain must be compensated for to ensure that the theoretically desired pulse shape (red) is the same what is actually applied to the atom (black).

are focussed to a  $14\ \mu\text{m}$  spot at the cavity axis using an  $f = 30\ \text{cm}$  achromatic doublet. At the mirror edges,  $500\ \mu\text{m}$  away, the beam has a  $16\ \mu\text{m}$  waist which results in just  $0.02\%$  of the incident light being scattered.

### 2.5.3 *Single Photon Detectors*

The emitted photons are detected using Perkin-Elmer single photon counting modules (SPCM QC6-14). These are gated and quenched avalanche photodiodes with a timing resolution of  $350\ \text{ps}$  and a dead-time of  $50\ \text{ns}$ . Although the detectors were factory specified to have dark counts of  $100\ \text{Hz}$  and quantum efficiencies (Q.E.) of  $\approx 60\%$  when we calibrated the detectors we instead measured a dark count of  $1\ \text{kHz}$  and a Q.E. of  $75\%$ . This change is caused by an intrinsic bi-stability of the SPCMs which causes them to jump between their two operating modes - this is thought to be dependent on environmental conditions. It was found necessary to check the SPCMs before use to determine which dark count and efficiency regime they were operating in.

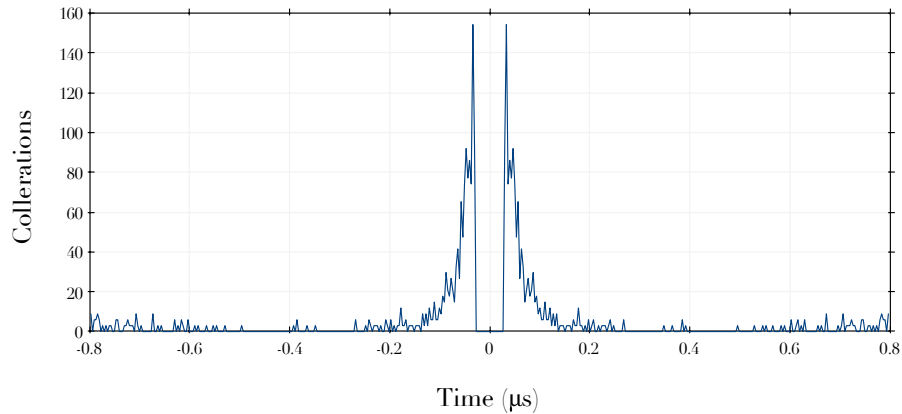


Figure 2.18: SPCM afterpulsing: an autocorrelation measurement of one of the detectors shows the significant number of counts caused by the afterpulsing of the detectors. The artificially imposed dead-time of the detector can be seen by the missing counts around zero. The number of correlations per 4 ns time-bin are shown for a typical experimental run, on this scale the expected signal that we are interested in would only be  $\sim 20$  correlations.

A major drawback of these Perkin-Elmer SPCMs are the ghost detections due to afterpulsing of the diode. The signal amplification caused by the diode avalanche, which is required for us to detect the photon, can also cause another spurious detection to occur. This can be seen in an auto-correlation measurement of the counts from a single detector (Figure 2.18) where there is an exponential decay of these afterpulsing events along with the artificially imposed 50 ns dead-time. These spurious counts come from two main sources: the SPCMs emit a flash of light upon detection of a photon which propagates back along the optical path and can be reflected onto the detector causing a second detection, and also a longer term effect caused by charge impurities in the detectors themselves. This noise prevents us from using data from detector auto-correlations; cross-correlations between two different detectors are not affected.

The TTL output from the detectors is monitored with an Agilent Time-Digital-Converter (*U1051A / TC890*), which records a time-stamp relative to an external pulse (a trigger from the arbitrary waveform generator at the

start of every STIRAP pulse) with a 50 ps timing resolution. The time-stamps of every detector count are then saved for later analysis in MATLAB.

#### 2.5.4 Beam Shutters

The AOM that is used to switch the laser to which the cavity is locked has an extinction ratio of only  $10^5$ ; with a beam power of  $150\ \mu\text{W}$  this results in  $1.5\ \text{nW}$  entering the cavity even when the AOM is in the OFF position. Not only would this light completely swamp the photons that we are looking to produce, the experimental scheme described in Section 1.2 relies on the interaction of an atom with the vacuum mode of the cavity. There is a similar problem on the output side of the cavity. When we lock the cavity length such that the transmission of this same beam is maximized, there is a significant amount of light directed towards the SPCMs which is undesirable as it results in an increased dark count.



Figure 2.19: A simplified optical setup of the cavity and beam shutters. The shutters are placed at a tight focus of the beams to enable fast switching times.

To solve these problems we have implemented two beam blocks which place a thin ( $\sim 0.25\ \text{mm}$ ) layer of steel in the beam path completely interrupting the cavity locking beam. One is placed before the cavity and is switched to the ‘closed’ position during the atom interaction time, the other - placed in front of the SPCMs - is switched to the ‘open’ position to allow detection of the emitted photons (Figure 2.19).

The interaction time (shown in Figure 3.3b) is about 20 ms and as the cavity has an extremely low drift when unlocked (Figure 2.10) the beam

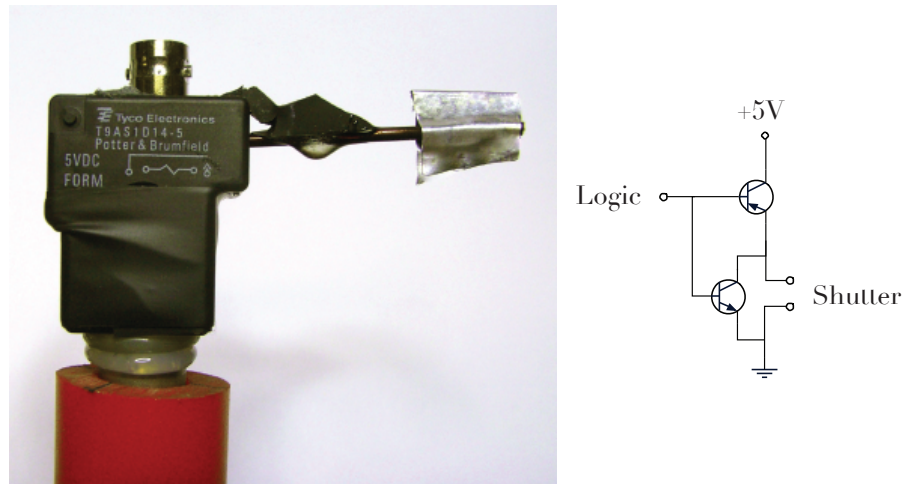


Figure 2.20: Photograph and simplified circuit diagram for the beam-shutter. The red neoprene mount (bottom of the photo) and a sorbathane pad which connects the shutter arm to the mount are used to damp vibrations.

block does not have to be particularly fast - a millisecond is sufficient, the cavity ring-down time of 10 ns ensures that the atom truly interacts with the vacuum state. Rather than trying to achieve a fast switching time, as the cavity-lock must be interrupted before the beam is blocked, the more pressing concern is minimizing any vibration during the switch. The cavity will be relying solely upon its passive stability to remain on resonance and so any vibrations applied to the laser table could easily move the cavity mirrors by the 100 fm required to knock it out of resonance.

Our first attempts to make a beam block were direct copies of the shutter described in [130], a beam block based on the voice coil and reading arm of a commercial hard-disk drive. Unfortunately the fast switching time of this shutter meant that there were also very large vibrations, causing the cavity to drift by a significant fraction of  $\kappa$ , and even on occasion unlock the lasers. We have instead developed a cheap and simple beam block based on a relay (*Tyco-T9AS/V*) and a simple control circuit (Figure 2.20). The relay arm is about 5 cm long and has a  $\sim 1$  mm range of motion, and can switch a focussed beam in  $\sim 200 \mu\text{s}$  with a  $\sim 50 \mu\text{s}$  jitter. To minimize vibrations

the shutter is bolted to the laser table with a neoprene mount which has been machined to the same blueprint as a standard 1/2-inch post holder. With this mount no vibrations can be observed on the cavity transmission spectrum.

## 2.6 CONCLUSION

In this chapter I have presented the experimental foundation of our C-QED based single photon source. A high finesse cavity ( $\mathcal{F} = 85,000$ ) was constructed and characterised; values of  $\{g, \kappa\} = 2\pi \cdot \{15, 12\}$  MHz put this cavity in the strong-coupling regime with an atom-cavity co-operativity of  $C = 3$ . The cavity is actively stabilised using the Pound-Drever-Hall technique. Due to its high level of passive stability it can remain unlocked during the 20 ms experimental runs with the locking laser switched off, this ensures that no extraneous light interacts with the atom. To enable this a Sample and Hold circuit and a simple beam-shutter were developed.

$^{87}\text{Rb}$  atoms were trapped and cooled in a Magneto-Optical Trap and were then loaded into the cavity via a frequency detuned atomic fountain. The background pressure of the vacuum system is kept low ( $10^{-10}$  mbar) and fast loading of the MOT is achieved using Light-Induced Atomic Desorption.

Finally the apparatus to produce and detect single photons was characterised. The shaped pulses, which are used to drive the atom, were created using an RF arbitrary waveform generator and an AOM, whose response was linearized so that exact pulse shapes could be applied to the atom. The single photon counting modules were characterised and found to have a high level of after-pulsing, preventing us from using them for auto-correlation measurements.



PHOTONS

---

In this chapter the photon-generation scheme that was briefly outlined in the Introduction and more comprehensively discussed in references [119, 120] is implemented using the apparatus described in Chapter 2. We demonstrate that the system behaves as a ‘push-button like’ single-photon source which exhibits sub-poissonian statistics. The photon source operates intermittently for periods of up to  $100\ \mu\text{s}$ , with single-photon repetition rates of 1.0 MHz and an efficiency of approximately 80%. Atoms are loaded into the cavity using an atomic fountain, with the upper turning point near the cavity’s mode centre. This ensures long interaction times without any of the disturbances induced by trapping potentials and is the key to reaching ‘deterministic’ efficiencies (as high as obtained in photon-heralding schemes). The photons are also shown to be indistinguishable and thus suitable for use in quantum interference experiments.

The optimisation of the atomic fountain and STIRAP driving laser are shown in Section 3.1. The singleness of the photons that are produced is tested in Section 3.3, and with basic post-selection of our data the photons’ sub-poissonian statistics are shown in Section 3.4. The efficiency of the source is discussed in Section 3.5 and the indistinguishability of the photons is proved via Hong-Ou-Mandel interference in Section 3.6.

### 3.1 EXPERIMENTAL OPTIMIZATION

#### 3.1.1 *Loading Atoms into the Cavity*

The first obstacle that we must overcome to implement the atom-cavity based single photon emitter is to confirm that we can reliably load single atoms into the cavity. In most atomic physics situations the simplest method of detecting an atom is to make it emit photons which can then be detected with an APD or a CCD camera. For this system however, due to the cavity mirrors, observing photons is quite difficult and the experimenter faces two challenges that do not occur in free space.

The first problem is simple: the atoms are contained between two macroscopic mirrors which have a very small separation so the solid angle through which fluorescence can be collected is minimal. The second problem stems from the need to overlap an illumination beam with the atoms to excite them causing them to fluoresce. As the cavity mirrors are quite large, and are only spaced by  $\sim 75 \mu\text{m}$ , it is quite hard to get a beam between them, indeed the maximum possible beam waist at the cavity mode is only  $\sim 15 \mu\text{m}$  (Section 2.2); getting this illumination beam overlapped with a cavity-mode of unknown position which might (or might not) contain an atom is not easy. These problems conspire to make fluorescence imaging of atoms in the cavity mode impractical.

A more useful method for detecting atoms is to use the effect of the vacuum Rabi splitting. As an atom passes through the cavity mode it will shift the resonance of the system [94]. If the cavity is locked onto an atomic resonance (e.g. the  $F = 1 \rightarrow F' = 1$  transition) and one observes the cavity transmission with a co-resonant laser beam, a dip will be seen whenever atoms enter the cavity mode [131]. This is due to the shift of the resonance of

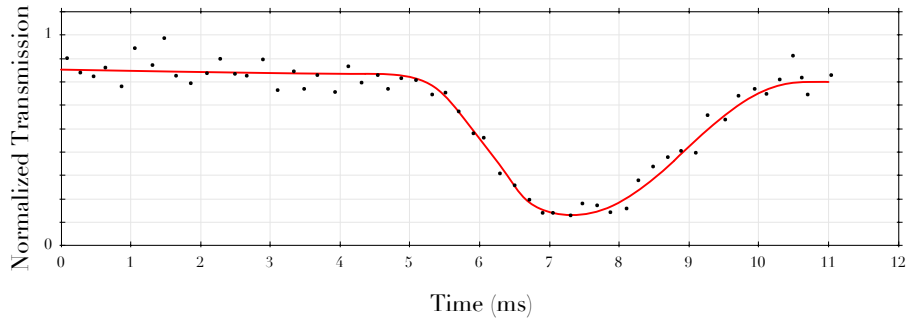


Figure 3.1: Detecting atoms: the presence of atoms in the cavity mode causes a shift in the resonance frequency of the cavity (vacuum Rabi splitting) which can be probed with a weak laser. A 5 ms long dip in the intensity of the transmitted light was observed as the atom cloud passed through the cavity mode.

the atom-cavity system away from the laser frequency. Although this method of detecting atoms relies on more complex physics it is actually relatively simple to implement as the required experimental apparatus is already in place (Section 2.3). A typical measurement of the transmitted power is shown in Figure 3.1.

### 3.1.2 Producing Photons

Once we have verified that we have loaded atoms into the cavity we can attempt to produce photons. To do this we must drive the atoms whilst they are within the cavity mode with a laser locked to the  $F = 2 \rightarrow F' = 1$  transition which, with the cavity mode stabilised to  $F = 1 \rightarrow F' = 1$ , meets the Raman co-resonance condition. A photon should be produced in the cavity which then leaks out through the less reflective mirror at the rate  $\kappa$ . Once the cavity has emitted a photon the atom is decoupled from the exciting laser and must be optically re-pumped to the initial state  $F = 2$  before the sequence can be repeated.

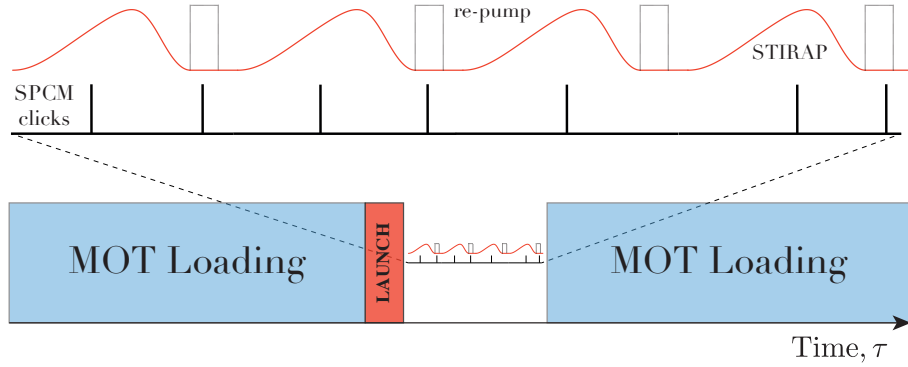


Figure 3.2: Experimental sequence for producing photons: After the atoms have been launched all lasers apart from the STIRAP pulse and re-pump are switched off. These two lasers are pulsed continuously at 1 MHz for the entire 20 ms interaction time (20,000 pulses). A sample of this sequence of STIRAP (red) and re-pump (grey dash) pulses is shown along with a sample of the corresponding SPCM counts (black).

The experimental sequence is shown in Figure 3.2, the MOT is loaded for  $\sim 200$  ms and then it is launched towards the cavity. The cavity lock is then switched off and the sequence of STIRAP and re-pump pulses is continuously applied to the cavity. Once the atom cloud has traversed the cavity mode the pulses are stopped, the cavity is re-locked, and the MOT is reloaded.

### 3.1.3 Optimizing Atom Loading

The histogram of detector clicks caused by atoms traversing the cavity can be used to optimize the atomic fountain to have the atoms within the cavity mode for as long as possible. To do this we tune the fountain's launch velocity such that the atoms reach the maximum height of their ballistic flight inside the cavity mode. As photons are only produced when an atom is located in the cavity mode, the envelope of the histogram of detector counts can be used to characterize the fountain. If we assume a similar number of atoms enter the cavity mode per launch, a narrow peak in the number of counts indicates

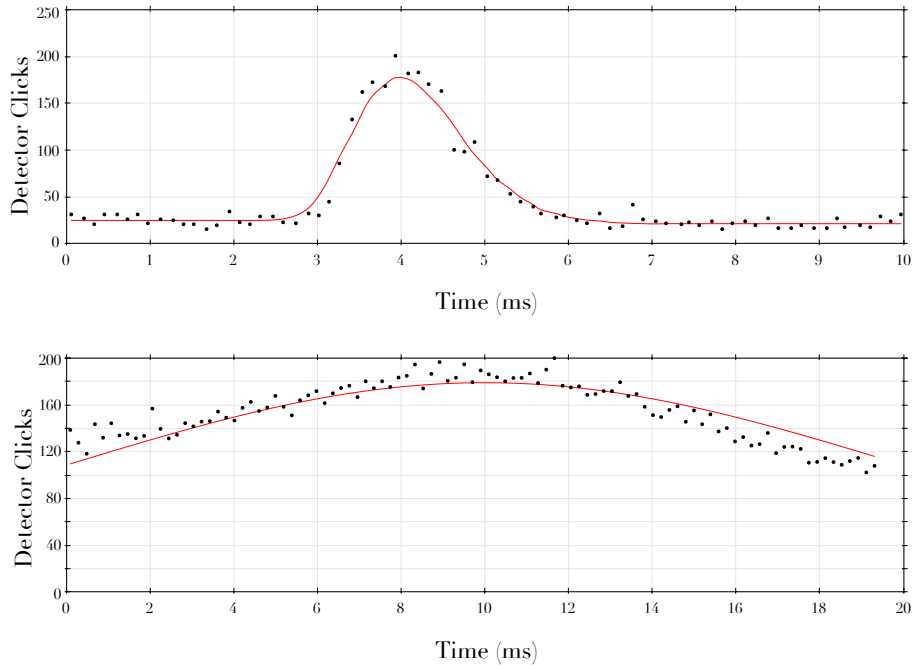


Figure 3.3: Atomic fountain optimisation: a histogram of photons produced per as a single atom cloud traverses the cavity mode (black) was used to optimise the atomic fountain. An order of magnitude improvement was obtained in the interaction time of the atom-cloud with the cavity, from  $2 \rightarrow 20$  ms. The time  $t = 0$  is arbitrarily selected to best display the observed counts. The number of atoms launched in each case was different and so the displayed count rates should not be compared.

that the atoms are traversing the cavity mode very quickly compared with the wide peak caused by slowly moving atoms. The launch velocity was therefore reduced to maximise the width of the histogram envelope (Figure 3.3). The maximum practical width corresponds to a launch velocity of  $\sim 1 \text{ m s}^{-1}$ . More details and analysis of the atomic fountain can be found in the thesis of Jerome Dilley [126].

#### 3.1.4 Optimizing the STIRAP beam

Once we have loaded the atoms into the cavity, the STIRAP driving beam must be overlapped with them. This is performed by walking the beam

through the gap between the cavity mirrors using Piezo controlled beam-steering mirrors (Newport Agilis) as shown in Figure 3.4a. As the gap between the mirrors is only  $70\ \mu\text{m}$  wide it is not possible to steer the beam in the direction parallel to the cavity axis. The beam must be perfectly perpendicular to the cavity mode to get through the gap, so the only degree of freedom is the vertical direction.

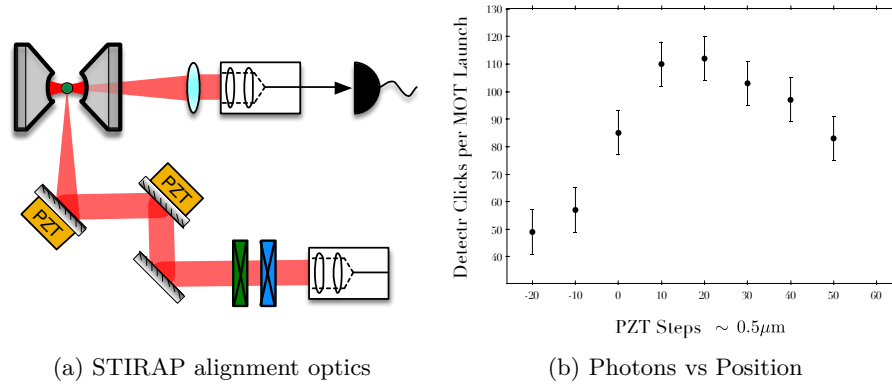


Figure 3.4: Aligning the STIRAP beam: the STIRAP laser was aligned to the cavity mode (a) by observing the photon count rate as the vertical position of the beam was changed (b).

A plot of the number of detector counts per MOT launch relative to the position of the STIRAP beam is shown in Figure 3.4b. The most obvious feature of this plot is the asymmetry. As the beam has a symmetric Gaussian profile, one would expect that its vertical displacement around the cavity axis should cause a symmetric drop in the number of photons produced. This is the case for a stationary atom placed at a particular vertical position within the cavity, however that is not the situation in this experiment. As we launch atoms into the cavity from below they are able to interact with the STIRAP beam before they reach the cavity centre. If the STIRAP beam is centred below the cavity, when the atoms pass through this beam they will scatter light and be blown away, thus reducing the number of available atoms and hence the photon count rate. For a beam centred just above the

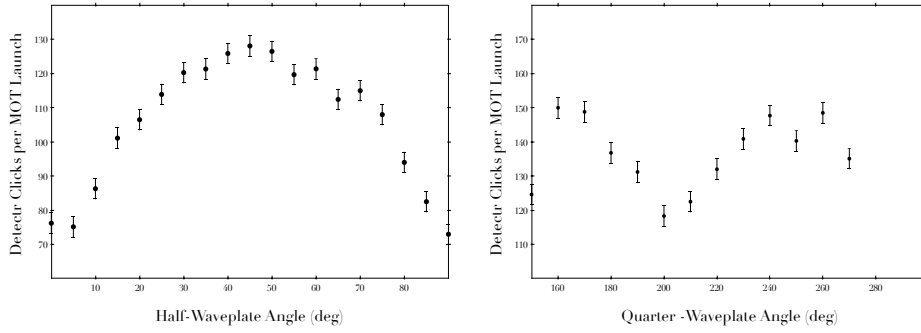


Figure 3.5: Optimizing STIRAP polarisation: The polarisation of the STIRAP beam was aligned using half and quarter-wave plates to be perpendicular to the cavity mode in order to drive  $\sigma^{+/-}$  transitions. This results in a maximal number of photons being produced.

cavity mode this ‘blowing away’ does not occur and the drop in counts is solely due to the change in the interaction strength. We phenomenologically determine the beam to be well aligned when we observe a maximum number of photons.

The other parameter which must be optimized is the polarization of the STIRAP beam; we would like to excite the  $\sigma^+/\sigma^-$  transitions as the the higher F-number of the initial ground state means that not all of its Zeeman sub-levels can be excited by a  $\pi$  transition. To do this we would like the STIRAP laser to be aligned perpendicular to the quantisation axis as defined by the cavity. As the vacuum chamber viewports are slightly birefringent we cannot measure the exact polarization of the beam incident on the atoms. We therefore set the polarization to be approximately correct and fine-tune this using half and quarter-wave plates. We again phenomenologically define the maximum number of observed counts to be the ‘correct’ polarization (Figure 3.5) .

### 3.2 PHOTONS

A histogram of the the clicks that were observed on the detectors for a well optimized source is shown in Figure 3.6. Due to the incoherent re-pump step each STIRAP pulse (Figure 3.6a) is an independent repetition of the experiment and the time of each detector click can be taken relative to the start of each pulse. In this way, after a few thousand repetitions the histogram of counts shows the relative probability of detecting the photon at a particular time and hence the photon wavepacket i.e.  $P_{click}(t) \propto |\psi_{ph}(t)|^2$ . Detector clicks caused by scattered photons during the re-pumping (unshaded area) are ignored in all future discussion.

### 3.3 PHOTON STATISTICS

It can be seen in Figure 3.6b that we have managed to detect some photons, or at least that our photon counters have registered clicks; we would now like to analyze these clicks to prove that we have indeed managed to produce a single photon source. With a highly efficient source and a perfect, noiseless, number-resolving detector this would be trivial; in practice it is necessary to demonstrate the anti-bunched sub-poissonian statistics of the photon arrival times to prove the photons' singleness.

#### 3.3.1 *Classical Intensity Fluctuations*

The properties of any state of light may be determined by the statistics of its intensity fluctuations using Hanbury Brown Twiss interferometry [132–134]. This technique relies on measuring the autocorrelation of the detected light, i.e. we look for differences in the detected intensity at two times  $I(t)$  and

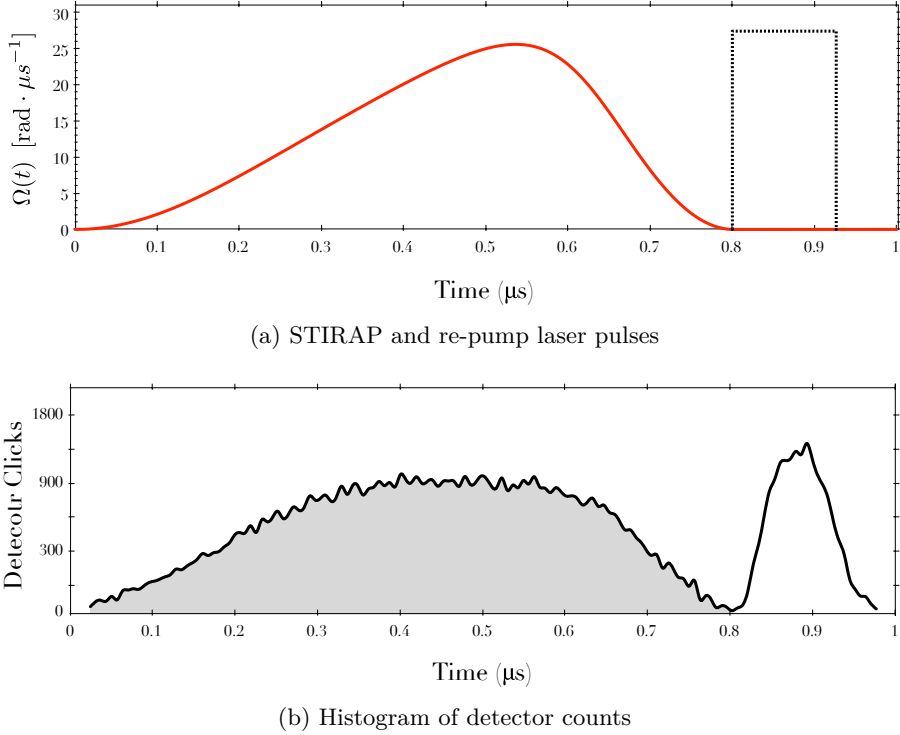


Figure 3.6: A histogram of photons emitted from the cavity: the sequence of STIRAP (red) and re-pump (dashed) pulses is shown in (a), the re-pump Rabi-frequency is not to scale. A histogram of detector counts when this pulse is applied to the atom is shown in (b), this is the sum of 2000 MOT launches and is displayed as the total number of decoctions per 7.5 ns time-bin. Photons which have been produced by the STIRAP process are shaded grey, and counts from re-pump light scattered off the mirror surfaces are left unshaded.

$I(t + \tau)$ . The properties of the light are then defined by the second order correlation function,  $g^{(2)}(\tau)$ ,

$$g^{(2)}(\tau) = \frac{\langle I(t)I(t + \tau) \rangle}{\langle I(t) \rangle \langle I(t + \tau) \rangle}, \quad (3.1)$$

where  $\langle \dots \rangle$  denotes the time average. A good introduction to photon statistics can be found in Fox (2006) [135].

The benchmark against which the measured  $g^{(2)}(\tau)$  correlation function of light is compared is that of a coherent source, i.e. a laser - perfectly monochromatic light in which there are no intensity fluctuations. It is trivial

to see that in this case the correlation function reduces to  $g^{(2)}(\tau) = 1$  for all time delays  $\tau$ . It is also clear from Equation. 3.1 that any classical fluctuations in  $I(t)$  will cause  $g^{(2)}(0)$  to increase, this is because there must be equal fluctuations of  $I(t)$  above and below the mean  $\langle I(t) \rangle$  and so  $\langle I(t)^2 \rangle > \langle I(t) \rangle^2$ .

### 3.3.2 Quantum Fluctuations

In this experiment, and indeed in the quantum world in general, we are no longer dealing with large beam intensities and diode photocurrents but with clicks on single photon detectors. When we consider a quantum optical field we can imagine a stream of point-particle photons. If this is observed with a single photon detector (for example an APD) we can look at the number of photons detected in a certain time window  $\Delta t_{gate}$ . If we let  $\Delta t_{gate} \rightarrow 0$  we will start to see the inherent ‘graininess’ of the field; sometimes we will see a photon during  $\Delta t_{gate}$  and sometimes we will not: even for a coherent field we no longer have a constant photocurrent (Figure 3.7a). Instead of looking at the instantaneous intensity  $I(t)$ , we must now re-define the criteria for the correlation function in terms of the number of photons that are observed,

$$g^{(2)}(\tau) = \frac{\langle n_1(t)n_2(t+\tau) \rangle}{\langle n_1(t) \rangle \langle n_2(t+\tau) \rangle}, \quad (3.2)$$

where  $n_i(t)$  is the number of counts at detector  $i$  at time  $t$ .

As coherent light has constant power, the mean number of photons per unit time must also be constant (with a completely random arrival time) and thus the time between detector clicks will follow a Poissonian distribution. With these constant probabilities the correlation function will remain flat at  $g^{(2)}(\tau) = 1$ . A single quantum emitter will show a very different behaviour. Photons are produced by a transition from an excited state to a ground state

with only one photon being emitted per transition. Once the emitter is in the ground state it must be re-pumped back to the excited state, and during this time there cannot be another photon emitted - the intensity must be identically zero and so  $g^{(2)}(0) = 0$ . This therefore is the signal which we are looking for, a dip in the number of correlations about  $\tau = 0$ , and the signifier of a perfect single photon source is that the dip reaches  $g^{(2)}(0) = 0$  (Figure 3.7b).

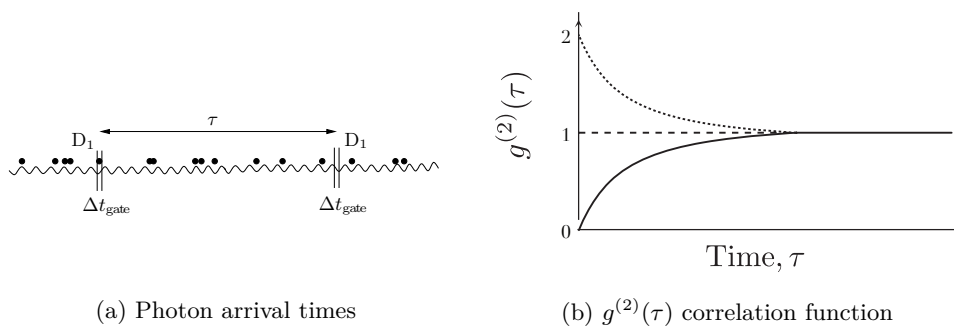


Figure 3.7: Autocorrelation of an optical field: the correlation statistics of a stream of photons (a) at a time interval  $\tau$  are shown (b) for coherent (thick dash), thermal (thin dash) and anti-bunched single photon (solid) sources. Reproduced with permission from [136].

### 3.3.3 Intermittent Sources

The  $g^{(2)}(\tau)$  correlation function relies on having good knowledge of the expected click probability at each moment in time,  $P_{n \geq 1}(t)$ , in order to normalize the function. With a stable continuous source this is trivial, one simply observes the average count rate over a long period, however in our case it is rather more complicated.

Imagine the correlation function from a continuous anti-bunched source (for example a pumped parametric down conversion crystal),  $g^{(2)}(\tau)$  will take the form of the solid line shown in Figure 3.7b. Now imagine that the grad student

running the experiment walks off for a cup of coffee and whilst he is away the laser pumping the crystal drifts out of lock and slowly stops producing photons. When looking at all the correlations for the first photon, there will be a constant stream of photons causing correlations until the start of the coffee break, at this point the photon production efficiency decreases causing the correlation function for  $\tau > \tau_{active}$  to decrease  $g^{(2)}(\tau) \rightarrow 0$  until it stops altogether,  $g^{(2)}(\tau) = 0$  (Figure 3.8). This reduction in the photon production probability will also cause the random correlations to have  $g^{(2)}(\tau) > 1$ . This is an extreme example of what happens in our experiment as an atom passes through the cavity - we simply have a different timescale. Whilst an atom is perfectly positioned in the centre of the cavity mode we will observe photons, as the atom moves out of the cavity mode the atom-cavity coupling  $g$ , and hence the photon production efficiency, decreases (the grad student gets lazy and wanders off for coffee).

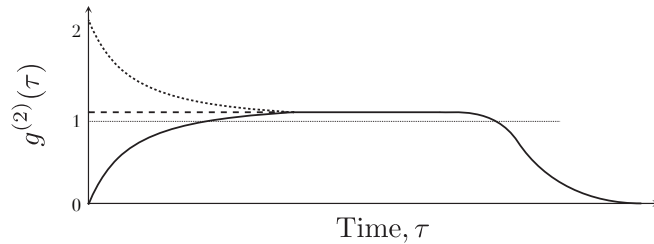


Figure 3.8: Correlation function from an intermittent source: at late times the emission probability reduces, correlations therefore cannot happen and  $g^{(2)}(\tau) \rightarrow 0$ . If normalised by the mean emission probability over all times (i.e. including when it's not working) the random correlations will be above 1.

It is possible, with perfect knowledge of the system, to correctly normalize the correlation function to take this change in  $P_{n \geq 1}(t)$  into account [137]. However it is initially simpler not to use the second order correlation function  $g^{(2)}(\tau)$  at all and instead simply look at the raw number of correlations at a particular time delay  $\tau$ .

### 3.3.4 Hanbury Brown Twiss Interferometer

Although it is theoretically possible for an autocorrelation measurement to be performed with a single detector, in practice, due to the dead times of SPCMs and their inability to resolve the number of incident photons, an experimental arrangement as shown in Figure 3.9 is required. The output of the atom-cavity system is split via a 50/50 beam-splitter and the two output ports are each interrogated by a SPCM. If multiple photons are emitted, as the beam-splitter will randomly split the photons between the two detectors, it is possible for both detectors to click simultaneously. If just a single photon is incident, as it is an indivisible particle one - and only one - of the two detectors will click.

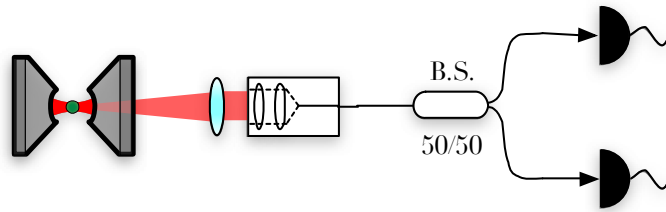


Figure 3.9: Hanbury Brown Twiss interferometer: due to detector noise and dead times, the autocorrelation of the photon system is found using the cross correlation of two detectors. Two SPCMs are used on the output of a 50/50 fibre based beam-splitter, with low count rates this ensures that at least one detector is always ‘on’.

A plot of the correlations measured between the two detectors is shown in Figure 3.10: this includes correlation contributions from both the photons and from the dark noise of the detectors (1 kHz). The masking of detector counts which occur during the incoherent re-pump step (Section 3.2) gives rise to the periodicity of the background which would otherwise be at a constant level (if desired this can be recovered by adding a Poissonian background with the observed dark-count rate to these masked regions). The  $g^{(2)}(\tau)$  function itself

exhibits the periodicity that one would expect for a pulsed source, with peaks separated by the repetition period. It can clearly be seen that the expected peak at  $\tau = 0$  is missing and the number of correlations fall to the background level. We may therefore conclude that the correlations at  $\tau = 0$  are caused by noise, and thus that there is only one photon produced per atom per pulse. The envelope of the correlations is a consequence of the limited atom-cavity interaction time, if the atom-cavity system produces a photon at a time  $t$  there is still a small probability of other photons being produced up to  $t + 100 \mu\text{s}$  later. After this time however there are no correlations above the background as the atom has left the cavity mode. The background is considered more fully in Section 3.4.1.

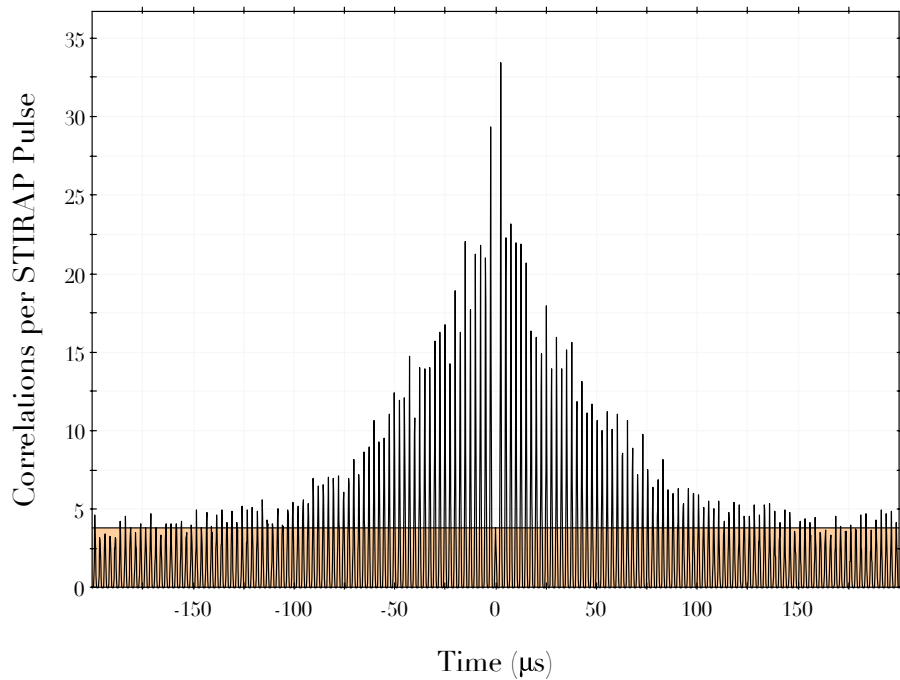


Figure 3.10: Second order correlation function of the detected photons: the missing central peak implies a single photon source, and the envelope of peaks shows that the atom remains in the cavity mode for  $T_{interact} \approx 100 \mu\text{s}$ . The dark-count background level is shaded yellow. The STIRAP repetition rate has been reduced to 400 kHz so that the individual peaks are visible.

## 3.4 CONDITIONING

As we only load atoms into the cavity probabilistically, to ensure that we never observe two atoms in the cavity simultaneously we must keep the overall probability of having any atom in the cavity very low. Most of the time therefore the cavity will be empty, by looking at the detector clicks from these times we simply increase our noise levels from background and dark counts unnecessarily. Even when an atom is in the cavity it is far more likely to be in the wings of the mode, and thus poorly coupled, than located in an anti-node at the cavity centre. What we would like therefore is a method of sorting through our data and only using those time intervals where an atom is present and at the centre of the cavity mode.

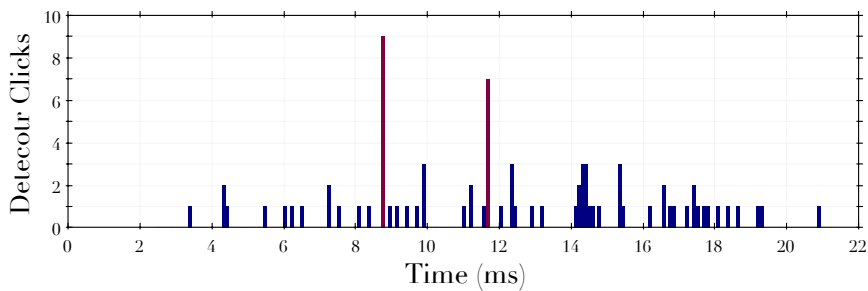


Figure 3.11: Time-binned photon arrival times from a single MOT launch: the number of photons detected per  $100 \mu\text{s}$  time-bin can be used to observe atoms within the cavity mode. During certain bins (red) there is a sharp increase in the number of detected photons ( $\sim 10$  per 100 STIRAP pulses) compared with the background. It is during these times that an atom is present in the cavity and the experiment is deemed to be ‘working’.

To do this we look at the arrival times of the photons within the 20 ms period that it takes for the whole atom cloud to traverse the cavity. A time-binned trace of these arrival times for a single MOT launch is shown in Figure 3.11, this is similar to Figure 3.3b which is the combination of 2000 such traces. The most striking part of this trace is the two time-bins at

$\sim 8, 12$  ms, (red), during which the count rate is significantly higher than at any other time. This is exactly what we would expect to see from an atom traversing the cavity mode, i.e. a string of photons being produced. Once we have identified those times when an atom is present within the cavity (this is arbitrarily set as the data from those  $100 \mu\text{s}$  time intervals with more than a certain number of counts e.g.  $\xi > 1, 2, 3 \dots$ ) the data can be further examined by ‘zooming in’ and then plotting another, finer ( $25 \mu\text{s}$  time-bin) histogram (Figure 3.12).

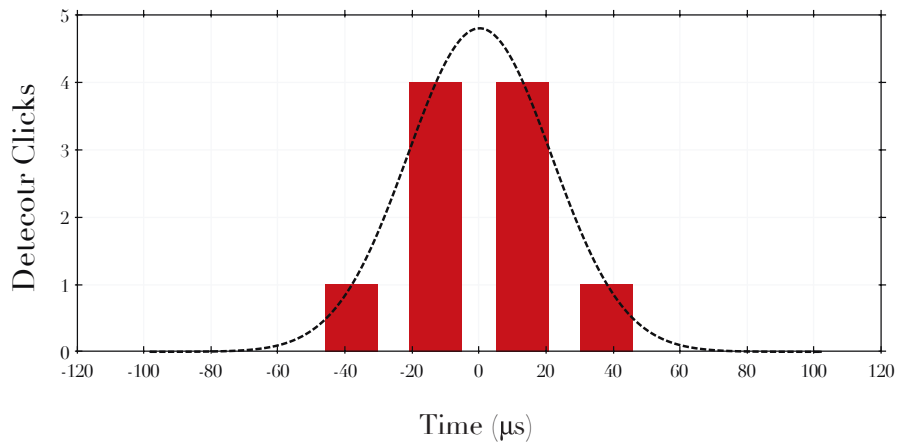


Figure 3.12: Time-binned photon arrival times from a single atom transit: the number of photons detected per  $25 \mu\text{s}$  time-bin can be used to observe atoms transitting the cavity mode.

The Gaussian distribution of clicks in this ‘finer’ histogram shows the atom’s trajectory through the cavity. When the atom is far from the cavity centre,  $g$  and the emission probability  $P_{emit}$  are small and hence there are few counts; as the atom moves to the centre of the cavity  $g$  and  $P_{emit}$  reach their maximal values with a corresponding increase in counts, and finally as the atom moves away from the cavity mode the number of counts decreases. A Gaussian curve can now be fitted to this histogram; the time about which the curve is centred is used as the time when an atom is well-coupled to the cavity mode and its width tells us the atom’s transit time.

### 3.4.1 Conditioned Correlation Functions

By post-selecting only those times during which an atom was present, this conditioning allows us to significantly improve our Hanbury Brown Twiss interferometry. Figure 3.13a shows a close-up view of the  $g^{(2)}(\tau)$  correlation function centred around  $\tau = 0$ . The presence of clicks at  $\tau = 0$  means that something is wrong: either dark counts and an external background or more worryingly, another atom is in the cavity. After the data has been conditioned on the presence of an atom the  $g^{(2)}(\tau)$  correlation function is much cleaner, with no central counts at all. We can therefore conclude that these correlations were erroneously introduced from random coincidences of the dark noise.

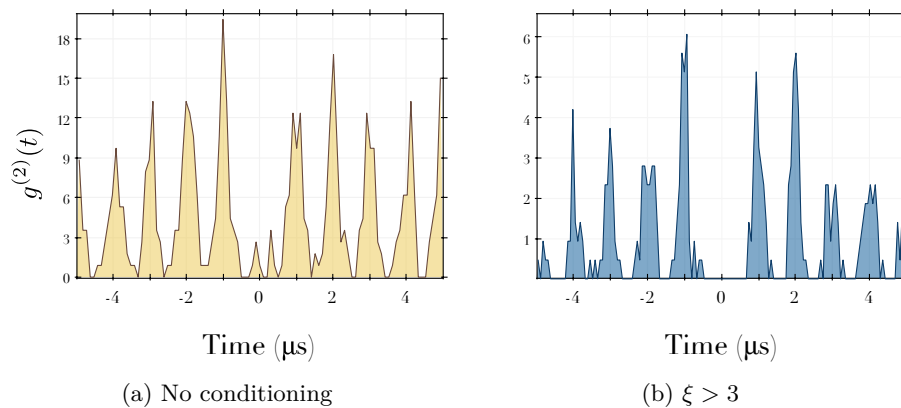


Figure 3.13: Second order correlation function of conditioned photons: the correlations around  $\tau = 0$  are shown without conditioning on the presence of an atom and conditioned photon when  $\xi > 3$  counts per  $100 \mu\text{s}$ . The correlation functions are normalised to the total number of counts, assuming a static source - hence the change in height (Section 3.3.3).

This conditioning method also allows us to reconstruct what the  $g^{(2)}(\tau)$  correlation function would look like if we had a stationary atom within the cavity [137]. Once the times during which an atom is present in the cavity have been identified, the relevant detector clicks can be concatenated to form a new data set consisting solely of counts occurring when an atom is present

in the cavity. This removes the interaction-time limited envelope of  $g^{(2)}(\tau)$  and allows us to correctly normalise the correlation function. This simulation of a static source (Figure 3.14) emphasises the sub-poissonian statistics of the source with a value of  $g^{(2)}(0) = 0.06$ .

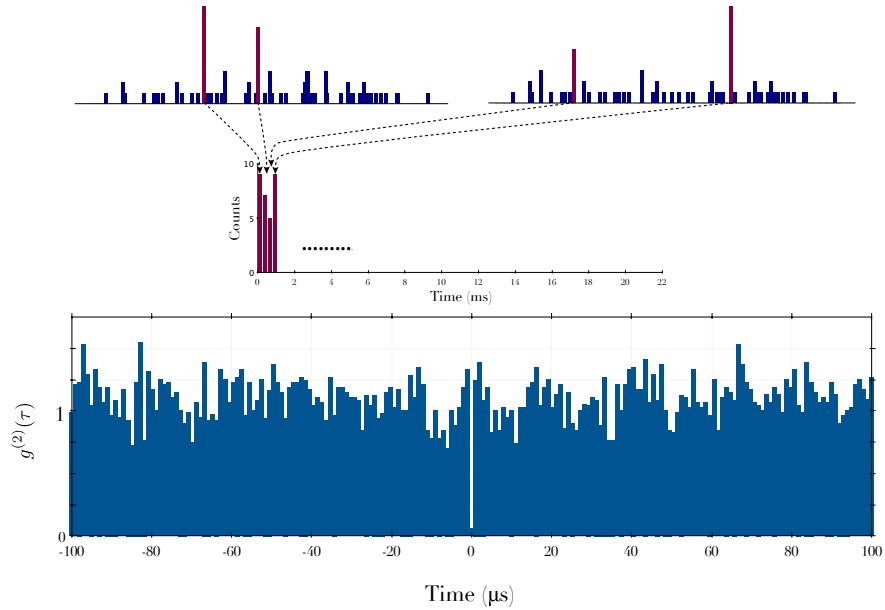


Figure 3.14: Conditioning on the presence of atoms: to simulate the photon statistics of a static source the detector clicks from times when an atom is present in the cavity are concatenated to form a new data set. The  $g^{(2)}(\tau)$  correlation function of this new data is shown over a  $200 \mu\text{s}$  range with one datum per STIRAP pulse. The missing central peak has a visibility of  $\geq 94\%$ .

### 3.5 PHOTON PRODUCTION EFFICIENCY

#### 3.5.1 *Detection Efficiency*

The dynamic nature of the photon pistol means that we must do some data conditioning to determine the true efficiency of the source. If we simply take the number of photons detected and divide by the number of STIRAP pulses

applied to the system we get a value of 0.026 %, an obviously very low number as most of the time the cavity sits empty and nothing happens. This can be clearly seen in Figure 3.11 where only two atoms enter the cavity during the entire 20 ms interaction time. As described in Section 3.3 we define the experiment to be ‘working’ when there is an atom in the cavity, therefore to calculate the efficiency of the ‘working’ source we must condition our analysis on actually having an atom in the cavity.

This conditioning is performed in exactly the same manner as described in Section 3.4, looking for times when there was a spike in the count rate and fitting a Gaussian to the distribution of these counts. We then take the central time of this Gaussian fit as the moment when the atom was centred in the cavity mode (Figure 3.12) and sum the number of photons detected in the surrounding pulses. Dividing this by the total number of conditioning events  $N$  gives a histogram of the probability of the detector firing with respect to the atom’s position within the cavity, Figure 3.15. This can be expressed as,

$$p_{det}(\Delta t) = \frac{1}{N} \sum_{i=1}^N [n(\Delta t) - \bar{n}], \quad (3.3)$$

where  $\Delta t$  is time from the centre of the Gaussian fit and  $\bar{n}$  is the probability of detecting a background count within this time window.

This method of calculating the efficiency is obviously self-referential - we use periods of time in which there is a high photon production efficiency to condition our data and then claim ‘we have a high production efficiency’. In order to limit this problem we must ensure that we condition the data as little as possible. The data shown in Table 3.1 have been conditioned with the requirements that we have observed a single count, two counts, three counts and four counts per 100  $\mu s$ .

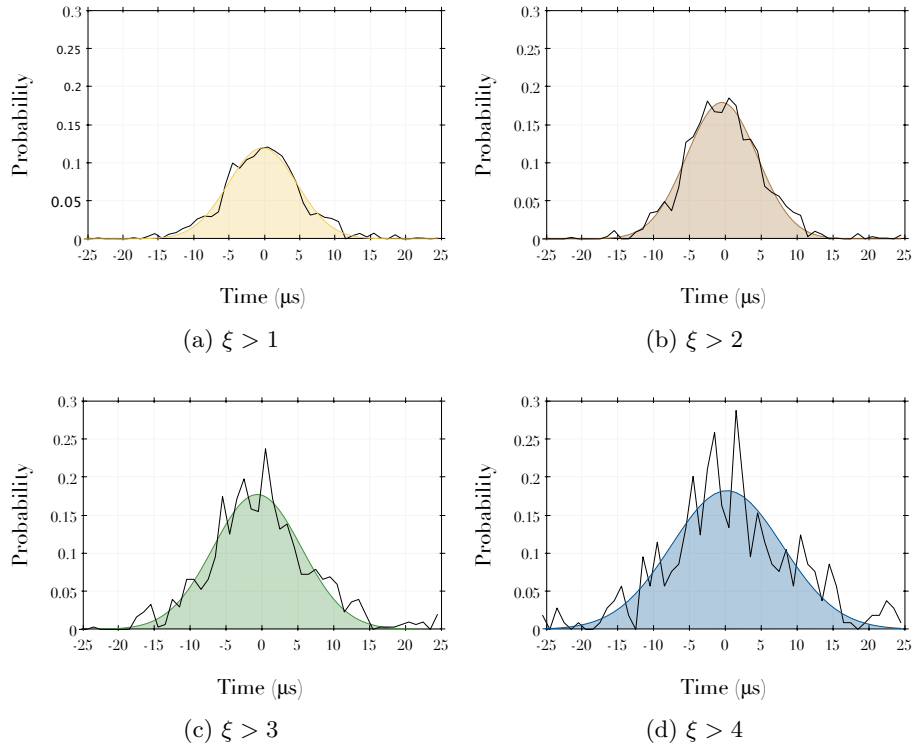


Figure 3.15: Conditioned emission probability: the emission probability is plotted as a function of the atom’s transit across the cavity mode with the conditioning criteria that there were more than 1(a), 2(b), 3(c), and 4(d) counts per  $100 \mu\text{s}$ .

After a marked increase from the no conditioning and ‘single count’ case it is surprising how little the more stringent conditioning requirements change the maximum efficiency. In fact the extra counts seem to be due either to those atoms in the wings of the velocity distribution moving more slowly through the cavity mode, or the atoms emitting photons when poorly coupled rather than an increase in the maximum emission probability. This implies that the photon source must be operating at very high efficiencies: if the emission probability were low, we would expect that the conditioning would filter out those unlikely cases where a photon was emitted with every pulse, resulting in an apparent increase in maximum efficiency.

CONDITIONING CLICKS (PER 100 $\mu\text{s}$ )	-	1	2	3	4
CLICK PROBABILITY (%)	0.03	$12.0 \pm 0.5$	$17.9 \pm 0.7$	$18 \pm 1$	$18 \pm 2$
DISTRIBUTION WIDTH ( $\mu\text{s}$ )	-	$11.5 \pm 0.6$	$11.7 \pm 0.6$	$14 \pm 1$	$18 \pm 3$

Table 3.1: Peak emission probability and distribution width for the conditioning shown in Figure 3.15. These correspond to the emission probability at time  $t = 0$ .

It should be noted that the much reduced atom-cavity interaction time compared with that shown in Figure 3.10 ( $15 \mu\text{s}$  rather than  $100 \mu\text{s}$ ) is deliberate. It is much easier to align the atomic fountain for daily use when the atoms are moving faster as angular misalignments of the fountain have less of an effect. This is easily reversed when a long interaction time is required.

### 3.5.2 Emission Probability

The probabilities that we have been discussing so far have all been probabilities of a photon detection. Whilst these are the probabilities which limit the use of a particular photon source on an experimental level they are also greatly influenced by the technical and experimental details rather than the actual physics of the system in question. The number that we actually care about is the probability of the atom emitting a photon into the cavity mode; this is determined by the dynamics of the system and is the ultimate limit of its usefulness. The ability of the experimentalist to couple light into a fiber, or the amount of money one has to spend on APDs with a high Quantum Efficiency (Q.E.) is important but is secondary to the physics of the atom-cavity system.

To calculate the efficiency of the photon production we must propagate backwards from our measured click efficiency taking into account all of the losses that exist until we can estimate the efficiency of the STIRAP process itself. The two APDs used have Q.E.s of  $77.2 \pm 0.1\%$  and  $60.8 \pm 0.1\%$  respectively. As photons are randomly sent to one or the other of these detectors by the 50/50 beam-splitter we take the mean of the detectors' Q.E.s giving a Q.E. of  $\eta_{det} = 69.0 \pm 0.14\%$ . To measure the losses in the optical path we use the cavity locking beam; when the cavity is locked on resonance this beam passes through the cavity, and, as it is defined by the cavity mode, follows the same path as any emitted photons. We can measure the beam power after the beam has passed through the vacuum chamber windows and again just before the APDs to determine the optical losses. To find the approximate losses as the beam passes through the vacuum chamber viewports we use another beam, displaced slightly from the cavity, and measure the input and output powers. We then assume that the losses occur equally on the input and output viewports and so take half this value.

The combined optics' losses are very variable: fluctuations in the lab temperature and acoustic vibrations which change the coupling into - and the losses in - the optical fibres, as well as dust on the optical surfaces, all conspire such that the optics' losses change daily. We can however put a reasonable estimate of the losses of a clean system as  $\eta_{opt} = 65 \pm 2.5\%$ . If this loss is taken into consideration (Equation 3.4) photons are emitted from the cavity with an efficiency of  $p_{emit} = 40 \pm 5\%$ .

$$p_{det} = \eta_{det} \cdot \eta_{opt} \cdot p_{emit}. \quad (3.4)$$

The final estimation of the photon production efficiency is a little more tenuous but it still deserves to be included for the same reason as before - it applies only to the mechanics of the particular experiment in question

(and the mistakes that we made during construction) not to the physics of the atom-cavity system as a whole. As was mentioned in Section 2.4.1 the cavity mirrors were damaged during the vacuum bakeout and the mirror losses increased dramatically from 2ppm to 18ppm.

These extra losses increase the cavity linewidth  $\kappa$  and reduce the effective asymmetry of the cavity. Figure 2.2a shows that the outcoupling that we could achieve with the designed specification of our mirrors was upwards of 96 %, i.e. for all practical purposes we would collect every photon that was produced in the cavity. The extra mirror losses reduced the outcoupling to  $\eta_{can} = 51 \pm 3\%$ , taking this extra loss into account (Equation 3.5) gives an emission probability into the cavity mode of  $p_{cav} = 79 \pm 9\%$

$$p_{det} = \eta_{det} \cdot \eta_{opt} \cdot \eta_{cav} \cdot p_{cav}. \quad (3.5)$$

This must be compared to the theoretical maximum emission probability  $P_{max} = 2C/(2C + 1)$  of 86% [138].

### 3.5.3 Photon Production Rates

To ensure that there is only ever a single atom in the cavity at any time we deliberately launched very dilute MOT clouds towards the cavity. This means that we observe a very low count rate – typically on the order of 10-30 photon detections per MOT launch, as can be seen in Figure 3.11. Due to this low count rate it was found that we had to launch 4000 MOT clouds to build up sufficient photon statistics – with a cycle time of one launch every 300 ms Figure 3.10 took about 20 minutes to obtain.

It should however be noted that this photon production rate is in no way optimised. As this experiment aims to demonstrate the principles of the

photon source – and as a large scale quantum network is unlikely to be constructed without a permanently trapped atom – optimising the photon production rate was not a primary consideration in either its design or operation.

### 3.6 HONG-OU-MANDEL INTERFEROMETRY

Creating single photons allows us to perform single qubit operations, however for a truly useful quantum device we require multi-qubit operations, i.e. we need to be able to encode information on various separate qubits and have them talk to one another. For this we require the photons to be indistinguishable so that it is possible for interference to occur between them.

#### 3.6.1 *Theory*

In this interferometer two photons are overlapped at a beam-splitter and the correlations between the two detectors at the output ports C and D are observed. This gives rise to a peculiarly quantum effect - due to their bosonic character, the two photons, if they are indistinguishable, will coalesce and leave the beam-splitter through the same output port and no correlations will be observed. If there exists any distinguishability between the two photons, such as a random instantaneous jitter or a systematic effect such as polarisation, some correlations will still be observed. The number and distributions of these correlations can be used to characterise the mutual properties of the two interfering photons.

The effects of this interference can be modelled by considering the creation operators for single photons in the relevant modes. The two input ports A

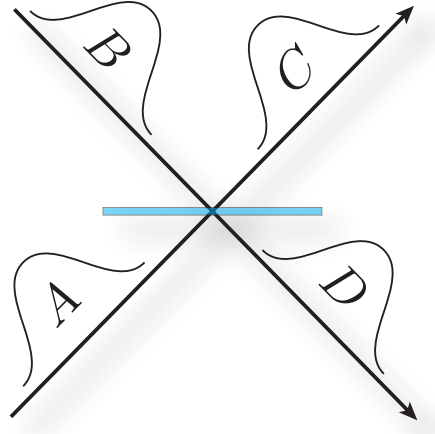


Figure 3.16: Two photon interference: Two photons A and B overlap on a beam-splitter and if indistinguishable will leave through the same output port. As the photons are longer than the detector resolution the photons' shape must be considered.

and B can be transformed into a combination of the two output ports C and D via the relations,

$$\begin{aligned}\hat{a}_A^\dagger &= \frac{1}{\sqrt{2}}(\hat{a}_C^\dagger + \hat{a}_D^\dagger), \\ \hat{a}_B^\dagger &= \frac{1}{\sqrt{2}}(\hat{a}_C^\dagger - \hat{a}_D^\dagger),\end{aligned}\tag{3.6}$$

where  $\hat{a}_X^\dagger$  is the creation operator for a photon in mode  $X$ . The difference in sign between these two equations is due to the phase change upon reflection that is imposed on the photon. If we now consider two photons simultaneously incident on the beam-splitter in the vacuum-state we have,

$$\hat{a}_A^\dagger \hat{a}_B^\dagger |\text{Vac}\rangle.\tag{3.7}$$

Using the relations shown in 3.6 this becomes,

$$\hat{a}_A^\dagger \hat{a}_B^\dagger |\text{Vac}\rangle = \frac{1}{2}(\hat{a}_C^\dagger + \hat{a}_D^\dagger)(\hat{a}_C^\dagger - \hat{a}_D^\dagger) |\text{Vac}\rangle,\tag{3.8}$$

which can be expanded to give

$$\hat{a}_A^\dagger \hat{a}_B^\dagger |\text{Vac}\rangle = \frac{1}{2}(\hat{a}_C^\dagger \hat{a}_C^\dagger - \hat{a}_D^\dagger \hat{a}_C^\dagger + \hat{a}_D^\dagger \hat{a}_C^\dagger + \hat{a}_D^\dagger \hat{a}_D^\dagger) |\text{Vac}\rangle. \quad (3.9)$$

As  $\hat{a}_D^\dagger$  and  $\hat{a}_C^\dagger$  are orthogonal modes they commute reducing the expression to,

$$\hat{a}_A^\dagger \hat{a}_B^\dagger |\text{Vac}\rangle = \frac{1}{2}(\hat{a}_C^\dagger \hat{a}_C^\dagger + \hat{a}_D^\dagger \hat{a}_D^\dagger) |\text{Vac}\rangle \quad (3.10)$$

$$= \frac{1}{\sqrt{2}}(|2_C, 0_D\rangle + |0_C, 2_D\rangle). \quad (3.11)$$

The photons have bunched and have exited the beam-splitter through the same output port. This is the interference that we would like to observe.

Most single photon experiments performed to date probe this indistinguishability by varying the arrival time of the photons onto the beam-splitter. In these sources the photons are very short in time - typically in the picosecond to femtosecond regime - and can be considered as point particles. If the number of correlations between the output ports C and D is monitored when there is a large difference in the photon arrival times (as interference can only occur if the photons interact), one will observe correlations that would be expected by randomly distributing the photons between the two ports. As the difference in arrival times is reduced the photons begin to interact and bunch, reducing the number of correlations. This reaches a minimum when the photons arrive at the same time causing the famous Hong-Ou-Mandel (HOM) dip [139] (Figure 3.17).

The indistinguishability of the two photons is defined as the depth of this dip, i.e. if the number of correlations decreases to half of the non-interacting value we declare the two photon interference visibility to be 50%. As this effect only occurs for indistinguishable photons, if we can force the photons to become distinguishable - whilst still arriving at the same time - we can

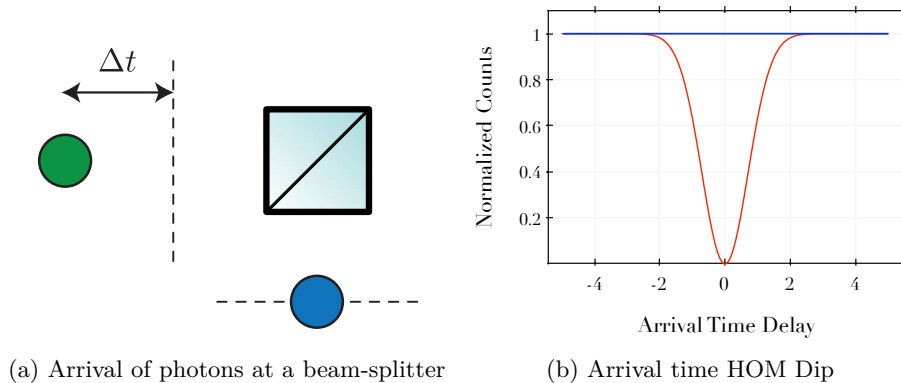


Figure 3.17: Non time-resolved HOM: In most single photon sources the photons cannot be resolved and must be considered as point particles (a). The number of correlations between the beam-splitter output ports when the relative arrival time at the beam-splitter is varied,  $\Delta t$ , is shown for perpendicular (grey) and parallel (red) polarized photons, (b).

measure the difference in the number of correlations without having to alter the photons' arrival times. This can be performed by changing the polarization of one of the photons such that the two photons are perpendicular to one another. The two photon interference visibility can now be described by,

$$V_{2ph} = 1 - \frac{\phi(t)_{\parallel}|_{t=0}}{\phi(t)_{\perp}|_{t=0}}. \quad (3.12)$$

where  $\phi(t)$  is the number of correlations observed as function of photon arrival times for parallel  $\parallel$ , and perpendicular  $\perp$  polarizations.

The photons produced in Section 3.2 are much longer than those usually seen in single photon experiments; they can be up to several microseconds long which corresponds to hundreds of metres. With these photons we only consider the situation when both photons arrive at the beam-splitter at the same time. Unlike with point particles, the photons' length can be comparable with the coherence time so it is possible to obtain the value of this coherence time along with the two-photon visibility  $V_{2ph}$  from a single measurement.

This is because the HOM interference described above had a photon length that was less than the detector resolution  $T_{ph} < t_R$ , i.e. one could not temporally resolve the photon. In our time-resolved case however the photons are very much longer than the detector resolution,  $\sim 1 \mu s \gg 50ps$ , and we have another degree of freedom to take into account - the photons' shape (Figure ??).

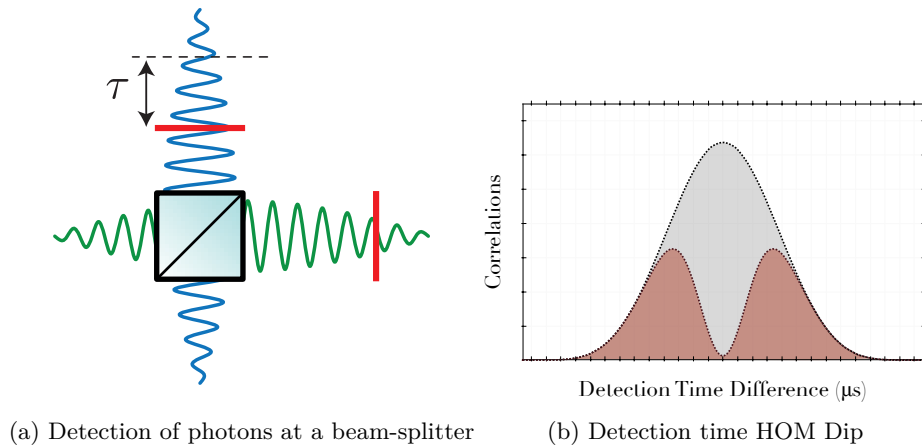


Figure 3.18: Time-resolved HOM: As the photons are very long compared with the detector resolution they can no longer be considered point particles. The photons arrive at the beam-splitter at the same time however they can be detected in different parts of the envelope. The difference in time between these detections  $\tau$  is shown for perpendicularly (grey) and parallel (red) polarized photons

As the photons are now taken to be extended objects, we will observe a time dependence in the number of correlations even when the photons arrive at the same time. If the photons are Gaussian in shape (with a wavepacket duration defined by the full-width at  $1/e$  maximum of  $t = T_1$ ) then for perpendicularly polarised photons the time dependent interference will be defined by the convolution of the two arriving photons,

$$\Phi(\tau)_{\perp} = \frac{1}{2\sqrt{\pi}} e^{-\tau^2/T_1^2}, \quad (3.13)$$

and parallel polarised photons will have the form,

$$\Phi(\tau)_{\parallel} = \frac{1}{2\sqrt{\pi}} e^{-\tau^2/T_1^2} \cdot [1 - e^{-\tau^2/T_2^2}]. \quad (3.14)$$

$\Phi(\tau)$  is the number of correlations at a particular detection time  $\tau$ , the coherence time  $T_2 = 2/\delta\omega$  depends of the jitter in the photons' frequency  $\delta\omega$  [115]. This time dependence of the two photons' interference is covered in more detail in Section 5.1.1. The two photon visibility of time resolved photons can be described in the same way as Equation 3.12, one simply integrates over the detector time delay to obtain,

$$V_{2ph} = 1 - \frac{\int \Phi(\tau)_{\parallel} d\tau}{\int \Phi(\tau)_{\perp} d\tau}. \quad (3.15)$$

### 3.6.2 Experimental Demonstration

In order to test the indistinguishability of photons that are produced by the same source we must interfere two successive photons with one another. As the photons are emitted with a repetition rate of 1 MHz we have to catch a photon and then delay it by  $1 \mu\text{s}$  to overlap it with a photon emitted in a subsequent pulse. This is done with optical paths of different lengths, one long, one short, such that the length difference between them is  $\Delta d = (\frac{c}{n}) \cdot t_{rep}$ , where  $n$  is the refractive index of the material through which the photon is travelling. In free space with  $n = 1$  (a reasonable approximation for light in air), the path length difference must be  $\Delta d = 300 \text{ m}$ , which is not an easy proposition. To achieve these long delay lines we therefore use a long 200 m single mode, polarization maintaining optical fibre (*Nufern - 780 PM*)

A simplified outline of the experimental arrangement is shown in Figure 3.19. The photon stream is split equally down the upper (long) and lower

(short) beam paths by a polarizing beam-splitter (PBS), and the polarization of the photons is aligned to the birefringent axis of the polarization maintaining fibre using zero-order half-wave plates (HWP) and adjustable fibre couplers (Schäfter and Kirchhoff *60FC*).

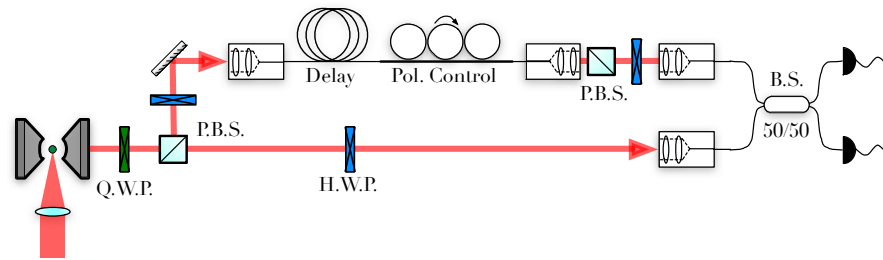


Figure 3.19: HOM interferometer: A 200 m long fibre is used to delay one photon such that it can be overlapped with the subsequently emitted one. A fibre-based beam-splitter and polarization optics are used to ensure near-perfect spatial and polarization overlap.

In order to achieve a good interference pattern between two photons their spatial, temporal and polarization modes must overlap perfectly. Spatial overlap is provided by the single mode fibres that the photons propagate in, which ensures overlap of the photon wavepackets both at the fibre-beam-splitter (*Newport F-CPL-2x2-OPT-55-21-55*) and at the detectors. Any deviation of the polarization from parallel will lead to a washing-out of the interference dip, so we must take a great deal of care to ensure this cannot occur. Polarization overlap is ensured using the two polarising beam-splitters shown in Figure 3.19.

A polarization maintaining fibre, although designed to allow propagation of light without changing the polarization, requires careful alignment - any deviation of the input polarization from the birefringent axis will result in polarization drifts over time. Stresses applied to the fibre, for example through temperature changes or air currents, will increase the rate at which this happens. The effects of this can be removed by adding a polarization

filter after the fibre delay line. This consists of a fibre polarization controller and a 10,000:1 polarising beam-splitter placed in the photons' path. The filter ensures that the photons are always correctly polarized no matter what polarization rotations occur in the delay line as any photons that are incorrectly polarized will simply be reflected out of the interferometer onto a beam dump. Polarization rotations therefore simply reduce the count rate and thus increase the measurement time, rather than washing out the interference. The settings of the fibre polarizer are optimized by maximising the transmission of the cavity locking beam through the filtering PBS. Once this is done measurements can be taken for approximately 20 minutes before the polarization must be checked and optimized again.

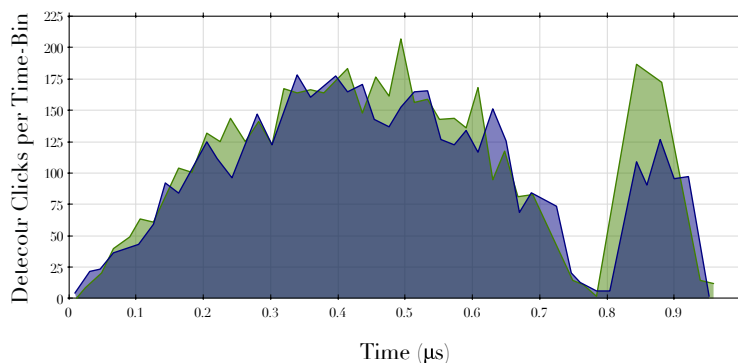


Figure 3.20: Time-binned photon arrival times showing the overlap of the photons: travelling down the long and short arm of the interferometer: The repetition rate of the photon production must exactly match the delay imposed by the interferometer in order to perfectly overlap the photons. To illustrate this we have here deliberately imposed a timing mismatch to cause an arrival time difference of 20 ns between the un-delayed photon (green) and the delayed photon (blue).

Temporal overlap, i.e. getting two photons onto the beam-splitter simultaneously, is achieved by delaying the emission time of the second photon to the exact time that it takes for the first photon to traverse the fibre delay-line. This delay is easily monitored by blocking the two optical paths (long and short) in turn and then looking at the arrival times of the photons - if they

are the same then  $\Delta t = 0$  and a maximal interference should be observed. This is shown in Figure 3.20 - the green line shows the photons which have gone directly to the detectors and the blue line shows the photons which have passed down the delay line. By looking at the sharp increase in count rate at the onset of the re-pump pulse it is clear that the delayed photons arrive at the detectors 20 ns after the photons which take the shorter path. Using this information the emission time of the photons can be changed to achieve temporal overlap. Care must be taken to ensure that no external timing delays are introduced between the detectors and the TDC by cables of different lengths, or by the attenuators required on the detector output, as these can cause a systematic error in the timings ([140], please say it's isn't, *edit in corrections: oh well, it was nice while it lasted!*).

### 3.6.3 Results

The cross-correlation between the two detectors is shown in Figure 3.21. With perpendicular polarization the photons do not interfere and a correlation function given by the convolution of the shapes of the two photons is observed, whereas with parallel polarization the photons interfere and the number of correlations is greatly reduced. As the atom loading is a stochastic process the observed correlations are normalized by comparing the number of correlations in the first  $g^{(2)}(\tau)$  peak. Although it should also be possible to observe these 'bunched' photons directly by plotting the autocorrelation of the individual detectors, the after-pulsing of the SPCMs (Section 2.5.3) prevents this.

The indistinguishability of the two photons, and hence their suitability for use in quantum interference experiments, is defined by the two-photon visibility (Equation 3.15). This is the fractional change in the total number

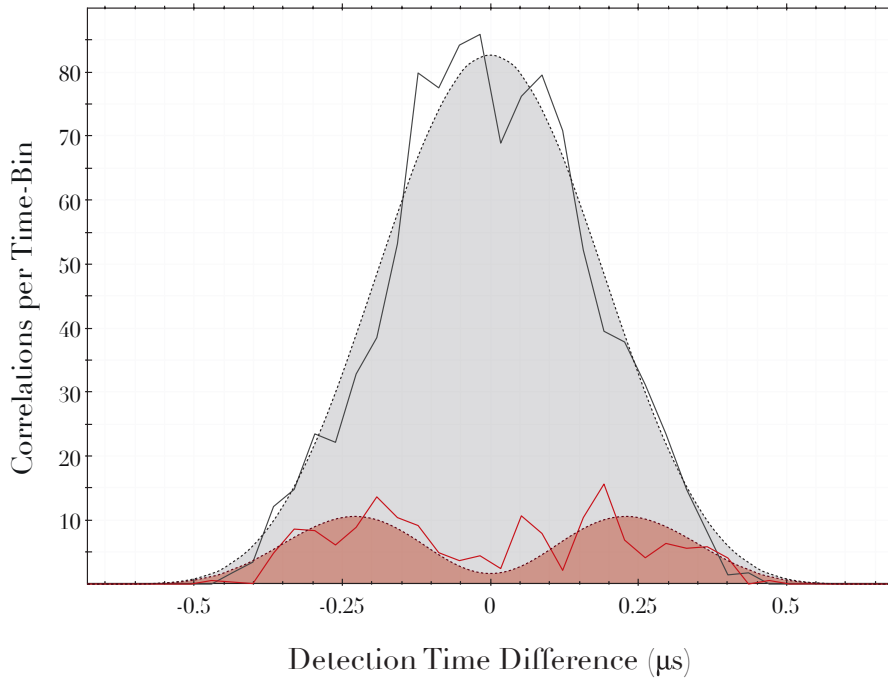


Figure 3.21: Two photon interference: Cross correlation function of the detector time delay  $\tau$  is shown for perpendicular polarized photons (solid grey line) and parallel polarized photons (solid red line), along with the relevant theoretical fit (shaded). The two photon visibility is  $V_{2ph} = 0.87$  and the coherence time is  $T_2 = 0.48 \pm 0.06 \mu\text{s}$ .

of correlations observed in the perpendicular and parallel cases and is equal to  $V_{2ph} = 0.87 \pm 0.05$ .

The width of the central minimum in the parallel photon case is caused by the two photon coherence time (HW1/eM) as  $T_2 = 0.48 \pm 0.06 \mu\text{s}$ . This coherence time can either arise from a frequency jitter of the photons' carrier frequency of  $\delta\omega = 2\pi \cdot (0.65 \pm 0.09) \text{ MHz}$  or a jitter in the photon emission time. The jitter in the photon emission time would have to be about  $1 \mu\text{s}$  to cause this effect and with the results shown in Section 4.5 this is unlikely. As the transform-limited bandwidth of these photons is 300 kHz, the remaining inhomogeneous broadening must be due to external sources, such as stray magnetic fields, the frequency stability of the STIRAP laser ( $\sim 300 \text{ kHz}$ ) or drift of the cavity length.

In the preceding discussion we have assumed that the photons exist as pure states and so the HOM visibility is solely due to photon indistinguishability. This assumption is justified by the post-selection of photons from well-coupled atoms and polarisation filtering of any fibre-induced rotations, as well as by the singleness of the emitted photons (Figure 3.10). However it should be noted that a lack of visibility can be caused by multi-emission events as well as impurity of the emitted photons [141].

### 3.7 CONCLUSION

We have demonstrated a cavity-based single-photon source. Emission rates of 1 MHz can be achieved and the lack of disturbances caused by trapping fields means the source exhibits peak photon production efficiency into the cavity of nearly 80%. Despite the lack of a trap individual atoms can remain inside the cavity mode for up to  $100 \mu\text{s}$  which provides sufficient time for potential QIP operations both with the emitted photons and the atoms themselves. The photons were characterized using Hanbury Brown Twiss and Hong Ou Mandel interferometry. They showed strong anti-bunching with a HBT visibility of  $V_{HBT} > 94\%$ , which is suspected to be limited by background noise, and a high indistinguishability with a HOM visibility of  $V_{2ph} = 87\%$ .

Recent results from other C-QED sources based on neutral atoms in dipole traps give an indistinguishability similar to that observed here  $V_{2ph} = 85\%$  [118], but with a repetition rate of  $f_{rep} = 0.1 \text{ MHz}$  and a reduced efficiency of  $P_{emit} = 7-9\%$  [106]; a source has been produced with high efficiency  $P_{emit} = 69\%$  and repetition rate  $f_{rep} = 0.1 \text{ MHz}$ , however its indistinguishability was not tested [104]. Photons from trapped ions in cavities have shown either

high efficiencies,  $P_{emit} = 88\%$  with low repetition rates,  $f_{rep} = 0.002$  MHz [142], or the inverse  $P_{emit} = 8\%$ ,  $f_{rep} = 0.1$  MHz [107].

Currently the dominant photon source used in single photon experiments is a heralded photon pair produced by parametric down-conversion. These sources have shown excellent indistinguishability,  $V_{2ph} = 84/94\%$ , and single-ness,  $V_{HBT} = 99\%$ , however they suffer in emission probability. The emission of a photon in these sources is a stochastic process, so as with the atom loading in our experiment, the emission probability of a single photon must be kept low so that the probability of emitting more than one photon is also minimised. Although this is counteracted by the high heralding efficiencies,  $P_{Herald} = 85/44\%$ , the probability of emitting a photon per attempt is only  $P = 0.001$  [141, 143].

The properties of the demonstrated source therefore compare very well both with similar C-QED sources and with single photons from heralded pair sources. Although the photon production mechanism from trapped neutral atom and ion sources is identical - a vacuum Raman transition - the convenience of a stationary source has a price to pay in the efficiency and indistinguishability of the photons; as we avoid this penalty we can achieve near deterministic operation, conditioned on the presence of an atom. Although the efficiency of heralded sources is comparable to that demonstrated here, the significantly lower emission probability per attempt causes problems when multiple successive photons are required as the probability of emitting  $n$  photons scales as  $P^n$ . It is again the near deterministic emission which circumvents the problem for the demonstrated source.

We should note that to be truly deterministic a source must be able to produce, with a probability of 1, a single photon with perfectly defined frequency, spatio-temporal mode, polarisation and phase. Sadly such a device is impossible, it is the Platonic ideal of a photon source.

For our atom-cavity source the primary (although not only) reason for this lack of determinism is the practical considerations of placing an atom within the cavity. Whilst an atom is perfectly located at the centre of the cavity mode the system should act as a near deterministic source, however the stochastic atom loading limits the 'up-time' of the experiment in which an atom is in the cavity. Within the confines of an academic experiment designed to prove the versatility of a photon source this is an acceptable limitation, though this problem must be solved to achieve truly deterministic operation.

## Part II

### MAKING THESE PHOTONS DO SLIGHTLY ODD THINGS

In the preceding chapters we presented the construction and characterisation of a deterministic atom-cavity photon source. Now that we have this large collection of optics and electronics in place we would like to study the control which can be exerted over these photons in slightly more depth. To this end we will demonstrate control over the photons' amplitude, frequency and phase.



## CONTROLLING A PHOTON'S AMPLITUDE

---

In this chapter control over the amplitude of the photon's temporal mode, i.e. its 'shape' is implemented. In previous work on trapped ions [107], it has been shown that the amplitude of the single photons produced by a C-QED source can be replicated theoretically. We now show that it is possible to *a priori* define an arbitrary photon shape and then produce it.

An outline of the method used to calculate the required STIRAP pulse for an arbitrary photon shape is shown in Section 4.1. In Section 4.2 the photon production is simulated using a realistic system; it is shown that the three level system that this method relies upon provides a reasonable approximation for the purposes of this experiment. The variability in the emitted photon shapes which is introduced by the imprecise loading of an atom into the cavity is discussed in Section 4.3 and removed in Section 4.4. Finally single photons with a variety of shapes are produced in Section 4.5.

### 4.1 CALCULATING A STIRAP PULSE

We will begin by simplifying the problem to its fundamentals. We have an atom interacting with some light and this atom should produce a photon; we would like to calculate the dynamics of this process so that we can perform it in the lab. The atom (to a reasonable first approximation) can exist in three levels: the initial state, an excited state through which the Raman transition

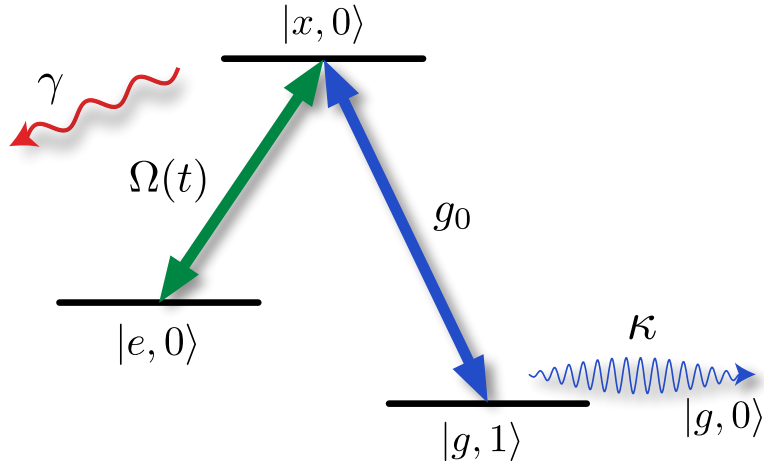


Figure 4.1: The STIRAP process occurs between three levels consisting of two atomic ground states  $u$  and  $g$  and the excited state  $x$  and the cavity photon population  $n$ . There are two decay processes: the free-space atomic decay  $\gamma$  and the cavity decay  $\kappa$ .

occurs, and the final state to which the atom is pumped. We do not care where these levels come from we just note that they exist.

The atom experiences a coupling to the vacuum field of the cavity. Whilst this could in principle be a dynamic coupling we assume that it is not; that the atom is at rest inside the cavity, and the cavity itself is stable with no frequency drifts. The other coupling that the atom feels is an electric dipole interaction with a laser. Unlike the interaction with the cavity, we have complete control over this coupling as the laser beam can be modulated in phase, frequency and amplitude by an AOM at timescales much shorter than the photon length. In this chapter however we will confine ourselves to modulation of the amplitude. Finally we consider the system's two decay processes: a spontaneous decay of the atoms' excited state and the decay of the photon population out of the cavity.

### 4.1.1 A Simple Three Level System

To formalize this, consider a three level system,  $|e\rangle, |x\rangle, |g\rangle$  shown in Figure 4.1. The laser pulse (which has a time dependent Rabi frequency  $\Omega(t)$ ) drives the transition  $|e\rangle \leftrightarrow |x\rangle$ , the constant vacuum field coupling  $g_0$  is resonant with  $|x\rangle \leftrightarrow |g\rangle$ , and the direct  $|e\rangle \leftrightarrow |g\rangle$  transition is forbidden. In practice this will be formed by using the hyperfine levels  $F = 2$  and  $F = 1$  of the  $5^2S_{1/2}$  manifold in  $^{87}Rb$  for the ground states and the  $F' = 1$  state in the  $5^2P_{3/2}$  manifold for the excited state, however any similar 3-level system would suffice. The full Hilbert space of the system is spanned by including the photon population of the cavity which can take any value from 0 to  $\infty$ .

We curtail the number of possible states with limits imposed by energy conservation: the photon population is constrained to the two Fock states  $|n\rangle = \{|0\rangle, |1\rangle\}$  (assuming we initially populate  $|e, 0\rangle$ ), and the  $|e, 1\rangle$  and  $|x, 1\rangle$  states cannot exist. As the cavity has a finite lifetime it is obvious that in practice  $|g, 1\rangle$  will decay to  $|g, 0\rangle$ , i.e. the photon will leak out of the cavity mirrors. This extra state can be ‘simplified away’ by assuming that the system works in only one direction - from  $|g, 1\rangle \rightarrow |g, 0\rangle$  and that  $\kappa^{-1}$  is much shorter than the photon length  $T_{ph}$ . In this case  $|g, 0\rangle$  and hence the photon wave-packet  $\psi_0$  will exactly follow  $|g, 1\rangle$ . Both this cavity decay and the spontaneous decay of the excited state  $\gamma$  are included in the system’s Hamiltonian phenomenologically by the use of imaginary decay terms along the diagonal. As a result of these simplifications the Hilbert space of the system can be fully spanned by the the states  $|e, 0\rangle, |x, 0\rangle, |g, 1\rangle$ .

The atom-cavity system is described by the Schrödinger Equation,

$$i\hbar \frac{d}{dt} \mathbf{c}(t) = -\frac{\hbar}{2} \begin{pmatrix} 0 & \Omega(t) & 0 \\ \Omega(t) & 2i\gamma & 2g \\ 0 & 2g & 2i\kappa \end{pmatrix} \mathbf{c}(t), \quad (4.1)$$

where  $\mathbf{c}(t) = [\mathbf{c}_e(t), \mathbf{c}_x(t), \mathbf{c}_g(t)]^T$  are the probability amplitudes for the states  $[|e, 0\rangle |x, 0\rangle |g, 1\rangle]$ .

#### 4.1.2 An Analytic Solution

Now that we have defined the Hamiltonian, calculating the required Rabi frequency to generate a photon of a shape  $\psi_0$  is relatively straightforward (using the method described in [138]). We start by writing out the set of coupled equations described by Equation 4.1

$$i\dot{\mathbf{c}}_e(t) = \frac{1}{2} \Omega(t) \mathbf{c}_x(t), \quad (4.2)$$

$$i\dot{\mathbf{c}}_x(t) = \frac{1}{2} \Omega(t) \mathbf{c}_e(t) + i\gamma \mathbf{c}_x(t) + g \mathbf{c}_g(t), \quad (4.3)$$

$$i\dot{\mathbf{c}}_g(t) = g \mathbf{c}_x(t) + i\kappa \mathbf{c}_g(t), \quad (4.4)$$

which, from Equation 4.2 gives an expression for the Rabi frequency,

$$\Omega(t) = -2i \frac{\dot{\mathbf{c}}_e(t)}{\mathbf{c}_x(t)}. \quad (4.5)$$

As  $\kappa^{-1} \ll T_{ph}$ ,  $\mathbf{c}_g(t)$  will be directly proportional to the shape of the photon that we are trying to produce; we can write the amplitude of the state  $|g, 1\rangle$  at all times as,

$$\mathbf{c}_g(t) = \frac{\sqrt{\eta} \psi_0}{\sqrt{2\kappa}}. \quad (4.6)$$

The factor of  $\sqrt{\eta}$  corresponds to the efficiency of the photon production process. Once we have found  $\mathbf{c}_g(t)$ , we can calculate  $\mathbf{c}_x(t)$  by re-arranging Equation 4.4,

$$\mathbf{c}_x = -\frac{i}{g} [\dot{\mathbf{c}}_g(t) + \kappa \mathbf{c}_g(t)]. \quad (4.7)$$

This takes us halfway to being able to analytically calculate the required driving pulse: we now need to calculate  $\mathbf{c}_e(t)$ . As we cannot obtain a clear expression for  $\mathbf{c}_e(t)$  from the Hamiltonian we must take a different approach using the diagonal elements of the density matrix, i.e. the population.

The population in this system must always equal unity. As there is only ever one excitation, all that happens during any system dynamics is that this excitation is shuffled around the various possible levels, or perhaps lost via an irreversible decay. The population in the state  $\rho_{ee} = \mathbf{c}_e(t)\mathbf{c}_e^*(t)$  is therefore equal to unity minus the population in the other two levels, minus the amount of excitation lost via the decay processes.

$$\rho_{ee}(t) = 1 - \rho_{xx}(t) - \rho_{gg}(t) - \int_0^t dt' [2\gamma\rho_{xx}(t') + 2\kappa\rho_{gg}(t')]. \quad (4.8)$$

To obtain an expression for  $\mathbf{c}_e(t)$  we note that the photon shape  $\psi_0$  is real, and so is  $\mathbf{c}_g(t)$ . Due to the lack of any detunings in the Hamiltonian (Equation 4.1) one can verify that  $\mathbf{c}_x(t)$  must be purely imaginary and  $\mathbf{c}_e(t)$  purely real, and therefore  $\mathbf{c}_e(t) = \sqrt{\rho_{ee}}$ , leaving us with

$$\Omega(t) = -2i \frac{\dot{\mathbf{c}}_e(t)}{\mathbf{c}_x(t)} = -i \frac{\dot{\rho}_{ee}(t)}{\mathbf{c}_x(t)\sqrt{\rho_{ee}(t)}}. \quad (4.9)$$

This algorithm is a completely analytic method for finding the shape of the driving pulse required to produce a photon of shape  $\psi_0$  for any given set of parameters  $\{g, \kappa, \gamma, \eta\}$ .

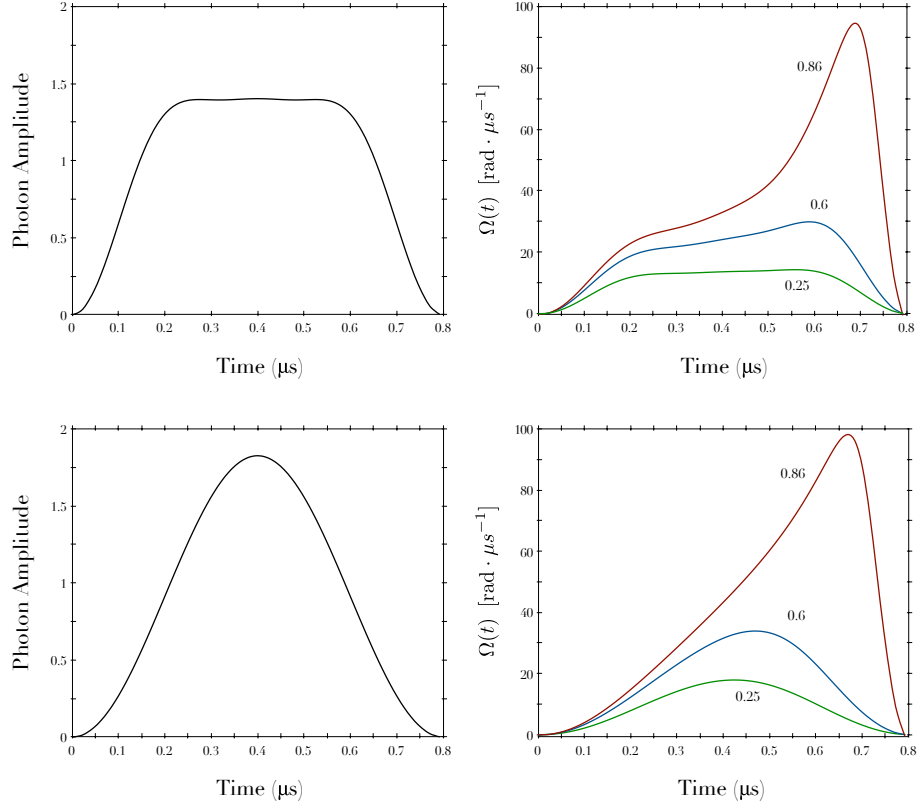


Figure 4.2: Shaped STIRAP Pulses: The left-hand figures show desired single photon wave functions and the corresponding right-hand plots show the required Rabi frequency of the STIRAP driving pulse. The driving pulses have been calculated for three efficiencies  $\eta = (0.25, 0.6, 0.86)$  with  $(g, \kappa, \gamma) = 2\pi \cdot (15, 12, 3)$  MHz and  $T = 0.8 \mu\text{s}$ .

We can now apply this algorithm to calculate the STIRAP pulse required to produce photons which might be of use for QIP, for example a time-symmetric photon with a sine-squared wave-packet  $\psi_0 = \sqrt{\frac{8}{3T}} \sin^2(\pi t/T)$ , or a ‘square’ wave-packet  $\psi_0 = \sqrt{\frac{10}{9T}} [\sin^2(2\pi t/T) + 1.19 \sin^7(\pi t/T)]$  (Figure 4.2). These pulse shapes have been calculated using the parameters of this experiment for a range of efficiencies. At low efficiencies it can be seen that the STIRAP pulse closely follows the desired photon shape, however as the efficiency of the process increases the system must be driven harder to maintain the required population transfer. A singularity is eventually reached when the initial state

$\rho_{ee}(t)$  is completely depleted, which for long photons ( $T_{ph} \gg \kappa^{-1}, g^{-1}$ ) is independent of the photon's shape,  $\eta = 2C/(2C + 1)$ .

## 4.2 NUMERICAL SIMULATION OF RUBIDIUM

In order to calculate the shape of the STIRAP pulse with which to drive the atom, we had to assume that the atom-cavity system was well described by a three level system. In our experiment however, the situation is not so simple. Rubidium has an excited state manifold with four possible hyperfine levels, this further decomposes into twenty  $m_F$ -states, all of which can be off-resonantly excited by either the laser or the cavity mode. In addition to this the decay processes, unlike those in the analytic model, do not remove the excitation from the system; if the atom decays from state  $|x\rangle$  it can fall back into the state  $|e\rangle$  and continue to influence the system dynamics. A more complete picture of the time-evolution of the atom-cavity system must therefore be examined to ensure that the desired photons are correctly produced. To do this we simulated the system using a Master Equation approach [144].

### 4.2.1 *The Hamiltonian*

We start by taking the standard Jaynes-Cummings Hamiltonian of a two-level atom interacting with a cavity mode and extend it to the three-level case. The Hamiltonian can be thought of as the combination of a static background and a term which describes the interactions of the system,

$$\hat{H} = \hat{H}_{stat} + \hat{H}_{int}. \quad (4.10)$$

The static term  $\hat{H}_{stat}$  includes the energy levels of the atom and the cavity,

$$\hat{H}_{stat} = \hat{H}_{atom} + \hat{H}_{cav}, \quad (4.11)$$

and for the three level system can be written in the interaction picture as,

$$\hat{H}_{stat} = \hbar \left( \Delta_{ee}|e\rangle\langle e| + \Delta_{gg}|g\rangle\langle g| \right) + \hbar\Delta_{aa} (\hat{a}^\dagger\hat{a}), \quad (4.12)$$

where  $\Delta_{ii}$  is the detuning from the rotating frame and  $i \in \{g, e\}$ , and  $\hat{a}^\dagger$  and  $\hat{a}$  are the creation and annihilation operators for a photon in the cavity mode.

The interaction part of the Hamiltonian which contains the dynamics of the system's evolution is given by

$$\begin{aligned} \hat{H}_{int} = \hbar\Omega(t) \left[ \Delta_{ex}\mathcal{A}_{e,x}(\hat{\sigma}_{e,x} + \hat{\sigma}_{e,x}^\dagger) + \Delta_{gx}\mathcal{A}_{g,x}(\hat{\sigma}_{g,x} + \hat{\sigma}_{g,x}^\dagger) \right] + \dots \\ \hbar g \left[ \Delta_{ex}\mathcal{A}_{e,x}(\hat{\sigma}_{e,x}\hat{a}^\dagger + \hat{\sigma}_{e,x}^\dagger\hat{a}) + \Delta_{gx}\mathcal{A}_{g,x}(\hat{\sigma}_{g,x}\hat{a}^\dagger + \hat{\sigma}_{g,x}^\dagger\hat{a}) \right], \end{aligned} \quad (4.13)$$

where  $\hat{\sigma}_{e,x}$  and  $\hat{\sigma}_{e,x}^\dagger$  are the atomic creation and annihilation operators for the transition  $i \rightarrow j$  and  $\mathcal{A}_{i,j}$  is the relevant dipole matrix element [123].

For the sake of clarity and brevity the preceding equations have been limited to the initial three level system. The extension of this Hamiltonian to the full  $^{87}\text{Rb}-D_2$  line (shown in Figure 4.3) is achieved in an identical way; the resulting Hamiltonian is simply larger. In addition to all the atomic levels we must also include the fact that the Fabry-Perot cavity is not well described by a single cavity mode, but instead supports two degenerate modes of orthogonal polarisation, with creation operators  $\hat{a}^\dagger$  and  $\hat{b}^\dagger$  respectively. The complete Hamiltonian is therefore given by

$$\hat{H}_{stat} = \hbar \left( \sum_i \Delta_i |i\rangle\langle i| + \Delta_c (\hat{a}^\dagger\hat{a} + \hat{b}^\dagger\hat{b}) \right), \quad (4.14)$$

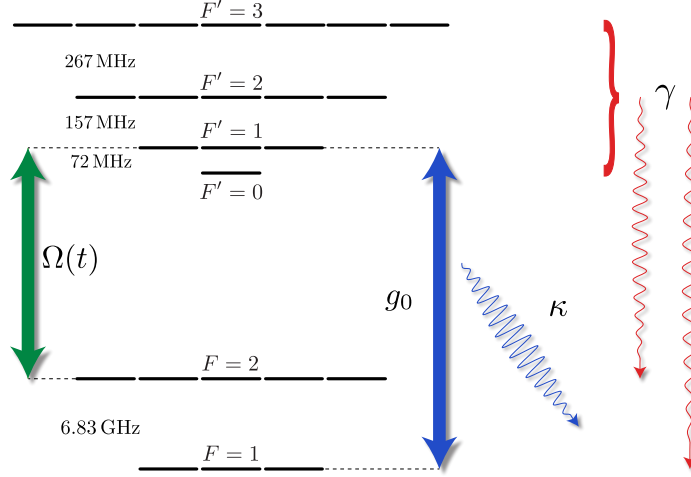


Figure 4.3: Complete energy level structure of the  $^{87}\text{Rb}$   $D_2$  line.

$$\hat{H}_{int} = \sum_{i,j} \hbar \left( \Omega \left[ \Delta_{ij} \mathcal{A}_{i,j} (\hat{\sigma}_{i,j} + \hat{\sigma}_{i,j}^\dagger) \right] + g \left[ \Delta_{ij} \mathcal{A}_{i,j} (\hat{\sigma}_{i,j} \hat{a}^\dagger + \hat{\sigma}_{i,j}^\dagger \hat{a}) \right] \right). \quad (4.15)$$

The time evolution of this system, including its decay processes, can be calculated using the Linblad form of the Master Equation,

$$\frac{d}{dt} \hat{\rho} = -\frac{i}{\hbar} [\hat{H}, \hat{\rho}] + \mathcal{L}[\hat{\rho}], \quad (4.16)$$

where  $\hat{\rho}$  is the density matrix and  $\mathcal{L}[\rho]$  is the Liouville super-operator. This relies on the assumptions that the process is Markovian (i.e. the environment into which information decays is sufficiently large that over the timescales concerned it will not interact with the system again), and that it is at zero temperature (so it is not influenced by input of excitation from the background). As the environment is the infinite set of free-space electromagnetic modes and the transitions are well above the room-temperature black-body spectrum these assumptions are justified. The Liouville operator describes the non-

unitary decay processes via the Decay operator  $\mathcal{D}[c]\rho = 2\hat{c}\rho\hat{c}^\dagger - \hat{c}^\dagger\hat{c}\rho - \rho\hat{c}^\dagger\hat{c}$ , and takes the form,

$$\mathcal{L}[\rho] = \kappa\mathcal{D}[a]\rho + \kappa\mathcal{D}[b]\rho + \gamma\mathcal{D}[\sigma]\rho. \quad (4.17)$$

#### 4.2.2 Results

The populations of the atomic levels during the photon production process are shown in Figure 4.4. For this simulation we assumed that the atom was prepared in an equal mixture of all the  $m_F$  sub-levels of the  $F = 2$  ground state and was driven with a Rabi frequency calculated from Section 4.1.2 to produce a  $\psi(t) = \sin(t)^2$  photon with an efficiency of  $\eta = 0.8$ .

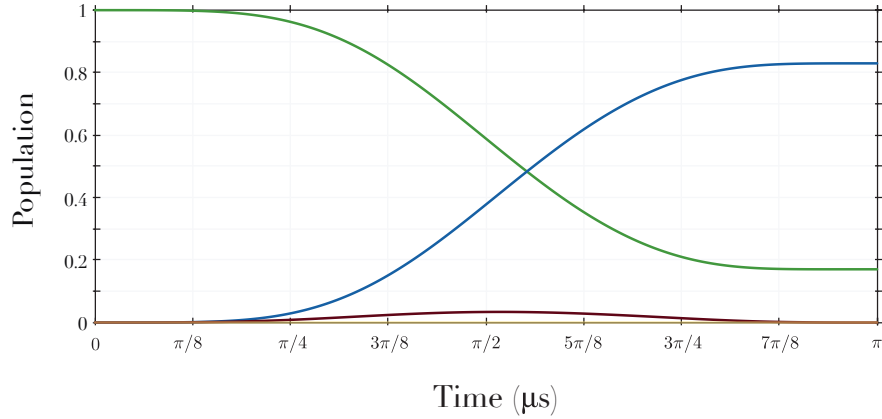


Figure 4.4: Time evolution of the atomic populations: The population of the atom, which is initially prepared in the  $F=2$  ground state (green), is pumped via a Raman transition to the  $F=1$  ground state (blue). A small population is transferred to the  $F'=1$  excited state (red), but the  $F'=0,2,3$  states are negligibly populated (yellow).

The most obvious result is that the addition of all the excited states does not influence the dynamics; the  $\sim 100\text{MHz}$  detunings, along with the low power STIRAP laser, mean that the excited states are too far away to off-resonantly influence the three level sub-system. Rather than the additional

atomic levels, it is the inclusion of the spontaneous atomic decay that causes the greatest deviation. By allowing the population in the excited state  $|x\rangle$  to

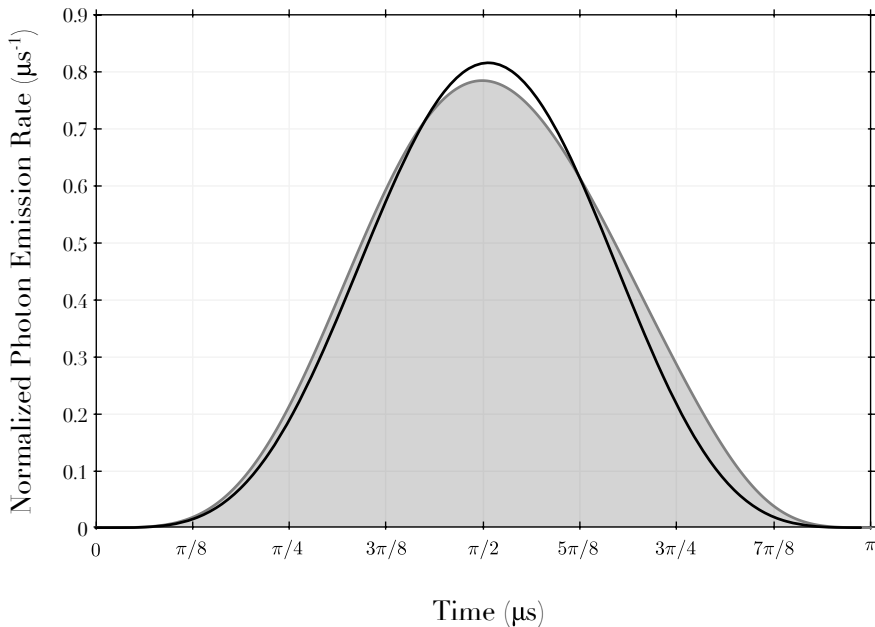


Figure 4.5: Emitted photon shape: The shape of the photon produced by a simulation of a realistic atom-cavity system (grey) is slightly different from the shape calculated using a three-level approximation (black). This is due to the spontaneous decay from the excited state  $|x\rangle$  replenishing the initial state population  $|e\rangle$ . The photon shapes have been normalised such that  $\int \psi_0 dt = 1$ .

decay back to the initial state  $|e\rangle$  we increase the efficiency of the photon production process (incoherently) from 80% to 83%. This can also be seen in the shape of the photon that leaks out of the cavity (Figure 4.5) as the photon emission rate is increased at later times. The population that was excited to state  $|x\rangle$  has decayed back to the initial state and can continue to contribute to the system dynamics. This distorting effect on the photon's shape, however, is small compared to that caused by the atomic fountain, which will be described in subsequent sections. The simulation was performed in MATLAB using the Quantum Optics Toolbox developed by Sze Tan [145].

## 4.3 VARIATIONS FROM THE FOUNTAIN

All of the simulations thus far have been performed under the assumption that we have a completely stationary single atom located at the very centre of an anti-node of the cavity. In reality this is almost never the case. As the atoms are loaded into the cavity using a fountain, by the time the atom cloud has reached the cavity mode it is approximately 5 mm in diameter, considerably larger than the  $20\ \mu\text{m}$  waist, the  $75\ \mu\text{m}$  length of the cavity mode, and the  $14\ \mu\text{m}$  waist of the the STIRAP beam.

This problem is further compounded by the fact that the cavity mode exists as a standing wave along the cavity axis; the maximum atom-cavity coupling will only be experienced at the  $\lambda/2 = 390\ \text{nm}$  spaced anti-nodes. As this is a localisation that is five orders of magnitude less than the accuracy of the atom localisation from the fountain, interactions at all values of  $g$  and  $\Omega$  from  $\{g, \Omega\} = \{0, 0\} \rightarrow \{g_0, \Omega_{max}\}$  will be obtained. This variation can be clearly seen by looking at a slice through the cavity mode (Figure 4.6), where  $g$  takes the form,

$$g(\mathbf{r}) = g_0 \cos(2\pi z/\lambda_c) \cdot \exp(-\zeta^2\omega_c^{-2}), \quad (4.18)$$

where  $\zeta = \sqrt{x^2 + y^2}$  is the radial co-ordinate,  $\omega_c$  is the cavity waist, and the cavity mirrors are located at  $z = \pm L/2$ , and  $\Omega$  is a simple Gaussian.

A simplified picture of this variation in the coupling constants can be used to model the expected deviation in the emitted photon shapes. There are two distinct regimes which we should consider. First - the variation in the atom-cavity coupling caused by the standing wave - this is relevant to all Cavity-QED experiments as even with complex trapping geometries (ion traps/dipole traps) the atom localisation will be on the order of 10 – 100

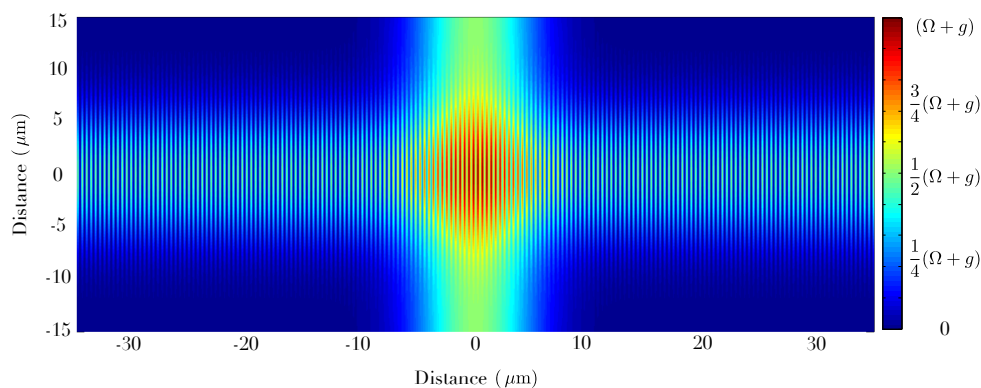
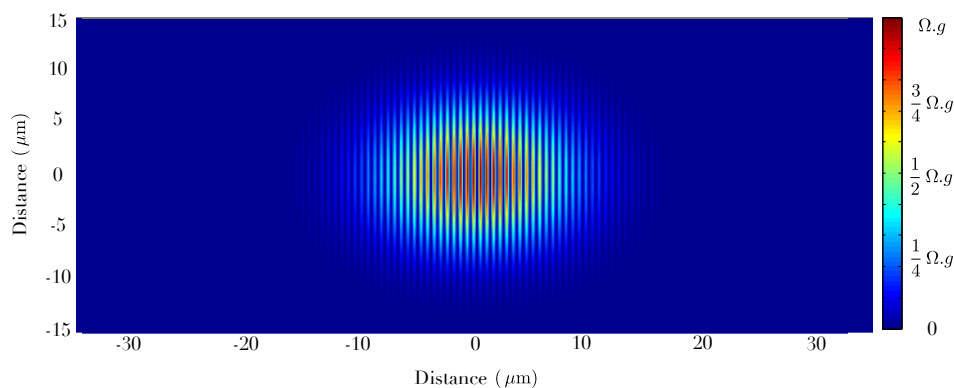
(a) Spatial distribution of  $\Omega + g$ (b) Spatial distribution of  $\Omega \cdot g$ 

Figure 4.6: Variation of interaction strength with position: The magnitude of  $\Omega + g$  is shown (a) for a cross-section of the cavity mode and STIRAP beam. The standing wave of the cavity mode gives rise to the high frequency variation along the cavity axis and the STIRAP beam is visible as the bright stripe propagating along the transverse axis. As the photon generation process is mediated by both  $\Omega$  and  $g$  photons are only produced when the atom is located in a region with a high value of  $\Omega \cdot g$  (b).

nanometres. Secondly there is the variation in the the peak STIRAP Rabi frequency - this variation occurs over a much larger scale and thus is only relevant to our completely un-trapped arrangement.

### 4.3.1 Variation in Atom-Cavity Coupling

We will first consider the regime where the atom is well localised with respect to the STIRAP laser and thus only the atom-cavity coupling deviates from the desired value.

The variation in the maximum photon production efficiency with the value of the atom-cavity coupling is shown in Figure 4.7. It can be seen that there is a high efficiency over a large range of values of  $g$ . Unfortunately the photon shape  $\psi_{ph}(t)$  changes significantly over this range - at  $g = 0.5g_0$  the emission efficiency has only dropped by 20% but the photon is emitted  $0.4\mu\text{s}$  earlier and is only  $2/3$  the width. We would therefore like to calculate a new driving pulse that takes this into account and minimises this variation.

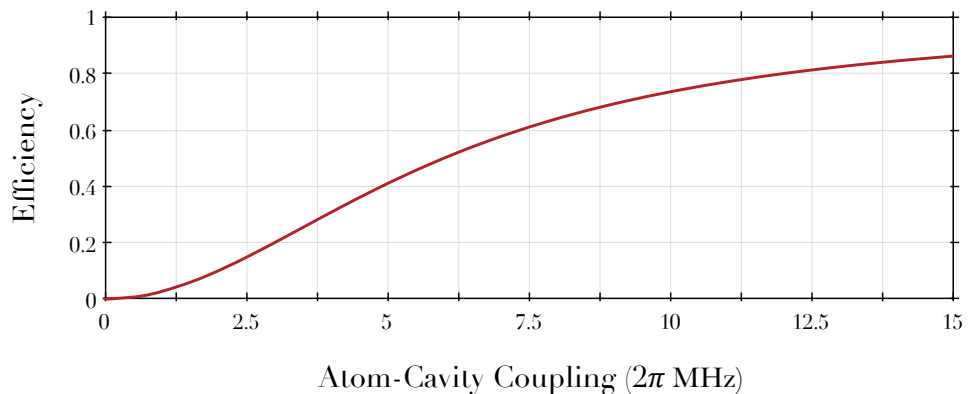
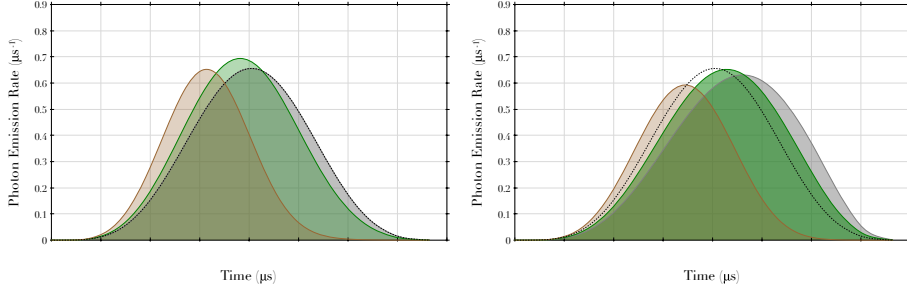
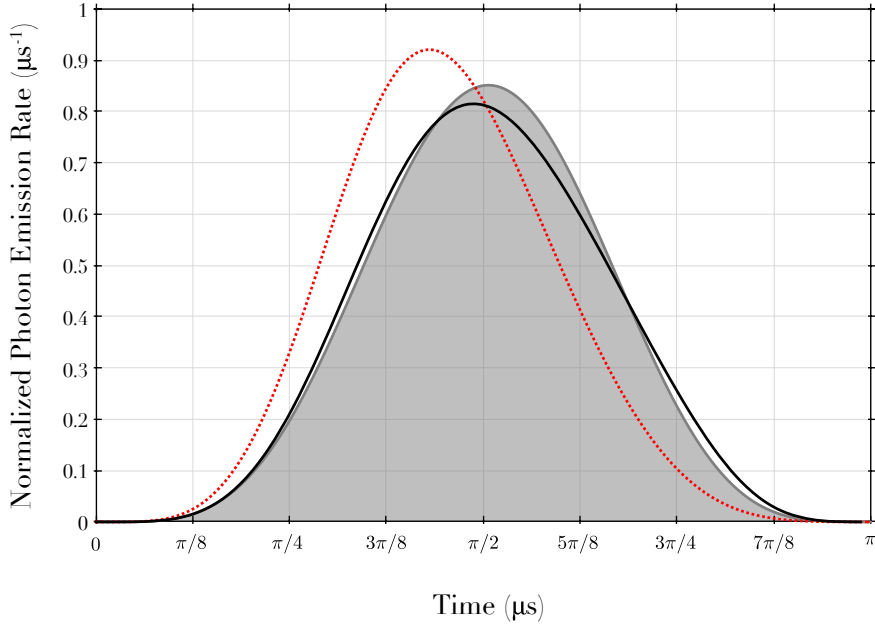


Figure 4.7: Photon production probability: the probability of producing a photon depends on the value of the atom-cavity coupling  $g$ . If we assume long photon lengths ( $T \gg 1/\kappa$ ) the maximum possible production probability is independent of the shape of  $\Omega$  and depends only on the value of  $g$  (red line) ( $\kappa$  and  $\gamma$  are constant). Using the experimentally determined values of the coupling constants, the maximum efficiency is 86%.

The STIRAP Rabi frequency  $\Omega(t)$  required to produce a photon with the shape  $\psi_{ph} = \sin(t)^2$  when  $\{g, \kappa, \gamma\} = 2\pi \cdot \{15, 12, 3\}$  MHz, was calculated using the algorithm from Section 4.1.2. The photon shape for an atom experiencing this Rabi frequency and an atom-cavity coupling increasing from  $g = 0 \rightarrow$

$g = g_0$  in steps of 5% of  $g_0$  was then found via numerical simulation. These photon shapes were weighted by the fractional volume of the cavity mode for each value of  $g$  and summed to get an ensemble average of the photon shape, with the resultant shape shown in Figure 4.8.

(a) Photon shapes when  $\Omega|_{g=g_0}$ (b) Photon shapes when  $\Omega|_{g=0.75g_0}$ 

(c) Photon shapes averaged over all atom-cavity couplings.

Figure 4.8: Normalized ensemble photon shapes: The detected ensemble photon shape will be distorted as the atom will interact with the cavity at all values of  $g$  from  $0 \rightarrow g_0$ . The shape of the photon produced when the atoms experiences  $g = \{0.5, 0.75, 1\}g_0$  (brown, green, grey) are shown in (a) for  $\Omega|_{g=g_0}$  and (b)  $\Omega|_{g=0.75g_0}$ , the desired shape is also shown (black dash). The resultant ensemble shape after the individual photons have been weighted by volume fraction is shown in (c) for  $\Omega|_{g=g_0}$  (red),  $\Omega|_{g=0.75g_0}$  (grey), the ideal is shown in black.

This calculation was initially performed for a STIRAP Rabi frequency  $\Omega(t)$  that was optimized for the peak atom cavity coupling  $g_0$ . The individual photon shapes from poorly coupled atoms are shown in Figure 4.8a. As  $g$  decreases the peak emission rate will occur progressively earlier in time distorting the individual photons away from the desired  $\psi_{ph} = \sin(t)^2$ . This distortion is clearly visible in the ensemble average of the photon shapes (Figure 4.8c, dashed red line).

The driving pulse was then engineered to produce a photon of the desired shape for a value of the atom-cavity coupling of  $g < g_0$ . This has two advantages. Not only is there a greater probability of an atom experiencing this interaction strength as the volume where  $g < g_0$  is greater than the volume where  $g = g_0$ , but also the ensemble distortion caused by the variability in  $g$  is minimised as there is skew to both earlier and later times. These two effects cause the ensemble photon shape to almost regain its desired form. It was found through simulation that a value of  $g \approx 0.75 g_0$  optimised this effect (Figure 4.8).

#### 4.3.2 Variation in STIRAP Rabi Frequency

The second cause of distortion to the emitted photons' shape is due to a variation of the STIRAP Rabi frequency experienced by the atom. As the peak of the individual photon emission rate occurs when  $g_0$  and  $\Omega(t)$  are approximately equal any reduction in the value of  $\Omega(t)$  will result in the photon emission being pushed to later times (this can be seen in Figure 4.9).

As with the variation in  $g$ , it is possible to change the value of  $\Omega(t)$  to minimize the amount of distortion. By increasing the maximum value of  $\Omega(t)$  the ensemble average will be shifted earlier in time and so become more like the desired  $\psi_{ph} = \sin(t)^2$  shape. This is a more complicated task than

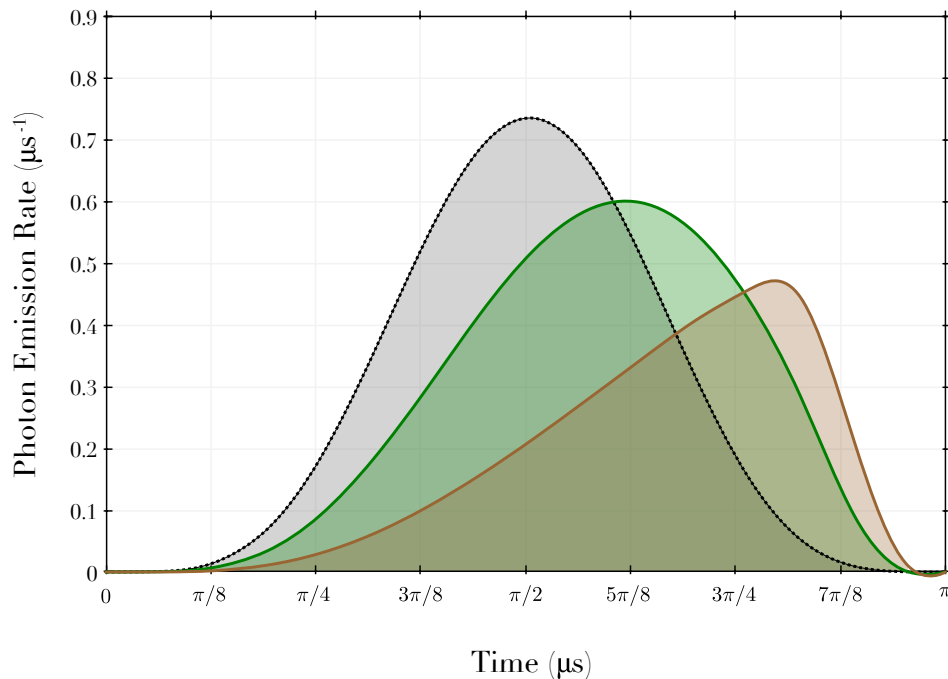


Figure 4.9: Distortion caused by STIRAP Rabi frequency: The emitted photon shape will change depending on the atom's position due to the Gaussian profile of the STIRAP beam. The emitted photon shapes are shown for  $\Omega = (0.5, 0.75, 1)\Omega_{max}$  in brown, green and grey. The ideal shape is also shown (black dash).

the simple scaling performed in Section 4.3.1; not only must we consider variation in  $\Omega(t)$  but also the Gaussian envelope, the standing wave of  $g$ , and the motion of the atoms. One ends up tracing the trajectories of single atoms through a  $\sim 30 \mu\text{m}$  box, calculating the photon shape every 10 nm - a very protracted task. We instead choose to post-select only those photons which came from well-coupled atoms.

#### 4.4 PHOTON SHAPES FROM WELL COUPLED ATOMS

It is not possible to detect the shape of an individual single photon. One must instead detect a large ensemble of photons and as the probability of observing

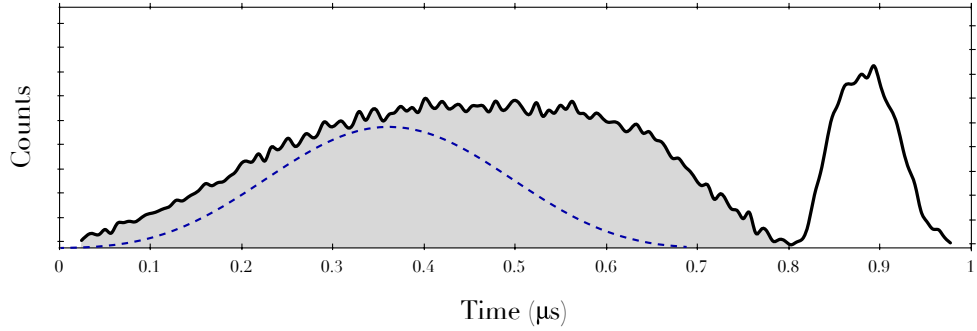


Figure 4.10: Ensemble photon shape: The histogram of detector counts for an ensemble of atoms of unknown position, each driven with the Rabi frequency required to produce a  $\psi(t) \propto \sin^2(t)$  shape is shown in grey. The desired shape of a photon from a well-coupled atom is shown in blue.

a detector click is proportional to the photon shape  $P_{det}(t) \propto |\psi_{ph}(t)|^2$ , one can reconstruct the shape by looking at the times of the detector clicks relative to the start of the driving pulse. If we drive the system with the Rabi frequency calculated using the method in Section 4.1.2 to produce a  $\psi_{ph} = \sin^2(t)$  photon, we would hope to obtain a histogram of detector counts with a  $|\psi_{ph}(t)|^2$  shape. As discussed in Section 4.3 however, the imprecise loading of the atoms into the cavity mode results in a distortion of this ensemble shape. The average shape of the photons produced for all atoms is shown by the grey shaded area in Figure 4.10 along with the photon shape that we expect for a well-coupled atom given the applied driving pulse (dashed blue line). By comparing this shape with Figure 4.9 it is clear that many of the detector clicks used to make this histogram come from atoms located away from the centre of the interaction region.

In Chapter 3 conditioning of the data was discussed in the context of determining the efficiency of photon production from a well coupled atom. It is possible to use the same conditioning method to counteract some of the effects of the random loading of atoms and retrieve only those photons produced from atoms interacting with the desired  $g$  and  $\Omega$ .

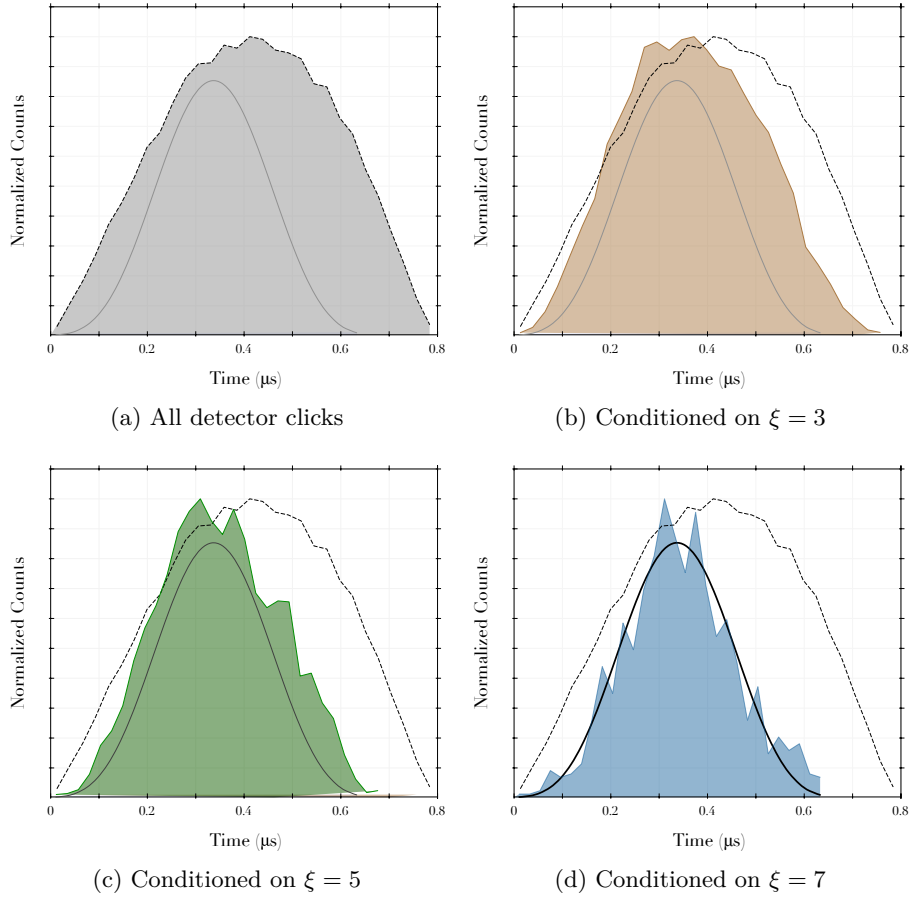


Figure 4.11: Conditioned photon shapes: using careful post-selection is possible to recover only those photons which were emitted by an atom experiencing  $g = g_0$  and  $\Omega = \Omega_{max}$ . The histogram of detector counts without post-selection is shown in (a), with post-selection of  $\xi = 3$  in (b),  $\xi = 5$  in (c) and  $\xi = 7$  in (d). As the post-selection criteria becomes more stringent the distorted photons are removed and the ensemble shape approaches the ideal (solid black).

Figure 3.11 shows a trace of the number of clicks on the detectors per  $100 \mu s$  time bin. As the atom cloud traverses the cavity, in two of these time bins the number of detector clicks is significantly higher than the background; this is understood to be when there is an atom in the cavity. As high photon emission probabilities are only found when the atom is well located with maximum values of  $g$  and  $\Omega$ , selecting only those photons produced around

the peak of the Gaussians fitted to these counts should result in selecting only those photons with the correct shape.

Post-selecting the data using the criteria that there must be more than 1, 3, 5 or 7 clicks per time bin results in ensemble photon shapes shown in Figure 4.11. The ensemble shapes are clearly collapsing towards the expected shape and with the most stringent post-selection criteria - that there must be seven detector clicks per  $100 \mu\text{s}$  time bin (Figure 4.11d) - almost all of the photons which were produced from atoms experiencing a non-maximal Rabi frequency have been removed and there is good overlap between the expected and observed shapes.

## 4.5 A GALLERY OF SINGLE PHOTONS

Whilst a  $\psi = \sin^2(t)$  shape might be very useful [98], it is perhaps also one of the least exciting of possible photon shapes. To show the versatility of both the algorithm and the photon source we have produced a selection of photons with shapes that might be of interest to quantum information applications (Figure 4.12b and Figure 4.12d) [146] and some of a more whimsical nature (Figures 4.13-4.15).

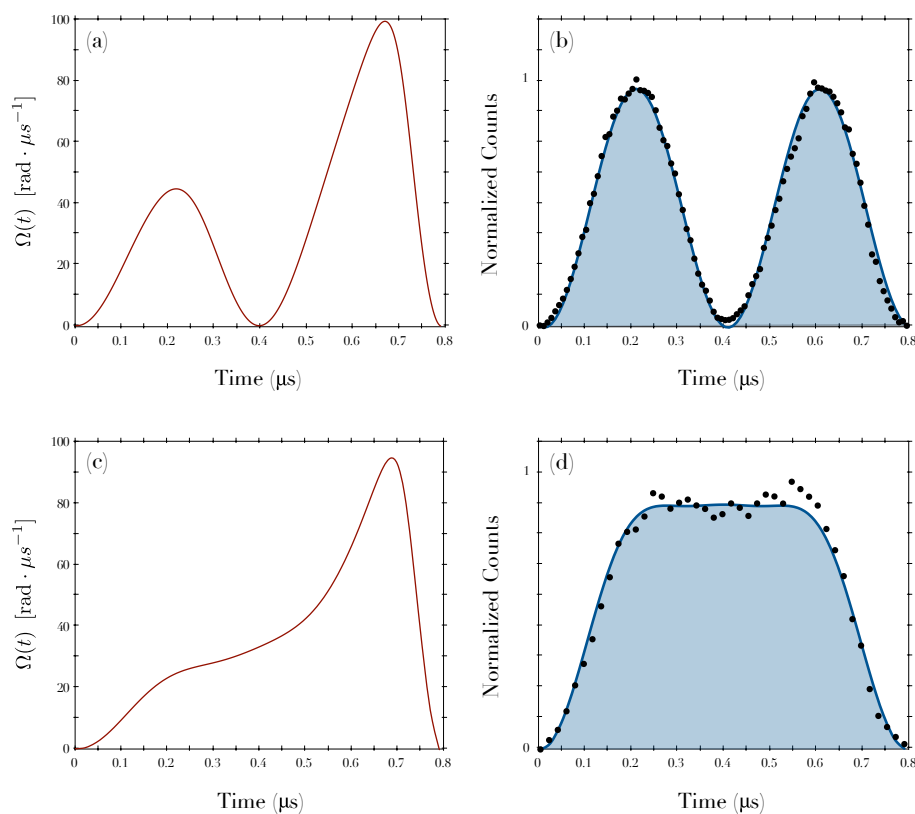


Figure 4.12: Shaped single photons: the STIRAP driving pulse (left) and resultant  $\psi = \sin^2(t)$  and ‘square’ photon shapes (right) are shown.

Although the photon shaping is good it is not perfect and the more complex shapes especially suffer from a ‘smoothing out’ where the sharp features are missing. For example the twin peak photon (Figure 4.12b) which has the

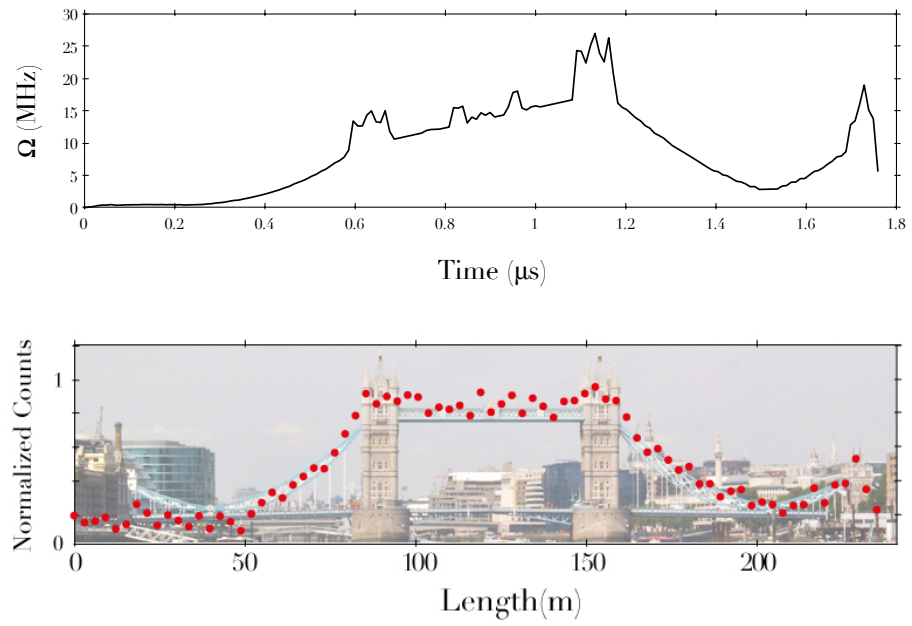


Figure 4.13: Tower Bridge: The upper plot shows the STIRAP pulse applied to obtain the photon shown below. The photon's shape has been drawn assuming that it propagates in a fibre with refractive index  $n = 2$  and is thus to scale.

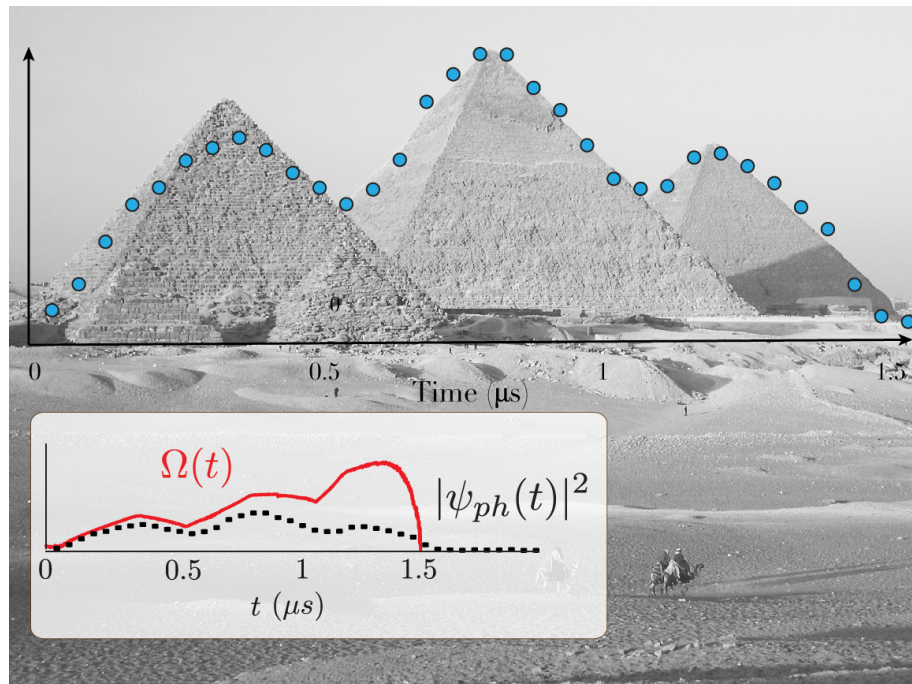


Figure 4.14: The Pyramids of Giza

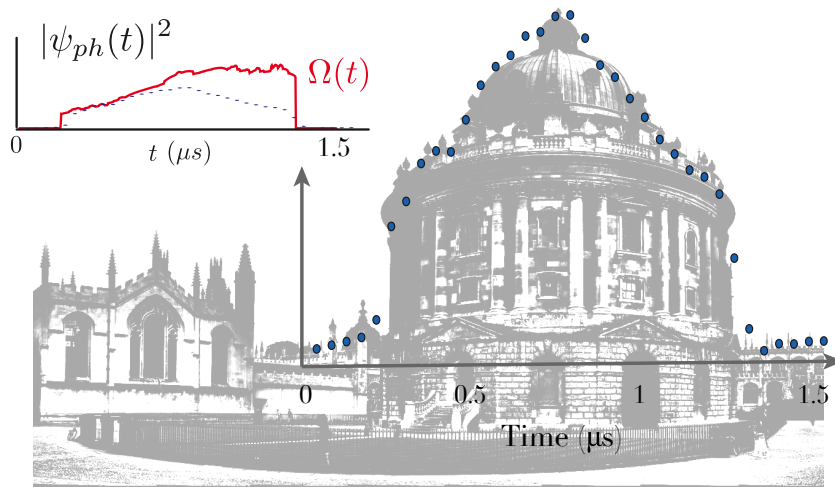


Figure 4.15: The Radcliffe Camera - part of the Bodleian Library in Oxford

fewest high frequency components is almost perfectly realised whereas the more complex shapes, which require a higher bandwidth modulation (e.g. the turrets on Tower Bridge), are missing.

It is believed that these imperfections are primarily due to the limited bandwidth of the AOM used to shape the driving pulse (Figure 4.16); this could only modulate the STIRAP pulse at a maximum of 3 MHz and therefore could not accurately produce the complex pulse shapes that were required. It is though that by using a modulator with a higher bandwidth, such as an EOM, it will be possible to obtain the missing sharp features. This will eventually be limited by the system due to the rates  $g$  and  $\kappa$ .

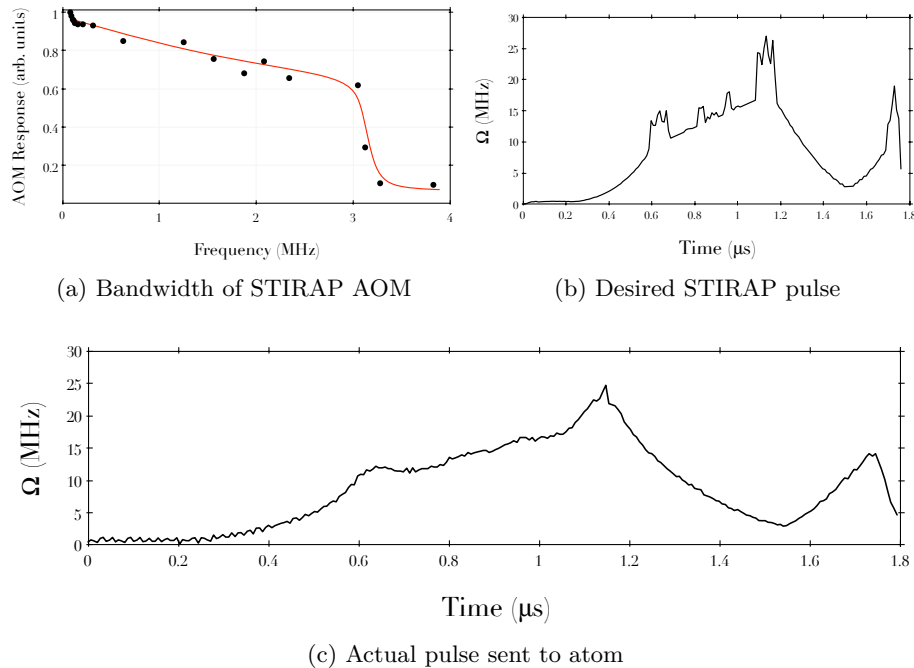


Figure 4.16: STIRAP pulse shaping: The limited bandwidth of the STIRAP AOM (a) means that the high frequency components of the STIRAP pulse required to produce a photon shaped like Tower Bridge (b) are not present in the pulse which is actually sent to the atom (c).

#### 4.6 CONCLUSION

A priori control over the temporal shape of single photons has been demonstrated based on the analytical algorithm presented in [138]. As this algorithm relies on an idealised three-level system it was necessary to perform full numerical simulations of the  $^{87}\text{Rb}-D_2$  transition to verify that that it was applicable to this system. The additional complexity of the full  $D_2$  manifold did cause a distortion in the simulated photon shape, however this was below the expected accuracy of the experimental realisation. The STIRAP pulse shapes produced by the three-level algorithm were therefore used without further modification.

The distortion caused to the ensemble photon shape by the variability in the atoms' positions in the cavity was also considered. This fell into two

distinct regimes. The first, a distortion caused by the variation in  $g$  due to the vacuum-mode standing wave, was an effect which occurred when the uncertainty in the atoms' position was on the order of 100 nm, this will therefore require consideration from all atom-cavity sources. The second, a distortion caused by variation in the STIRAP Rabi frequency, was due to the imprecise position of the atoms with respect to the  $\omega_0 = 14 \mu\text{m}$  STIRAP beam, this distortion applies to experiments where the atoms are not trapped. A method of post-selection which allows for the identification of only those photons which were produced by correctly positioned atoms was also presented.

The techniques discussed in this chapter were used to produce photons with a variety of unusual shapes, this demonstrates the level of control which a C-QED experiment provides over the interaction between an atom and a photon.



## CONTROLLING THE FREQUENCY AND PHASE

---

Having shown control over the amplitude of the single photons that we produce; we would now like to explore which other properties of the photons we can change. The two most accessible properties of the photons are their frequency and phase as these depend solely on the control which we can already exert over the STIRAP pulse Rabi frequency  $\Omega(t)$ .

As in Chapter 3 the photons' properties will be characterised using Hong-Ou-Mandel interferometry as this has been shown to be strongly dependent on the properties of the photons under consideration [147–150]. To understand what we expect to observe we must extend the theory to include the time-dependence of the photons: this will be shown in Section 5.1. Control over the photons' frequency is shown in Section 5.3. The ability to apply an arbitrary relative phase between the individual peaks of a twin-peak photon is demonstrated in Section 5.4. In Section 5.5 it is discussed how this can be used as a method of preparing arbitrary qubits for LOQC; and types of circuits that these qubits can be used in are shown in Section 5.6.

### 5.1 TIME-RESOLVED HONG-OU-MANDEL INTERFERENCE

In the initial explanation of Hong-Ou-Mandel interference (Section 3.6.1) the creation operators  $\hat{a}_A^\dagger$  and  $\hat{a}_B^\dagger$  were defined to create a photon in the spatio-temporal mode defined by the photon's envelope  $\xi(t)$  (Figure 5.1). With this simplification we were able to obtain an initial expectation of the

results that would be observed. A similar simplification can be performed with the twin-peak photons that will be used in this chapter, where we define two distinct modes - one for each peak of the photon - using the substitution,

$$\hat{a}_A^\dagger = \frac{1}{\sqrt{2}}(\hat{a}_{A1}^\dagger + \hat{a}_{A2}^\dagger), \quad (5.1)$$

where  $\hat{a}_{A1}^\dagger$  and  $\hat{a}_{A2}^\dagger$  are the creation operators for a photon in the first and second time-bins respectively. The photon is now split into two independent time-bins, 1 and 2, each subject to the standard beam-splitter relations; a similar expression holds for the creation operators in mode B (this can be seen in Figure 5.1). Performing this substitution on the initial input state incident upon the beam-splitter results in,

$$\hat{a}_A^\dagger \hat{a}_B^\dagger |Vac\rangle = \frac{1}{2}(\hat{a}_{A1}^\dagger + \hat{a}_{A2}^\dagger)(\hat{a}_{B1}^\dagger + \hat{a}_{B2}^\dagger) |Vac\rangle. \quad (5.2)$$

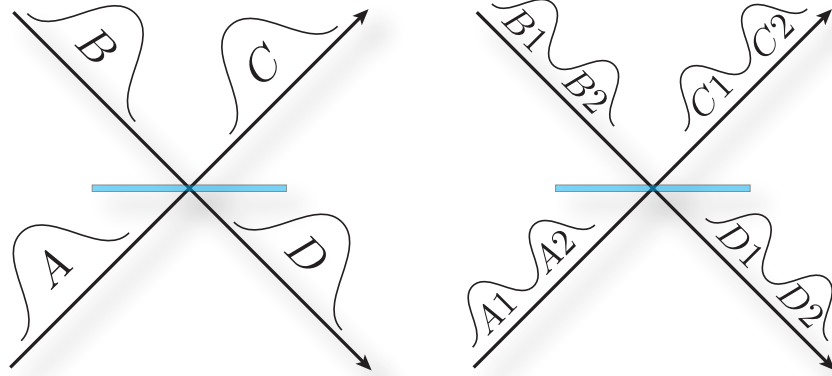


Figure 5.1: Time-binned HOM: the theory of Hong-Ou-Mandel interference can be extended to include a single photon which exists in multiple time-bins.

The beam-splitter then acts on the individual time-bins, splitting each input mode into an equal superposition of the two output modes. One only

has to note that photons in modes  $\{A1, B1\}$  are mapped to modes  $\{C1, D1\}$  and  $\{A2, B2\} \rightarrow \{C2, D2\}$ .

$$\begin{aligned}\hat{a}_{A1}^\dagger &= \frac{1}{\sqrt{2}}(\hat{a}_{C1}^\dagger + \hat{a}_{D1}^\dagger), & \hat{a}_{A2}^\dagger &= \frac{1}{\sqrt{2}}(\hat{a}_{C2}^\dagger + \hat{a}_{D2}^\dagger), \\ \hat{a}_{B1}^\dagger &= \frac{1}{\sqrt{2}}(\hat{a}_{C1}^\dagger - \hat{a}_{D1}^\dagger), & \hat{a}_{B2}^\dagger &= \frac{1}{\sqrt{2}}(\hat{a}_{C2}^\dagger - \hat{a}_{D2}^\dagger).\end{aligned}\quad (5.3)$$

Substituting these relations into Equation 5.2 gives the output state,

$$\frac{1}{2}\left(\frac{1}{\sqrt{2}}(\hat{a}_{C1}^\dagger + \hat{a}_{D1}^\dagger) + \frac{1}{\sqrt{2}}(\hat{a}_{C2}^\dagger + \hat{a}_{D2}^\dagger)\right)\left(\frac{1}{\sqrt{2}}(\hat{a}_{C1}^\dagger - \hat{a}_{D1}^\dagger) + \frac{1}{\sqrt{2}}(\hat{a}_{C2}^\dagger - \hat{a}_{D2}^\dagger)\right), \quad (5.4)$$

which, ignoring global factors can be simplified to,

$$\left(\hat{a}_{C1}^\dagger \hat{a}_{C1}^\dagger + \hat{a}_{C2}^\dagger \hat{a}_{C2}^\dagger - \hat{a}_{D1}^\dagger \hat{a}_{D1}^\dagger - \hat{a}_{D2}^\dagger \hat{a}_{D2}^\dagger\right) + 2\hat{a}_{C1}^\dagger \hat{a}_{C2}^\dagger - 2\hat{a}_{D1}^\dagger \hat{a}_{D2}^\dagger. \quad (5.5)$$

The physics involved in this expression is contained in the subscripts  $\{C_i D_i\}$ . It can be seen that the photons always coalesce and leave the beam-splitter through the same output port, i.e. we only ever see pairs of creation operators with the same subscripts  $\hat{a}_{C_i}^\dagger \hat{a}_{C_i}^\dagger$  or  $\hat{a}_{D_i}^\dagger \hat{a}_{D_i}^\dagger$ .

### 5.1.1 Full Time-Resolution

The theory presented thus far has assumed that the creation operator acts on the mode defined by the photon's probability amplitude. Whilst this is extremely useful in many cases (and will be essential in later sections) it does not describe the full time-resolution observed in this experiment. As the photons are very long compared with the detector time resolution we would like to increase the resolution of our theory to match this. If the photon length is only slightly greater than the detector resolution  $t_{ph} > T_{det}$  this could be done by artificially subdividing the continuous photon into collection

of time-bins, each with a width  $T_{det}$  and then applying the method described in Section 5.1 for the discontinuous multi-peaked photons. For the photons produced in this experiment however, this would require  $10^5$  time-bins and so we instead move to the completely general case found in the limit  $T_{det} \rightarrow 0$ . The following discussion is a précis of the theory developed in [113, 115] and has been included to aid in the comprehension of the presented results; the reader should refer to the above references for the complete theory of time-resolved HOM.

The photon is treated as a continuous function which can be written as the product of a real amplitude,  $\epsilon(t)$ , and a complex phase,  $\phi(t)$ ,

$$\xi(t) = \epsilon(t) \exp(-i \phi(t)), \quad (5.6)$$

where the photon amplitude is normalised such that  $\int |\epsilon(t)|^2 dt = 1$ . The correlation function for the interference between two such photons of identical polarization (e.g. both photons are horizontally polarized) takes the form,

$$G_{HH}^{(2)}(t_1, t_2) = \frac{|\xi_1(t_1)\xi_2(t_2) - \xi_1(t_2)\xi_2(t_1)|^2}{4}, \quad (5.7)$$

i.e. we have an interference between photon 1 at time  $t_1$  and photon 2 at time  $t_2$  and between photon 1 at  $t_2$  and photon 2 at  $t_1$ . If we multiply this expression out we can write the result as a sum of two terms,

$$G_{HH}^{(2)}(t_1, t_2) = G_{HV}^{(2)}(t_1, t_2) - F(t_1, t_2), \quad (5.8)$$

The first term  $G_{HV}^{(2)}(t_1, t_2)$  is simply the convolution of the real photon amplitudes; it is the function that one would observe if the photons had orthogonal polarizations and did not interfere. The second term  $F(t_1, t_2)$

describes the interference between the photons which is governed by the relative phases of two photons.  $G_{HV}(t_1, t_2)$  and  $F(t_1, t_2)$  are given by,

$$G_{HV}^{(2)}(t_1, t_2) = \frac{|\epsilon_1(t_1)\epsilon_2(t_2)|^2 + |\epsilon_1(t_2)\epsilon_2(t_1)|^2}{4}, \quad (5.9)$$

$$F(t_1, t_2) = \frac{\epsilon_1(t_1)\epsilon_2(t_2)\epsilon_1(t_2)\epsilon_2(t_1)}{2} \times \cos(\phi_1(t_1) - \phi_1(t_2) + \phi_2(t_2) - \phi_2(t_1)). \quad (5.10)$$

When a HOM experiment is actually performed what we measure is the difference in time between the detections of the two photons  $\tau = t_2 - t_1$ . This function - the probability of detecting a correlation at a particular time delay,  $\tau$  - can be found by integrating the above correlation function over the time of the first detection  $t_1$ ,

$$P^{(2)}(\tau) \propto \int dt_1 G^{(2)}(t_1, t_1 + \tau). \quad (5.11)$$

### 5.1.2 Decoherence

Until now we have assumed that the photon source is perfect and that all of the photons can be described by the same wavefunction  $\xi(t) = \epsilon(t) \exp(-i\phi(t))$ . In a more realistic scenario the properties of the emitted photon will have some form of jitter caused, for example, by the STIRAP laser's finite bandwidth or stray magnetic fields shifting the atom's energy levels. These variations will result in the properties of the successively emitted photons being different from one another and will thus change the expected pattern of correlations.

A jitter in the frequency of the photons will only manifest itself in the phase  $\phi(t)$  part of the photon  $\xi(t)$ , and thus will only affect the interference

term  $F(t_1, t_2)$ . If we assume a Gaussian frequency jitter between the photon pairs,

$$f(\Delta) = \frac{1}{\sqrt{\pi}\delta\omega} \exp(-\Delta^2/\delta\omega^2), \quad (5.12)$$

where  $\Delta$  is the frequency difference between the photons, and  $\delta\omega$  is the width of the frequency distribution, and integrate this over all frequency differences, we obtain a correlation probability function of the form,

$$P^{(2)}(\tau) \propto \int dt_1 G_{HV}^{(2)}(t_1, t_1 + \tau) - \exp\left(\frac{-\tau^2}{4/\delta\omega^2}\right) \int dt_1 F(t_1, t_1 + \tau). \quad (5.13)$$

Examples of the correlation probability function  $P^{(2)}(\tau)$  for two different photon amplitudes,  $\epsilon(t)$ , are shown in Figure 5.2. The most surprising feature of these figures is that the correlation function *always* drops to zero at  $\tau = 0$ , irrespective of the magnitude of the decohering frequency jitter. This

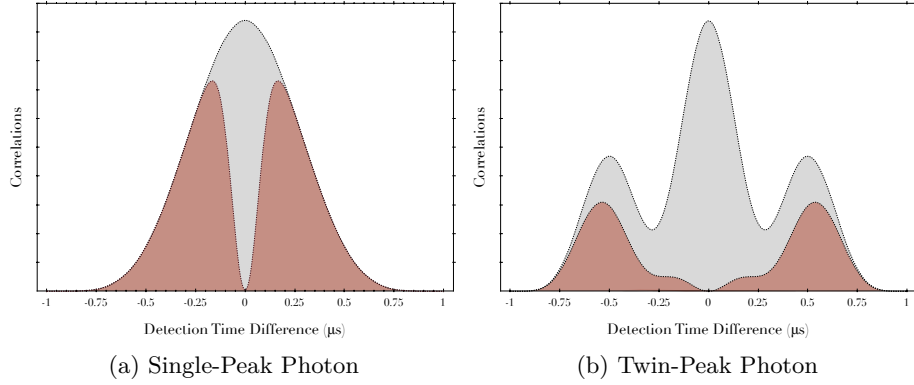


Figure 5.2: Time-Resolved HOM: the correlation probability functions for single-, and twin-peak  $\epsilon(t) = \sin^2(t)$  photons, are shown for perpendicularly (grey) and parallel (red) polarizations. With infinite coherence no correlations will be observed, with a finite coherence time correlations will appear, even for perfectly parallel photons. The single-peak and twin-peak photons shown here have coherence times of  $T_2 = 0.1 \mu\text{s}$  and  $T_2 = 0.5 \mu\text{s}$  respectively.

is because the relative phase of the photons is not defined until the first photon has been measured. If there is a second detection at  $\tau = 0$  the photons will be in phase, no matter how different they are, and so there are no correlations. Once the first detection has occurred however, and has projected the separable input state into an entangled combination of  $\xi_1$  and  $\xi_2$  with a defined phase relation, it is subject to classical interference fringes evolving according to the photons' phases  $\phi_1$  and  $\phi_2$ . As the time difference between the detections increases so does the relative phase difference, and as this phase accumulation is incoherent washes out any coherent phase relation between the photons and so defines their mutual coherence time  $T_2$ .

It is also possible to have a jitter in the emission-time of the photons; this would have the effect of significantly broadening the apparent envelope of the photon  $|\epsilon(t)|^2$ . Considering the results shown in Section 4.5 this effect has been deemed negligible for the demonstrated source.

## 5.2 A TWIN-PEAK PHOTON

The photons that we shall be using for the majority of this chapter are the twin-peak  $\psi = \sin^2(t)$  photons that were originally produced in Figure 4.12b. The autocorrelation function has a triple peak structure and is clearly resolved using non-interfering perpendicularly polarized photons - it has a large central peak caused by detector clicks in  $\hat{a}_{C1}^\dagger \hat{a}_{D1}^\dagger$  and  $\hat{a}_{C2}^\dagger \hat{a}_{D2}^\dagger$  and two side peaks of half the height caused by the correlations between  $\hat{a}_{C1}^\dagger \hat{a}_{D2}^\dagger$  and  $\hat{a}_{C2}^\dagger \hat{a}_{D1}^\dagger$  (Figure 5.3). If we rotate the polarization of the photons to be identical the photons will interfere, ideally resulting in no correlations. We almost reach this ideal case with an interference visibility of  $V_{ph} = 0.80 \pm 0.05$ , caused by a coherence time of  $T_2 = 0.5 \mu s$ .

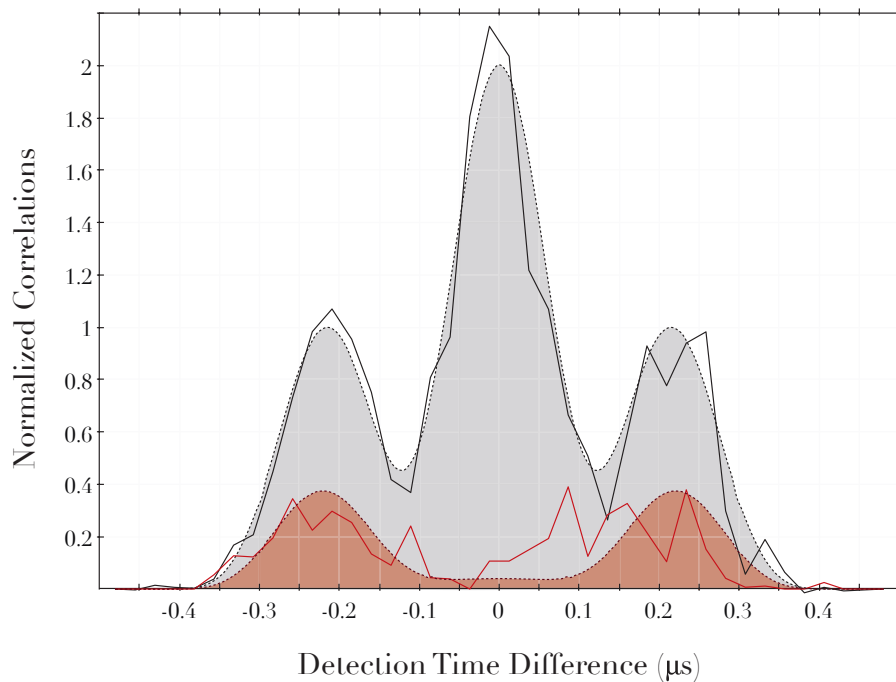


Figure 5.3: HOM of a twin-peak photon: the cross-correlation function photons is shown as a function of the detector time difference,  $\tau$ , for  $\phi = \sin^2(t)$  twin-peak photons with parallel (red) and perpendicular (grey) polarizations.

### 5.3 CHANGING A PHOTON'S FREQUENCY

The photons are produced via a Raman transition, so their frequency is determined by the difference in energy between the initial and final states and the energy of the STIRAP laser which drives the transition,

$$\hbar\omega_{ph} = \hbar\omega_{STIRAP} + E_{initial} - E_{final}. \quad (5.14)$$

Perhaps surprisingly the frequency of the cavity does not affect the frequency of the emitted photon, only the probability of emission. Given that the atomic energy levels are fixed, if we change the frequency of the STIRAP laser we should be able to change the frequency of the resulting photons. We cannot, however, emit a photon at an arbitrary frequency. The probability of

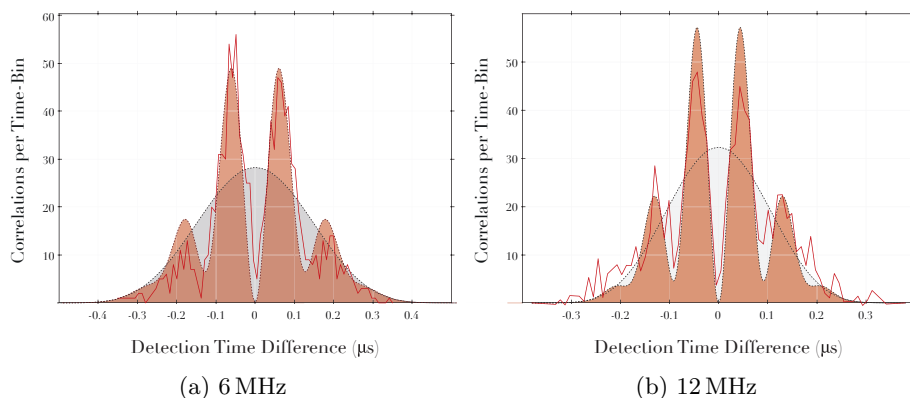


Figure 5.4: Changing a photon's frequency: a beat note between two parallel polarized photons of different frequencies was observed in the HOM (red). The data is shown as a histogram with 8 ns time-bins. A theoretical curve was fitted to the data (red shading); the perpendicular polarized reference is also shown (grey).

emitting a photon into the cavity mode at a particular frequency depends on the cavity resonance and line-width; if  $\omega_{ph} = \omega_{Cav}$  the emission probability is maximized, but if  $\omega_{ph}$  is very far detuned from  $\omega_{Cav}$  emission is unlikely. Whilst it is relatively easy to drive the atom at an arbitrary frequency - either tuning  $\omega_{STIRAP}$  with an AOM or even using another laser altogether - changing the cavity resonance is not. Even if one were to use a cavity that was actively locked during the interaction time, moving the macroscopic cavity mirrors a sufficient distance to create a frequency shift of more than a few MHz/ms is impractical. Despite this, we still have the ability to change the frequency of the photons within the cavity linewidth.

### 5.3.1 Changing a Whole Photon's Frequency

Initial experiments were performed with the single-peak photons produced in Section 3.6.3. The frequency shift was measured by observing a beat in the HOM interference; this can be thought of as a type of heterodyne

measurement, but instead of using two coherent beams we are using two single photons.

A stream of photons was produced in which the frequency of the photons alternated by  $\Delta$ , which ensures that every correlation is the result of the interference of a pair of photons with a frequency difference. The interference patterns for photons where the STIRAP laser was shifted in frequency by 6 MHz and 12 MHz are shown in Figure 5.4. Theoretical fits to the observed correlation resulted in frequency shifts on the photons of  $\Delta = 6.2 \pm 0.3$  MHz and  $\Delta = 11.9 \pm 0.3$  MHz. The coherence time of the photons was unaffected. This shows good agreement with past experiments [114].

### 5.3.2 *Changing Half a Photon's Frequency*

We would also like to show that it is possible to change the frequency within a single photon. To do this we use a twin-peaked photon (Figure 5.3) and change the frequency of one of the peaks with respect to the other. The frequency of the driving laser is shifted below the cavity resonance,  $\Delta = -6$  MHz, during the first half of the photon and then above resonance,  $\Delta = +6$  MHz, during the second half to ensure that the photon production efficiency is not too significantly harmed by the frequency shift.

As before, the frequency shift was tested by interfering this photon with another photon which had a constant frequency,  $\Delta = 0$ . The result of the measurement is shown in Figure 5.5, and from a theoretical fit to the data we obtain a measured frequency difference of  $\Delta = 11 \pm 1.5$  MHz. The interference pattern shows a beat for correlations within the same time-bin however the discontinuous frequency step washes out the interference between the different time-bins. The spectral properties of this photon are quite peculiar. Usually when one considers the spectrum of a single photon, one imagines a particle

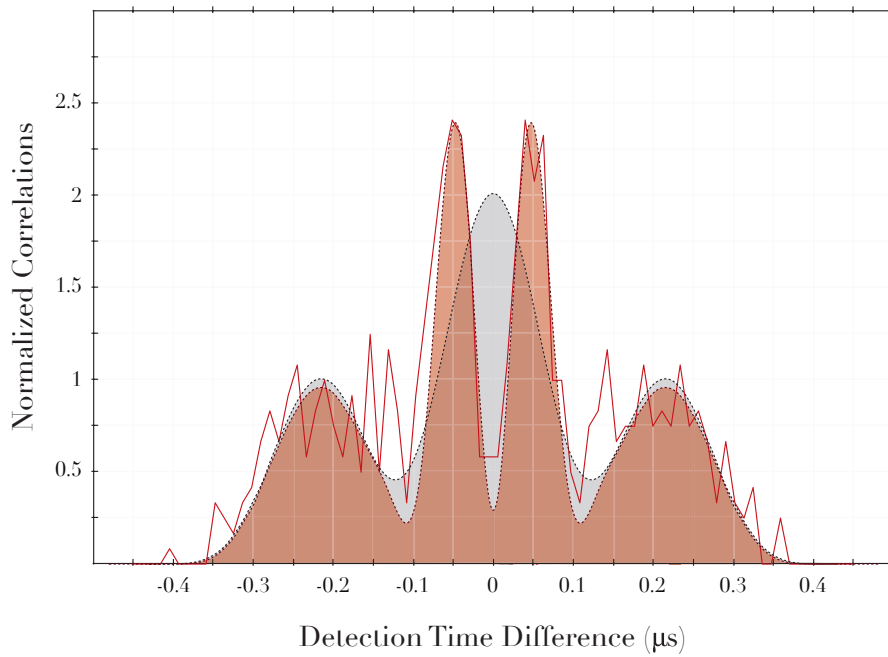


Figure 5.5: Changing the frequency within a single photon: a beat note between two parallel polarized photons - one with frequency  $\Delta = 0$  and the other with a frequency shift  $\Delta = -6$  MHz during the first time-bin and  $\Delta = +6$  MHz during the second time-bin - was observed in the HOM signal (red). A theoretical fit is shown (red shading) along with the perpendicular polarized reference (grey).

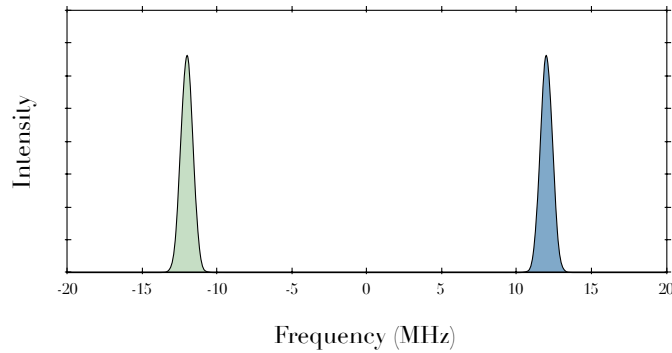


Figure 5.6: Spectrum of a frequency shifted photon: a photon with a frequency shift between its two time-bins will have the spectrum shown in green during during the interval  $0 < t < T_{ph}/2$  and the spectrum shown in blue during the interval  $T_{ph}/2 < t < T_{ph}$ , where  $T_{ph}$  is the length of the photon.

defined by a single frequency with a Fourier limited bandwidth. This is not the case here, this single photon exhibits two distinct frequencies at different times, these are separated by 12 MHz and each has a bandwidth of 500 kHz (Figure 5.6).

#### 5.4 CHANGING A PHOTON'S PHASE

In this section the ability to change the phase of a single photon is demonstrated. A photon does not have defined phase until it is measured and so we cannot put an arbitrary phase on the whole photon - instead we must impose a phase *relation* between the two peaks of a single photon.

##### 5.4.1 Phase-Shifted Hong-Ou-Mandel Interference

Consider an extension of the theory presented in Section 5.1 where we now impose a phase-flip  $\phi$  on the second time-bins of photon  $\hat{a}_B^\dagger$ ,

$$\hat{a}_B^\dagger = \frac{1}{\sqrt{2}}(\hat{a}_{B1}^\dagger + \hat{a}_{B2}^\dagger) \rightarrow \frac{1}{\sqrt{2}}(\hat{a}_{B1}^\dagger + e^{i\phi} \hat{a}_{B2}^\dagger). \quad (5.15)$$

For ease of understanding we shall use the case where we set the value of this phase shift to  $\phi = \pi$ , giving an input state of,

$$\hat{a}_A^\dagger \hat{a}_B^\dagger |Vac\rangle = \frac{1}{2}(\hat{a}_{A1}^\dagger + \hat{a}_{A2}^\dagger)(\hat{a}_{B1}^\dagger - \hat{a}_{B2}^\dagger) |Vac\rangle. \quad (5.16)$$

This change of sign in the superposition on the time-bins of photon B causes a dramatic change in the final expression for the output state which now reads

$$\left( \hat{a}_{C1}^\dagger \hat{a}_{C1}^\dagger - \hat{a}_{C2}^\dagger \hat{a}_{C2}^\dagger - \hat{a}_{D1}^\dagger \hat{a}_{D1}^\dagger + \hat{a}_{D2}^\dagger \hat{a}_{D2}^\dagger \right) + 2\hat{a}_{C1}^\dagger \hat{a}_{D2}^\dagger - 2\hat{a}_{D1}^\dagger \hat{a}_{C2}^\dagger. \quad (5.17)$$

As with Equation 5.5 the first term contains all the creation operator pairs where both photons are detected in the same time-bin; here the photons have coalesced and are always found in the same output port. The interesting part of this expression is the situation where the two photons are detected in different time-bins (i.e. one photon in bin-1 and the other in bin-2); these are shown in the final two terms in the equation. With this  $\phi = \pi$  phase shift the photons no longer coalesce, instead they are actively forced into opposite output ports; if the first photon is detected in  $C1$  the the second *must* be detected in  $D2$  (and vice versa).

The photon correlations, which normally follow bosonic statistics, have been projected into a quasi-fermionic state by the first detection and thus the photons will never coalesce at the same detector across time-bins.

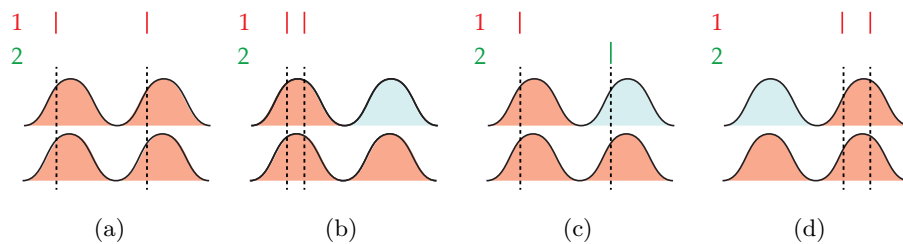


Figure 5.7: Graphical representation of the HOM interference of two twin-peak photons: the two photons are represented by the upper and lower envelopes. The detection of a photon is shown by a vertical line next to the either detector 1 (red) or detector 2 (green). The relative phase of the two photons at the first detection is shown by the red shading and a  $\pi$ -phase shift is represented by blue shading.

This can be considered pictorially in Figure 5.7. If the photons have no phase-flip between the two peaks (a) then after the first detection - a click in detector 1 which defines the phases of the two photons to be zero - the photons are identical and so will bunch, resulting in no detector correlations (Figure 5.7a). If there is a  $\phi = \pi$  phase-flip however, a detection in the first half of the photon will define the relative photon phases such that they are orthogonal in the second half (Figure 5.7c) and a subsequent detection must

only occur in detector 2 - i.e. the correlations shown in the previous section. Although they appear trivial, as they do not cause any correlations, the bunching of photons with a phase-flip is actually quite interesting. If both detections occur in the first half of the photon (Figure 5.7b) this bunching makes sense - both photons have been annihilated before their phase-flipped parts interacted. However, if both detections occur in the second half of the photon (Figure 5.7d), the phase relation between them is not set until after the phase-flip, reinforcing the fact that photons have no absolute phase.

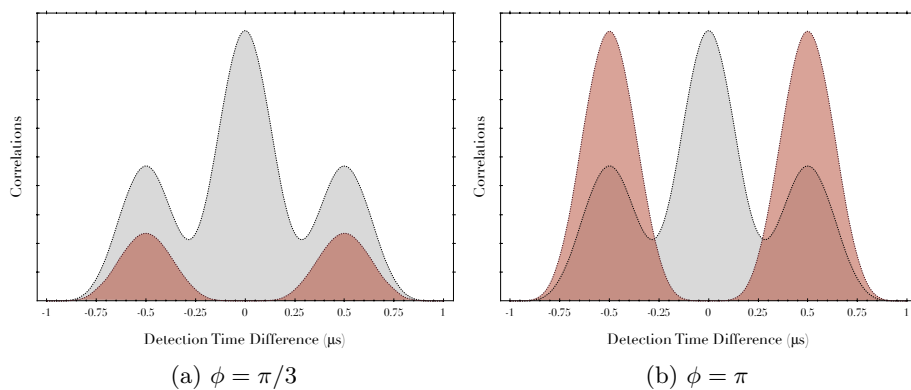


Figure 5.8: Time-resolved HOM of a twin-peak photon with a phase shift: by imposing a relative phase shift of  $\phi$  between the first and second peaks of the photon the photons are forced out of separate ports of the beam-splitter and hence cause correlations (red). The number of correlations is dependent on the phase with a minimum at  $\phi = 0$  and a maximum at  $\phi = \pi$ . The perpendicular polarized reference is also shown (grey).

Whilst this type of discussion can be useful to gain a conceptual understanding of what one expects to observe in this experiment it must be used with care. It is easy to slip into a train of thought in which two single photons arrive at a beam-splitter and through some local interaction decide which way to go; unfortunately this is not what happens. The important feature of two-photon interference is that the photon amplitudes are indistinguishable at the detectors, if this condition is met interference will occur even if the photons never overlapped at the beam-splitter [151].

### 5.4.2 *Creating the Phase Shift*

We would now like to try to produce photons with the type of phase-flip that we have been discussing. As the only time-dependent variables in the photon production process are the Rabi frequency of the STIRAP laser  $\Omega(t)$  and the photon itself  $\psi_{ph}(t)$ , to create a phase-flip in our photons all we must do is flip the phase of the STIRAP laser. This can be changed by applying a phase shift to the RF input of the AOM used to generate the pulse.

By beating the STIRAP pulse against a 10 MHz detuned, phase stable Local Oscillator (L.O.) in a heterodyne type measurement, we can verify this phase shift. The resulting beat signal is shown in Figure 5.9. One thing to note is that the phase shift is applied each time the beam passes through the AOM, i.e. for a double passed AOM a phase shift of  $\pi/2$  on the RF input is required to achieve an overall shift of  $\pi$ .

### 5.4.3 *Photons with a phase-flip*

The cross correlations measured for phase shifts between 0 and  $4\pi/3$  are shown in Figure 5.10. It can be clearly seen that the observed data behave as predicted by the theory; starting from a minimum at  $\phi = 0$  the correlations rise to a maximum with a  $\pi$  phase-shift, and then decrease once again. This is expressed more succinctly in Figure 5.11 which shows the total number of correlations observed in the side peaks normalized to the number of correlations observed with perpendicularly polarized photons. The expected change in peak visibility with phase shift (assuming  $T_2 = 500 \mu s$ ) is shown (red), and a theoretical fit to the data is shown in grey. Although these differ, the null hypothesis that the data are well represented by the expected peak

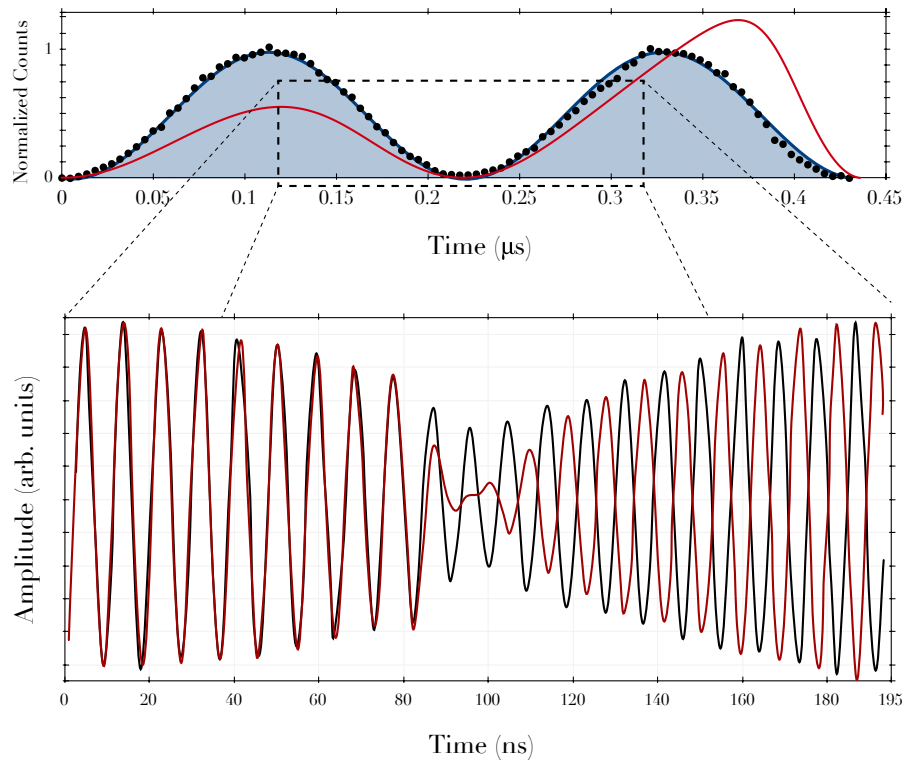


Figure 5.9: Measuring the phase of the STIRAP pulse: the phase of the STIRAP pulse used to produce a twin-peak photon (top) can be measured by beating it against a stable reference. The heterodyne-type signal (bottom) for the case where no phase shift has been applied (black), and the case when a phase shift of  $\phi = \pi$  has been applied to the driving pulse (red). In the first part of the pulse the two heterodyne signals are perfectly in phase, and in the second half of the pulse the phase shift of  $\pi$  is clearly visible. The amplitude of the  $\phi = 0$  pulse should be zero at the centre of the plot however this has been artificially increased to make the phase shift more obvious.

visibility is well within the 95% confidence bounds ( $\chi^2$ -test) and so can be accepted.

## 5.5 ARBITRARY QUBIT PREPARATION

In the preceding sections we have shown that we have complete control over the amplitude, frequency and phase of the single photons that we produce; and we would now like to put that control to use. A standard technique

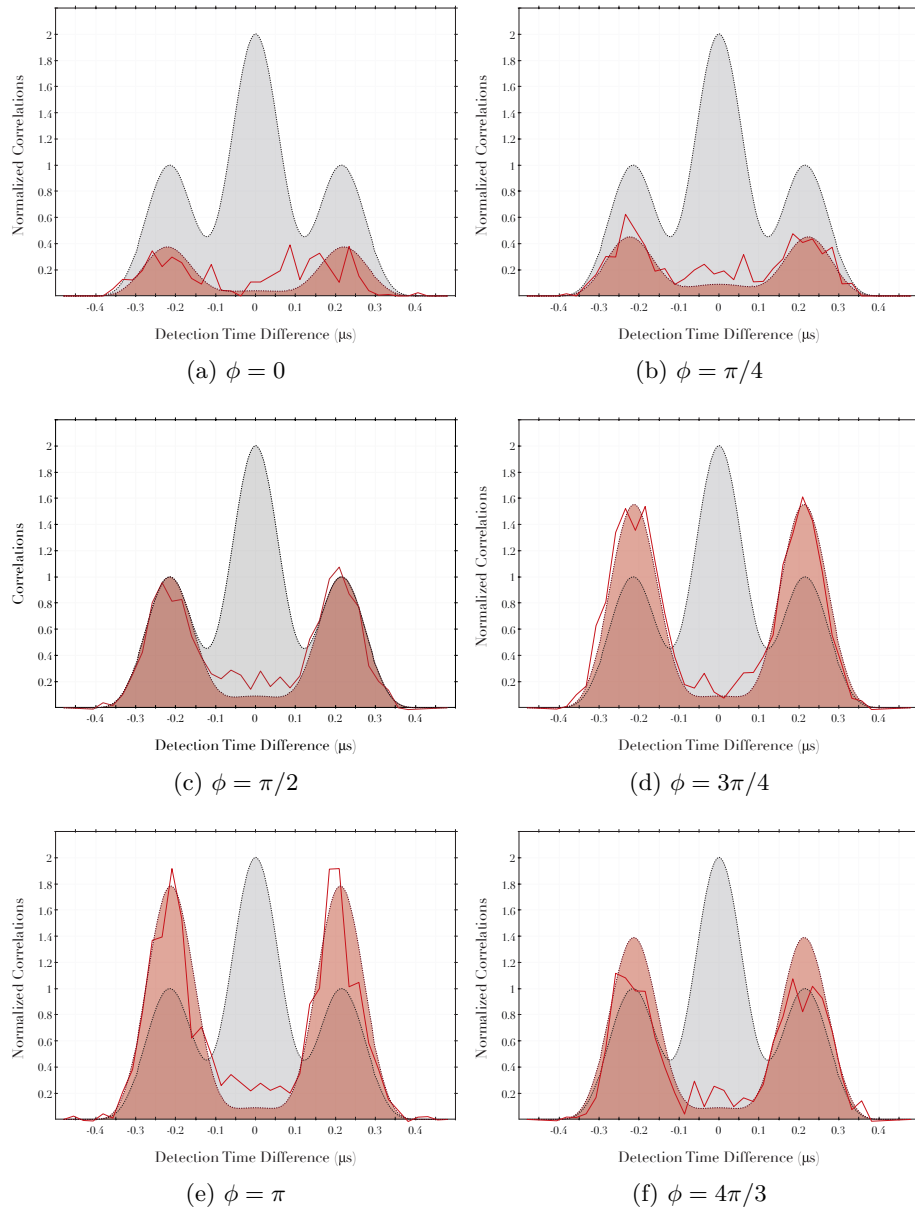


Figure 5.10: HOM interference patterns for photons with a phase shift: the time resolved correlations for twin-peaked photons with a relative phase shift of  $\phi$  between the first and second peaks are shown (red). The theoretical plots of the expected correlations for our system ( $0.48 \mu\text{s}$  coherence time, and a slight mismatch in polarization) are also shown (red shading) along with the perpendicular polarisation case (grey), these are not fits to the data but are simply included for ease of comprehension.

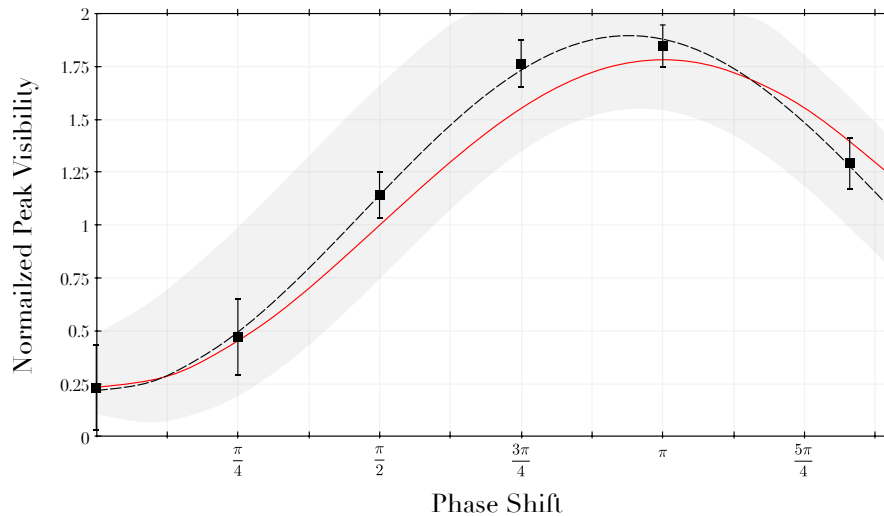


Figure 5.11: Peak visibility versus applied phase shift. The observed peak visibility normalised to the perpendicular case is shown along with the expected dependence (red) and a theoretical fit (dash) with 95% confidence bounds (grey shading). The visibility does not span the full  $0 \rightarrow 2$  range due to the inherent coherence time of the experiment.

in Linear Optical Quantum Computing (LOQC) is dual-rail entanglement [152–154]; a single photon incident on a 50:50 beam-splitter will be split between the two output ports creating a non-separable state of the form,

$$|\Psi\rangle = \frac{1}{\sqrt{2}}(|10\rangle + |01\rangle). \quad (5.18)$$

This is exactly the form of a twin-peak photon if one considers the time-resolved detection, i.e. a detector click in the time range  $0 < t < T_{ph}/2$  corresponds to  $|10\rangle$  and a click in the range  $T_{ph}/2 > t > T_{ph}$  corresponds to  $|01\rangle$ . The advantage of our scheme over a comparable qubit using multi-rail entanglement is the scaling ability. If one would like to increase from a dual-rail to triple-rail state, i.e. to produce the  $W$ -state

$$|\Psi\rangle = |W\rangle = \frac{1}{\sqrt{3}}|100\rangle + |010\rangle + |001\rangle, \quad (5.19)$$

using multi-rail entanglement, a network of two beam-splitters comprising of a 2:1 followed by a 50:50 is required. With our scheme however, all that is necessary is to change a single line of computer code to apply a STIRAP pulse which creates three peaks rather than two. There is also a significant advantage in the overhead of detectors, with multi-rail entanglement one requires a detector on each rail, whereas with the extra time resolution one only requires two detectors, irrespective of the size of the state. An arbitrary phase can also be applied to each time-bin individually to produce the state,

$$|\Psi\rangle = e^{i\phi_1}|100\rangle + e^{i\phi_2}|010\rangle + e^{i\phi_3}|001\rangle. \quad (5.20)$$

### 5.5.1 *Time-binned Qubit*

In order to display the physics of the system in a standard form it is possible to draw the quantum circuit for the interference of the time-binned photons (Figure 5.12). We have two photons, each existing in both time-bin 1 and 2, overlapped on a beam-splitter with detectors A and B. The quantum circuit for this situation is considered in two parts, a circuit which is realised inside the cavity to produce the photons (this involves changing the amplitude and phase of the two time-bins), and an external circuit formed of two ‘virtual’ beam-splitters and four ‘virtual’ detectors, which are just the two real detectors used at different times. A truth table can be drawn up to convert the expected ‘virtual’ detector clicks to the clicks of the real detectors.

In order to obtain the cross correlations of these ‘virtual’ detectors we return to the interference patterns shown in Section 5.4. These can be thought of as the sum of the four possible detector cross-correlations,  $C_{1,2}$ ,  $C_{3,4}$  and  $C_{1,4}$ ,  $C_{2,3}$ ; the individual correlations for both perpendicularly polarized photons and parallel polarized photons with a  $\phi = \pi$  phase shift are shown

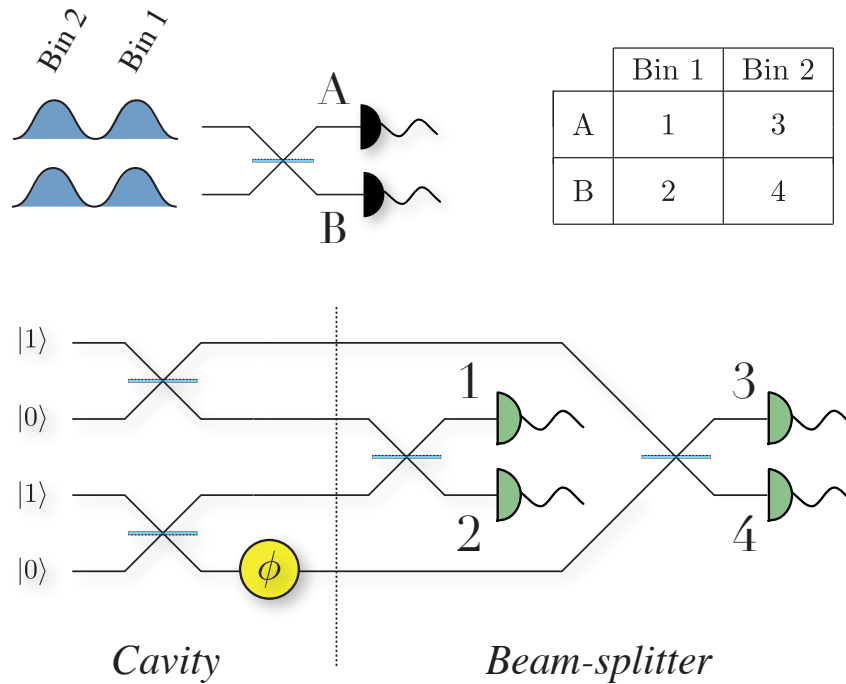


Figure 5.12: Equivalent photonic circuits: the emission of two twin-peak photons and their subsequent time-resolved overlap on a beam-splitter can be represented as a ‘rail-entanglement’-type quantum circuit. Real time-resolved detector clicks can be converted to the virtual detectors using the displayed truth-table.

in Figure 5.13. The full time-resolved correlations - which depend strongly on the photon shape - can be summed and normalised, to give the relative correlations between the virtual detectors (Figures 5.13); in essence we have returned to the time-binned HOM situation of Section 5.1.

### 5.5.2 Fidelity and Density Matrix Reconstruction

We can now use the time-binned correlation data described in the previous section to reconstruct the density matrix of the incident photons, and thus determine how well we can prepare the individual quantum states. The state vector for a twin-peak photon with a phase shift  $\phi$  can be written as

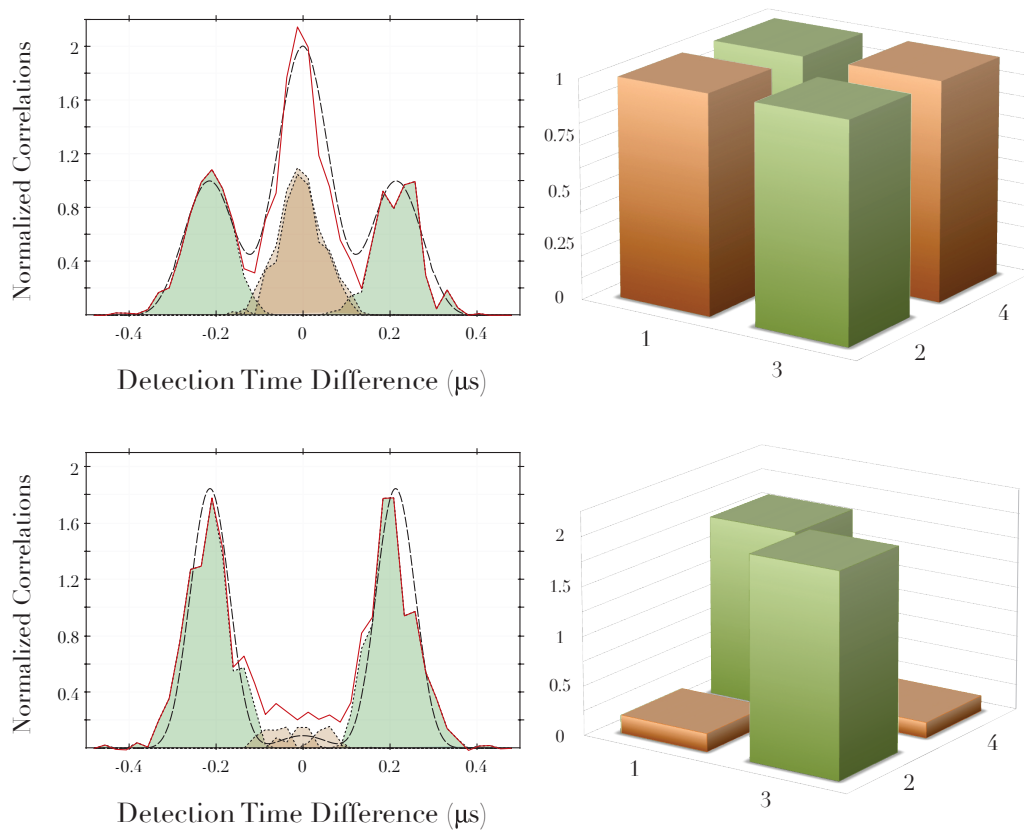


Figure 5.13: The correlations from the time-resolved HOM interference can be split into cases where both detectors fire in the same time-bin (brown), or in successive time-bins (green). The continuous signal (left) can then be simplified by comparing the total number of correlations in the four possible cases (right). The upper plots are for perpendicularly polarized photons and the lower for parallel photons with a  $\phi = \pi$  phase shift.

$|\Psi\rangle = \frac{1}{\sqrt{2}}(A|10\rangle + Be^{i\phi}|01\rangle)$ , where A and B are the amplitudes of bins 1 and 2 respectively. The density matrix of this photon is therefore,

$$\rho = 0.5 \cdot \begin{pmatrix} A^2 & D \cdot AB e^{i\phi} \\ D \cdot AB e^{-i\phi} & B^2 \end{pmatrix}. \quad (5.21)$$

The values along the diagonal signify the relative occupancy of the two time-bins and are normalised to  $\text{Tr}(\rho) = 1$ , whereas the magnitude of the

off-diagonal terms relate to the coherence of the state;  $D = 1$  implies that the state is completely coherent, and  $D = 0$  implies it is completely incoherent.

The diagonal terms can be determined from the number of correlations occurring in the same time-bin, i.e the correlations  $C_{1,2}$  and  $C_{3,4}$ . As there should be no correlations for perfect parallel polarized photons, we use the correlations from the perpendicular photons to determine these values. The off-diagonal terms are slightly more difficult as we cannot easily differentiate between a phase shift and decoherence. If we were to detect a normalised number of correlations  $C_{1,4} = 1$ , this could either be due to a phase-shift of  $\phi = \pi/2$ , or to a high level of decoherence in the state. In theory it should be possible to use the correlations  $C_{1,2}$  and  $C_{3,4}$  to differentiate between the effects of the phase shift and the decoherence, however this effect can be small as can be seen by comparing Figure 5.2b and Figure 5.8a.

Instead, we make the assumption - justified using the results shown in Figure 5.11 - that the applied phase shift is exact and that any deviation of off-diagonal terms from the expected value is purely due to the limited coherence time. A further justification that the applied phase shift is exact was provided by the HOM measurement of two photons which both had a  $\phi = \pi$  phase shift applied to the second time-bin. It was not possible to observe any difference between this HOM signal and that observed with two  $\phi = 0$  photons. The difference between the observed and expected number of correlations - and hence the off-diagonal terms - is therefore,

$$\rho(1, 2) = \rho(2, 1) = \frac{1}{2} \left( 1 - \left| \operatorname{Re}(e^{i\phi}) + [(C_{1,4} + C_{2,3})/2 - 1] \right| \right) AB e^{i\phi}, \quad (5.22)$$

where  $C_{i,j}$  is the number of correlations normalized to the perpendicularly polarized case  $C_{i,j}|_{\perp} = 1$ . We can therefore reconstruct the density matrix of the photons, which in the  $\phi = \pi$  case is,

$$\sigma = 0.5 \cdot \begin{pmatrix} 1.01 & -0.85 \\ -0.85 & 0.99 \end{pmatrix}. \quad (5.23)$$

### 5.5.3 Fidelity

A useful measure of the how well a state has been prepared is the Fidelity, the overlap of the measured density matrix  $\sigma$  with the density matrix of a desired reference  $\rho$ . A Fidelity of  $F = 0$  implies that  $\sigma$  is orthogonal to  $\rho$ , whereas  $F = 1$  is obtained if the states are identical. If the reference is maximally entangled a Fidelity of  $F > 0.5$  implies that entanglement is present in the measured state. The Fidelity is found using the expression,

$$F(\hat{\rho}, \hat{\sigma}) = \text{Tr}\left(\sqrt{\sqrt{\hat{\rho}}\hat{\sigma}\sqrt{\hat{\rho}}}\right)^2. \quad (5.24)$$

and a value of  $F = 0.93$  was obtained for the  $\phi = \pi$  photon.

### 5.5.4 Qudit Generation

Whilst we have shown that it is possible to use time-bin encoding to represent a qubit, the versatility of the photon generation process means that we are not limited to a twin-peak photon, we can scale the system up adding extra time-bins to the photon, each with their own amplitude and phase - a necessary step in fulfilling the DiVencenzo criteria[37]. To demonstrate this scaling ability we have produced triple- and quadruple- peak photons, corresponding to the states:

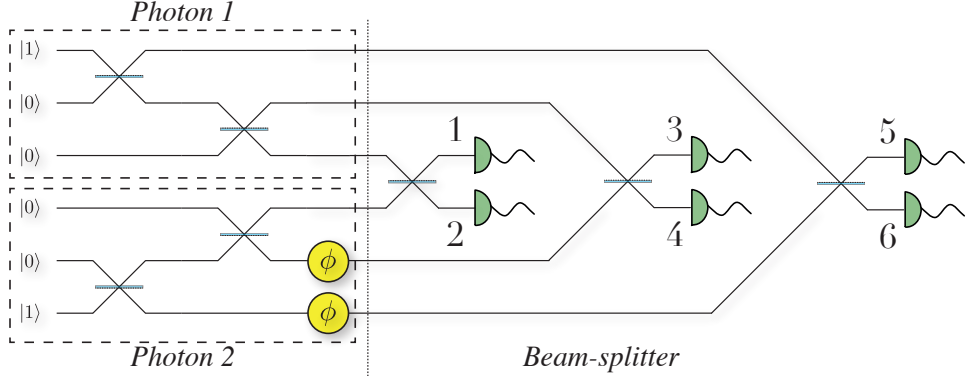


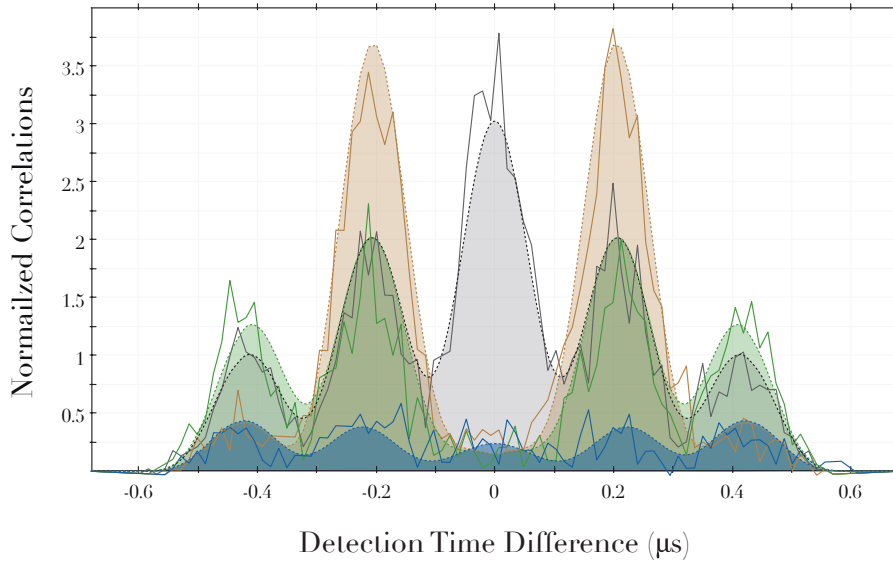
Figure 5.14: Triple-peak HOM: by increasing the number of time-bins of the emitted photons from two to three the quantum circuit substantially increases in size. There are now seven beam-splitters and six detectors in the virtual setup whilst the real experimental apparatus remains unchanged.

$$|\Psi\rangle = |100\rangle + e^{i\phi_1}|010\rangle + e^{i\phi_2}|001\rangle, \quad (5.25)$$

$$|\Psi\rangle = |1000\rangle + e^{i\phi_1}|0100\rangle + e^{i\phi_2}|0010\rangle + e^{i\phi_3}|0001\rangle, \quad (5.26)$$

The circuit which is used to construct and measure the qutrit is shown in Figure 5.14, note that although we have not changed our physical apparatus at all the ‘virtual’ circuit has expanded and we are now simulating six detectors using only the two which are bolted to our laser table. The correlations for the triple-peak photon are shown in Figure 5.15, both as a time-resolved Hong-Ou-Mandel and as the correlations between the six ‘virtual’ detectors.

The data for the quad-peak photon ququad (Figure 5.16) were only taken in the weeks immediately prior to the submission of this thesis and so there was insufficient time to obtain lots of beautiful results. We hope however that the data that have been presented are clear enough to demonstrate the technique.



(a) Time-resolved HOM for triple-peak photons

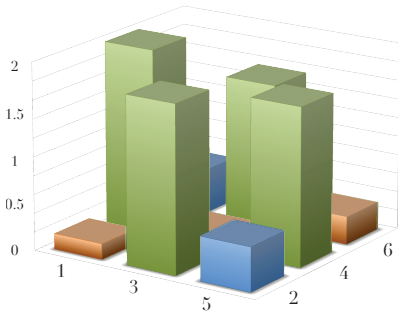
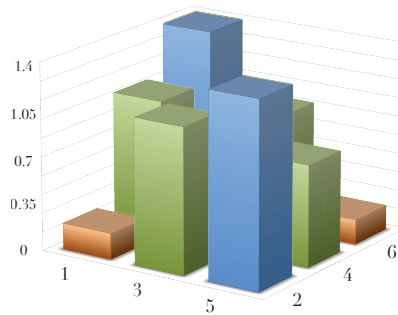
(b)  $\phi_1 = \pi$ (c)  $\phi_1 = \pi/2, \phi_2 = \pi$ 

Figure 5.15: HOM interference for triple-peak photons of defined phase: the upper plot shows the time-resolved correlations for photons with perpendicular polarisation (grey) and parallel polarized photons (blue) with a phase shift in the second time-bin of  $\phi_1 = \pi$  (orange) and with phase shifts of  $\phi_1 = \pi/2$  in the second and  $\phi_2 = \pi$  in the final time-bins (green). The correlations of the virtual detections are shown in the lower plots. Correlations are shown for the same time-bins (brown), successive time-bins (light green) and those separated by a time-bin (light blue).

## 5.6 EXPERIMENTALLY REALIZEABLE CIRCUITS

It is possible to make ever more complex qudits but there is perhaps more value in setting out the general limits on what type of circuits can be

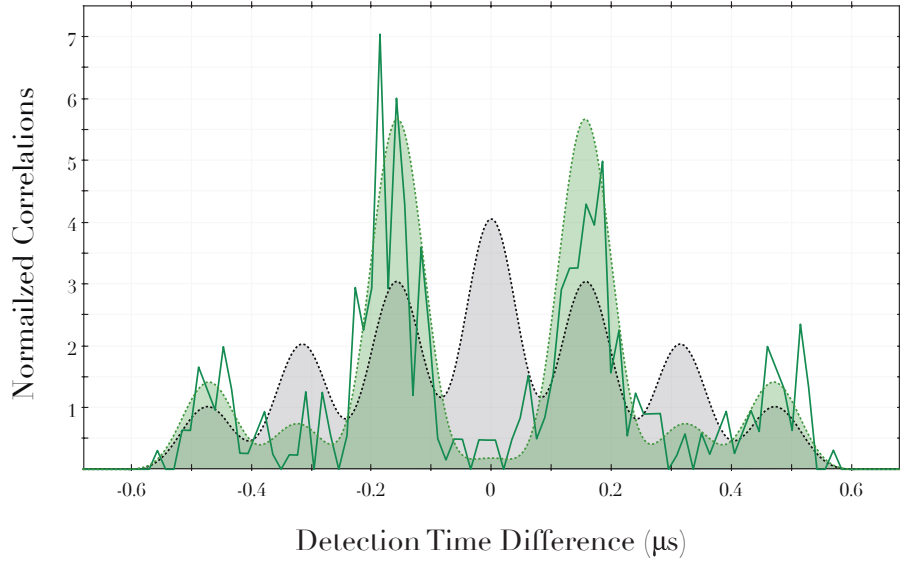


Figure 5.16: Time-resolved HOM for quad-peak photons with a phase-shift of  $\phi = \pi$  in the second and fourth time-bins (green). A theoretical fit (green shading) is shown along with the perpendicular reference (grey).

constructed; both internally - during the production process, and externally - using linear optics.

### 5.6.1 *Intra-Cavity Circuits*

The set of possible intra-cavity circuits is defined by the properties explored in this thesis - namely the amplitude, frequency and phase - as well as control over the photon's polarisation. (We have not been able to demonstrate polarisation control as the line-width of our cavity is too large to resolve the atom's  $m_F$  sub-levels - a necessary experimental condition - however it has been demonstrated elsewhere [112].) One can think of the photon as being comprised of an arbitrary number of time-bins, each one with an arbitrary amplitude, phase, and frequency and polarisation. This control can only be exerted sequentially however, as immediately after the photon has been created it leaks out of the cavity. Using the notation of Figure 5.17 this

means that we can only interact rails with their nearest neighbours - the first rail can never interact with the third.

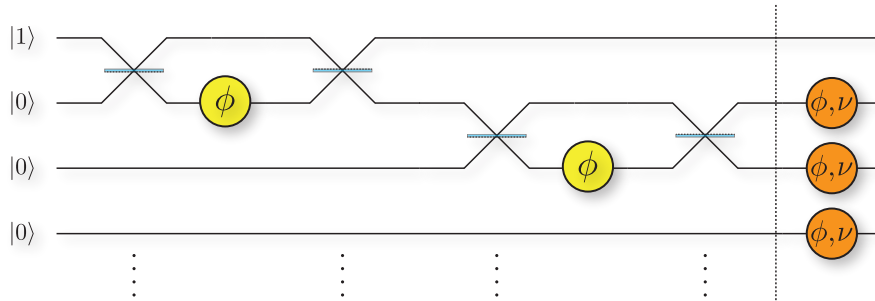


Figure 5.17: Quantum circuit for photon generation: The photon emission process can be thought of as a set of sequential Mach-Zender interferometers distributing the photon amongst the various rails. The relative-phase and frequency of each rail can be set independently.

Although theoretically one could extend this *ad-infinitum*, in practice this is not possible. The number of time-bins that can be produced is restricted by limits from the type of modulator used to generate the photons (Figure 4.16), and more fundamentally from values of  $\kappa$  and  $g_0$ . These, and the 500 kHz decoherence, will impose an upper limit of perhaps a 10-peak photon that is  $1 \mu\text{s}$  long.

We should also note that the intra-cavity circuit is not fixed, the ‘circuit’ is simply a line of code in the memory of an arbitrary waveform generator. It is quite possible to emit a string of photons each with very different properties, for example a ‘square’ photon, followed by a 3-peak photon with an amplitude ratio between the peaks of 3:2:1, followed by a 3-peak photon of equal amplitudes where the central peak has a  $\pi$  phase shift with respect to the others.

5.6.2 *External Circuits*

We currently have only one limitation on the type of possible external circuit - the time-bins of the photons cannot be re-arranged - beyond this all arrangements of mirrors and beam-splitters are possible. Due to our experimental arrangement we can only impose a time-delay on the entire photon, so that the first time-bin of one photon can only interact with the first time-bin of the next (and so on); this is how we have overlapped the photons to perform Hong-Ou-Mandel interferometry (Section 3.6.2).

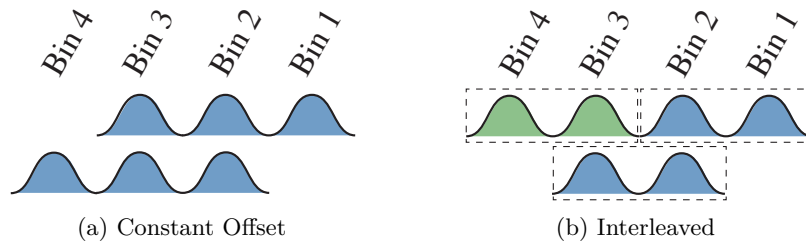


Figure 5.18: Overlap of the emitted photons: with the current experimental arrangement we can only be overlapped perfectly (Figure 3.20) or with a constant offset (a). A sequential offset would allow us to interleave a string of photons (b).

A slight variation on this is to change the timings of the photon emission (Section 3.6.2) so that the photons do not completely overlap but instead are shifted with respect to one another by a constant offset (Figure 5.18a). By controlling the timing in this way we can offset the photons' arrival times and thus interact different time-bins with one another. A simple extension of this with multiple photons would allow us to to mediate a phase relation along long string of photons, (shown in Figure 5.18b). If there is a detection in both time-bin 2 and time-bin 3, then we have succeeded in entangling the photon amplitudes in time-bins 1 and 4 despite the fact that they have never met.

Although our current experimental arrangement precludes overlapping arbitrary time-bins we do not see this as an insurmountable problem. It is envisioned that a phase-stable delay line of  $\Delta t_{delay} = T_{ph}/2$  which could be used to overlap successive time-bins could be implemented using a similar scheme to that used to stabilise the cavity length. The cavity stabilisation beam upon exiting the cavity will be directly coupled into the delay line, this could then be used to measure the phase shifts in the fibre. Feedback could be applied using a fibre-stretcher to keep the fibre phase-stable [155]. During experimental runs this feedback could be paused using a SH circuit (Section 2.3.3) provided the phase stability is sufficient over 20 ms.

### 5.6.3 Feedback

One final type of interaction is the possibility of feeding back the results of a measurement from the external circuit onto the internal circuit. Our photons are long - typically on the order of 100 m - which means that by placing the external circuit close to the cavity one could perform a measurement on the first time-bin of the photon before the second time-bin has been produced.

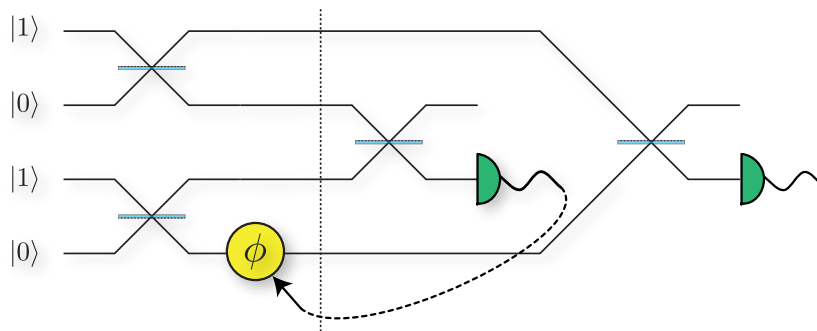


Figure 5.19: Quantum Feedback: due to the temporal length of the photons ( $\mu s$ ) it is possible to make a measurement on the system in the first time-bin and then feed this back onto the STIRAP laser to change the second time-bin. In this case, using the phase, the photons can be steered such that one photon always exits the beam-splitter via the upper port.

If we remove one of the two detectors in our current arrangement, and then put a feedback onto the phase of the second time-bin one could imagine using the effect of the Hong-Ou-Mandel interference to steer a photon out of a particular output port of a beam-splitter (Figure 5.19). In this case we use detector 2 to project the second time-bins of the two photons into a superposition. If we detect a photon at detector 2, we know that by applying a  $\pi$  phase shift we can force the second time-bin of the remaining photon out of the other port of the beam-splitter - correlations between 2 and 4 are impossible (and vice versa). What is peculiar is that this photon has not yet been produced, it is still just a twinkle in the eye of the AWG.

## 5.7 CONCLUSION

Using a time-resolved HOM two-photon interference technique we have demonstrated control over the frequency of the single photons as well as over the relative phase of different parts of a single photon. Two types of frequency control were shown: the first was a simple shift of the entire photon's frequency, whereas the second demonstrated our ability to emit a single photon composed of multiple frequency components. Phase control was implemented by creating a photon that exists in multiple time-bins and imposing a phase relation between them. By varying the phase shift between the time-bins the photon pair correlations simulated all possible spin-statistics from the bosonic  $\phi = 0$  through the anyonic  $0 < \phi < \pi$  to the fermionic  $\phi = \pi$ . Whilst phase changes have been externally applied to a single photon using an EOM [156] and simulated using entanglement [157, 158], this is the first demonstration of creating a photon with an arbitrary phase profile. This was characterized using HOM interference with a photon of fixed phase

which allowed the density matrix of the photon to be reconstructed and the Fidelity of the photon state preparation was found to be  $F = 0.93$ .

Based on these results, the possibility of using these shaped and phase shifted photons to create a simple optical quantum network was discussed. As the effective size of the quantum network is found by the product of the physical size and the number of time-bins used in the photon encoding, very complex arrangements which might be used for quantum simulations seem possible.



## CONCLUSIONS AND OUTLOOK

---

In this thesis the deterministic interaction between a single atom and a single photon has been demonstrated. This type of interaction shows considerable promise for creating quantum networks as it allows for the inter-conversion of static atomic qubits - which have deterministic interactions and long coherence times - and ‘flying’ photonic qubits which can be used to distribute quantum information between distant nodes [99]. In addition to this promise the atom-cavity system has been shown to behave as a possible source for LOQC displaying comparable indistinguishability to the best heralded photon-pair sources whilst increasing the efficiency of photon production.

The photon source has demonstrated the emission of single photons at efficiencies of up to 80% and singleness  $g^{(2)}(0) < 0.06$ . These photons have been shown to be indistinguishable with a two-photon HOM visibility of  $V_{2ph} = 0.87$ . The system dynamics were numerically simulated in order to calculate the required driving pulse to emit a photon of arbitrary shape. Using this technique the shaping of a single photon’s amplitude has been shown, producing simple symmetric shapes ( $\phi = \sin^2(t)$  and ‘square’) as well as more complex shapes (Tower Bridge, Pyramids of Giza, Radcliffe Camera). Finally, using time-resolved HOM it has been shown that both the frequency and the phase of the single photons can be controlled with a fidelity of  $F = 0.93$ , and the possibility of using this to create photonic qubits has been discussed.

The biggest limitation of the experiment, and the main reason why it cannot be considered a truly deterministic photon source, is the probabilistic

loading of an atom into the cavity. The atomic fountain loading scheme results in an arbitrary position of an atom within the cavity mode - causing imperfect knowledge of the atom-cavity coupling, whilst the desire to minimise multi-atom events results in very infrequent atom loading, and thus severely limits the times at which the source can emit photons. The solutions to these problems would be to trap a single atom at the very centre of the cavity mode. However as has been seen in Section 3.7, the electric fields required to trap an atom disturb the atom-cavity interaction and limit the indistinguishability of the source. It is hoped that future progress in the trapping community can overcome these problems and thus bring this atom-cavity source to the deterministic potential that has been shown here.

## 6.1 OUTLOOK

There are two promising routes to extend this work, the first moves directly towards the goal of a quantum network by trying to re-absorb a photon onto an atom in a time-reversal of this thesis, whereas the second seeks to use the current atom-cavity system as a photon source for LOQC.

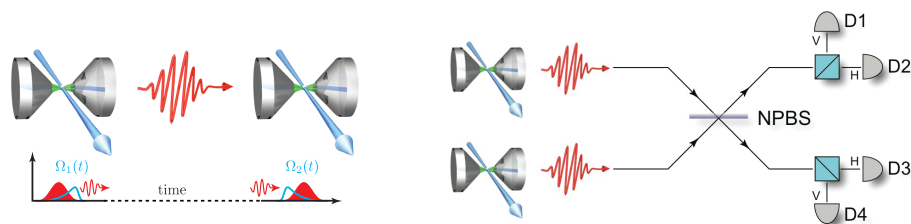


Figure 6.1: Connecting multiple cavities: to interact two atoms located in distant cavities one can either map the state of the atom onto a photon and subsequently map this photon onto the second atom (left), or one can perform a teleportation experiment using a pair of photons entangled with the two atoms (right).

### 6.1.1 A Network of Multiple Cavities

There are two distinct methods for transferring quantum information between two atoms. The first method is to perform a Bell state teleportation by performing a joint measurement on a pair of photons - one photon from each atom [88]. The second method is to map the state of the first atom onto a photon, transmit it to the second atom and re-absorb it, thus transferring the quantum state to the second atom. This has been demonstrated for weak coherent pulses [117, 118] but as yet never for single photons.

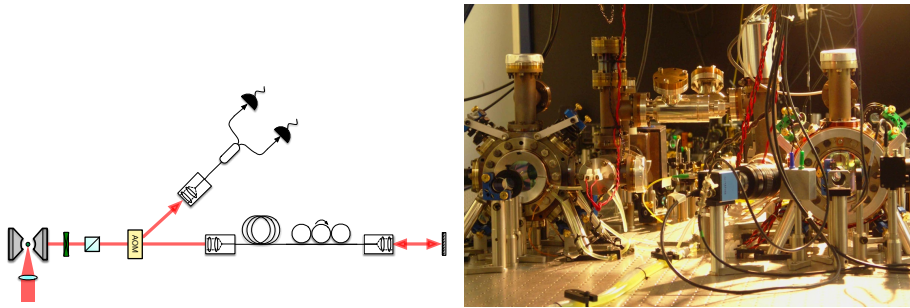


Figure 6.2: Progress towards a network of cavities: initial attempts have been made to map the state of the atom onto a photon and then back onto the same atom using a delay line (left), while a second cavity is being constructed (right).

Before attempting to re-absorb a photon in a second cavity, a sensible first step is to show that it is possible to re-absorb the photon onto the same atom from which it was emitted. Once an atom has emitted a photon it is decoupled from the system and cannot emit again until it is re-pumped to the initial state. If however the emitted photon is re-absorbed then it will coherently transfer the population of the atom back to the initial state and another photon emission can occur. It is this re-emission that is proof that the re-absorption took place.

Our initial attempts to do this (using the theory presented in [159] and the apparatus in Figure 6.2) have been unsuccessful - but show promise. We have implemented a beam steering apparatus with an AOM and can observe photons that are being sent back towards the cavity bouncing off the cavity mirror and then on to the SPCMs, but as yet there is too much noise to be able to observe any re-emission of absorbed photons.

We would also like to show that photons emitted from separate sources are indistinguishable and eventually to perform a teleportation experiment between two cavities. To this end we have started the construction of a second system (Figure 6.2) and have produced a MOT and atomic fountain, but time pressure removed the possibility of building a second cavity.

### 6.1.2 A Source of Photons for LOQC

The second, and perhaps more immediately fruitful, extension of this work is to build on the work shown in Section 5 to implement a simple optical quantum network which combines the atom-cavity photon source with integrated photonic circuits (Figure 6.3).

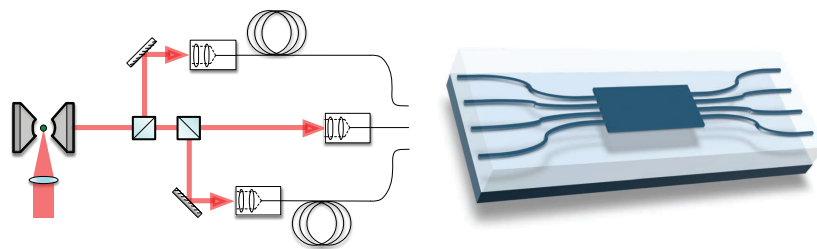


Figure 6.3: Using the atom-cavity photon source for LOQC: It is hoped that we will be able to combine this photon source with waveguide quantum circuits. The deterministic nature of our photon source, along with the time-multiplexing, should enable complex LOQC simulations to be performed.

With the inclusion of multiple delay-lines to increase the number of photons which are simultaneously input to a quantum network, the potential of a photon source which deterministically provides photons in arbitrary quantum states is very exciting. Recent work using photonic networks and conventional photon sources has been very successful and the increase in complexity that seems possible with the photon source demonstrated here should allow for significantly more complex quantum simulations.

It is hoped that in the coming years atom-cavity systems such as this can fulfil some of their enormous promise and enable scaleable quantum networks to advance the discovery of as yet unimagined physics.



## BIBLIOGRAPHY

---

- [1] Whitaker, A. *Einstein, Bohr and the quantum dilemma . From Quantum Theory to Quantum Information* (Cambridge University Press, 2006), 2 edn.
- [2] Hu, Z. & Kimble, H. Observation of a single atom in a magneto-optical trap. *Opt. Lett.* **19**, 1888–1890 (1994).
- [3] Cohen-Tannoudji, C. Nobel lecture: The manipulation of neutral particles. *Rev.Mod.Phys.* **70**, 707 (1998).
- [4] Khudaverdyan, M. *et al.* Controlled insertion and retrieval of atoms coupled to a high-finesse optical resonator. *New J. Phys.* **10**, 073023 (2008).
- [5] Neuhauser, W., Hohenstatt, M., Toschek, P. & Dehmelt, H. Localized visible Ba<sup>+</sup> mono-ion oscillator. *Phys Rev A* **22**, 1137–1140 (1980).
- [6] Paul, W. Electromagnetic traps for charged and neutral particles. *Reviews of Modern Physics* **62**, 531–540 (1990).
- [7] van Dyck, R., Ekstrom, P. & Dehmelt, H. Axial, magnetron, cyclotron and spin-cyclotron-beat frequencies measured on single electron almost at rest in free space (geonium). *Nature* **262**, 776–777 (1976).
- [8] Dehmelt, H. Experiments with an isolated subatomic particle at rest. *Reviews of Modern Physics* **62**, 525–530 (1990).
- [9] Kimble, H., Dagenais, M. & Mandel, L. Photon antibunching in resonance fluorescence. *Phys Rev Lett* **39**, 691–695 (1977).
- [10] Haroche, S. *et al.* Seeing a single photon without destroying it. *Nature* **400**, 239–242 (1999).
- [11] Haroche, S. & Raimond, J.-M. *Exploring the Quantum. Atoms, Cavities, and Photons* (Oxford University Press, 2010), 1 edn.
- [12] Davies, P. C. W. & Brown, J. R. *The Ghost in the Atom* (Cambridge University Press, 2008).
- [13] Einstein, A., Podolsky, B. & Rosen, N. Can Quantum-Mechanical Description of physical reality be considered complete? *Phys. Rev.* **47**, 777–780 (1935).
- [14] Bell, J. S. On the Einstein-Podolsky-Rosen paradox. *Physics* **1**, 195–200 (1964).

- [15] Bell, J. On the Problem of Hidden Variables in Quantum Mechanics. *Reviews of Modern Physics* **38**, 447–452 (1966).
- [16] Aspect, A., Dalibard, J. & Roger, G. Experimental Test of Bell's Inequalities Using Time-Varying Analyzers. *Phys Rev Lett* **49**, 1804–1807 (1982).
- [17] Tapster, P., Rarity, J. & Owens, P. Violation of Bell's Inequality over 4 km of Optical Fiber. *Phys Rev Lett* **73**, 1923–1926 (1994).
- [18] Weihs, G., Jennewein, T., Simon, C., Weinfurter, H. & Zeilinger, A. Violation of Bell's Inequality under Strict Einstein Locality Conditions. *Phys Rev Lett* **81**, 5039–5043 (1998).
- [19] Naik, A. *et al.* Cooling a nanomechanical resonator with quantum back-action. *Nature* **443**, 193–196 (2006).
- [20] O'Connell, A. D. *et al.* Quantum ground state and single-phonon control of a mechanical resonator. *Nature* **464**, 697–703 (2010).
- [21] Nairz, O., Arndt, M. & Zeilinger, A. Quantum interference experiments with large molecules. *American Journal of Physics* **71**, 319–325 (2003).
- [22] Gisin, N., Ribordy, G., Tittel, W. & Zbinden, H. Quantum cryptography. *Reviews of Modern Physics* **74**, 145–195 (2002).
- [23] Ladd, T. D. *et al.* Quantum computers. *Nature* **464**, 45–53 (2010).
- [24] Nielson, M. & Chaung, I. *Quantum Computation and Quantum Information* (Cambridge University Press, Cambridge, 2000).
- [25] Deutsch, D. & Jozsa, R. Rapid solution of problems by quantum computation. *Proceedings of the Royal Society A: Mathematical, Physical and Engineering Sciences* 553–558 (1992).
- [26] Grover, L. Quantum Computers Can Search Arbitrarily Large Databases by a Single Query. *Phys Rev Lett* **79**, 4709–4712 (1997).
- [27] Grover, L. Quantum mechanics helps in searching for a needle in a haystack. *Phys Rev Lett* **79**, 325–328 (1997).
- [28] Shor, P. Polynomial-time algorithms for prime factorization and discrete logarithms on a quantum computer. *Siam J Comput* **26**, 1484–1509 (1997).
- [29] Deutsch, D. Quantum Computational Networks. *Proceedings of the Royal Society A: Mathematical, Physical and Engineering Sciences* **425**, 73–90 (1989).
- [30] Deutsch, D. Quantum Theory, the Church-Turing Principle and the Universal Quantum Computer. *Proceedings of the Royal Society A: Mathematical, Physical and Engineering Sciences* **400**, 97–117 (1985).

- [31] Lloyd, S. Universal Quantum Simulators. *Science* **273**, 1073–1078 (1996).
- [32] Barreiro, J. T. *et al.* An open-system quantum simulator with trapped ions. *Nature* **470**, 486–491 (2011).
- [33] Lanyon, B. P. *et al.* Universal Digital Quantum Simulation with Trapped Ions. *Science* **334**, 57–61 (2011).
- [34] Gerritsma, R. *et al.* Quantum simulation of the Dirac equation. *Nature* **463**, 68–71 (2010).
- [35] Gerritsma, R. *et al.* Quantum Simulation of the Klein Paradox with Trapped Ions. *Phys Rev Lett* **106**, 060503 (2011).
- [36] Simon, J. *et al.* Quantum simulation of antiferromagnetic spin chains in an optical lattice. *Nature* **472**, 307–312 (2011).
- [37] DiVincenzo, D. The Physical Implementation of Quantum Computation. *Fortschritte der Physik* **48**, 771–783 (2000).
- [38] Saffman, M., Walker, T. G. & Molmer, K. Quantum information with Rydberg atoms. *Reviews of Modern Physics* **82**, 2313–2363 (2010).
- [39] Ryabtsev, I., Tretyakov, D. & Beterov, I. Applicability of Rydberg atoms to quantum computers. *Journal of Physics B: Atomic, Molecular and Optical Physics* **38**, S421–S436 (2005).
- [40] Gaetan, A. *et al.* Observation of collective excitation of two individual atoms in the Rydberg blockade regime. *Nature Physics* **5**, 115–118 (2009).
- [41] Urban, E. *et al.* Observation of Rydberg blockade between two atoms. *Nature Physics* **5**, 110–114 (2009).
- [42] Younge, K. C., Knuffman, B., Anderson, S. E. & Raithel, G. State-Dependent Energy Shifts of Rydberg Atoms in a Ponderomotive Optical Lattice. *Phys Rev Lett* **104**, 173001 (2010).
- [43] Loss, D. & Di Vincenzo, D. P. Quantum Computation with Quantum Dots. *Phys Rev A* **57**, 120–126 (1998).
- [44] Imamoglu, A. *et al.* Quantum Information Processing Using Quantum Dot Spins and Cavity QED. *Phys Rev Lett* **83**, 4204–4207 (1999).
- [45] Kiraz, A., Atatüre, M. & Imamoglu, A. Quantum-dot single-photon sources: Prospects for applications in linear optics quantum-information processing. *Phys Rev A* **69**, 032305 (2004).
- [46] Berezovsky, J. *et al.* Nondestructive Optical Measurements of a Single Electron Spin in a Quantum Dot. *Science* **314**, 1916–1920 (2006).

- [47] Morton, J. J. L., McCamey, D. R., Eriksson, M. A. & Lyon, S. A. Embracing the quantum limit in silicon computing. *Nature* **479**, 345–353 (2011).
- [48] Buluta, I. & Nori, F. Quantum Simulators. *Science* **326**, 108–111 (2009).
- [49] Bouchiat, V., Vion, D., Joyez, P., Esteve, D. & Devoret, M. Quantum coherence with a single Cooper pair. *Phys Scripta* **T76**, 165–170 (1998).
- [50] Wallraff, A. *et al.* Strong coupling of a single photon to a superconducting qubit using circuit quantum electrodynamics. *Nature* **431**, 162–167 (2004).
- [51] Steffen, M. Measurement of the Entanglement of Two Superconducting Qubits via State Tomography. *Science* **313**, 1423–1425 (2006).
- [52] Leek, P. J. *et al.* Using sideband transitions for two-qubit operations in superconducting circuits. *Phys Rev B* **79**, 180511 (2009).
- [53] Brouri, R., Beveratos, A., Poizat, J.-P. & Grangier, P. Photon anti-bunching in the fluorescence of individual color centers in diamond. *Opt. Lett.* **25**, 1294–1296 (2000).
- [54] Dutt, M. V. G. *et al.* Quantum Register Based on Individual Electronic and Nuclear Spin Qubits in Diamond. *Science* **316**, 1312–1316 (2007).
- [55] Neumann, P. *et al.* Multipartite entanglement among single spins in diamond. *Science* **320**, 1326–1329 (2008).
- [56] Balasubramanian, G. *et al.* Ultralong spin coherence time in isotopically engineered diamond. *Nature Materials* **8**, 383–387 (2009).
- [57] Kurtsiefer, C. *et al.* Quantum cryptography: A step towards global key distribution. *Nature* **419**, 450–450 (2002).
- [58] Ursin, R. *et al.* Entanglement-based quantum communication over 144 km. *Nature Physics* **3**, 481–486 (2007).
- [59] Freedman, S. J. & Clauser, J. F. Experimental test of local hidden-variable theories. *Phys Rev Lett* **28**, 938–941 (1972).
- [60] Ou, Z. & Mandel, L. Violation of Bell’s inequality and classical probability in a two-photon correlation experiment. *Phys Rev Lett* **61**, 50–53 (1988).
- [61] Stucki, D., Gisin, N., Guinnard, O., Ribordy, G. & Zbinden, H. Quantum key distribution over 67 km with a plug&play system. *New J. Phys.* **4**, 41.4–41.8 (2002).

- [62] Takesue, H. *et al.* Differential phase shift quantum key distribution experiment over 105 km fibre. *New J. Phys.* **7**, 232 (2005).
- [63] Gobby, C., Yuan, Z. L. & Shields, A. J. Quantum key distribution over 122 km of standard telecom fiber. *Appl. Phys. Lett.* **84**, 3762–3764 (2004).
- [64] Knill, E., Laflamme, R. & Milburn, G. A scheme for efficient quantum computation with linear optics. *Nature* **409**, 46–52 (2001).
- [65] Ralph, T., White, A., Munro, W. & Milburn, G. Simple scheme for efficient linear optics quantum gates. *Phys Rev A* **65**, 012314 (2002).
- [66] Nielsen, M. A. Optical Quantum Computation Using Cluster States. *Phys Rev Lett* **93**, 040503 (2004).
- [67] Ralph, T., Hayes, A. & Gilchrist, A. Loss-Tolerant Optical Qubits. *Phys Rev Lett* **95**, 100501 (2005).
- [68] O’Brien, J. L. Optical Quantum Computing. *Science* **318**, 1567–1570 (2007).
- [69] O’Brien, J. L., Pryde, G. J., White, A. G., Ralph, T. C. & Branning, D. Demonstration of an all-optical quantum controlled-NOT gate. *Nature* **426**, 264–267 (2003).
- [70] Langford, N. *et al.* Demonstration of a Simple Entangling Optical Gate and Its Use in Bell-State Analysis. *Phys Rev Lett* **95**, 210504 (2005).
- [71] Pittman, T., Fitch, M., Jacobs, B. & Franson, J. Experimental controlled-NOT logic gate for single photons in the coincidence basis. *Phys Rev A* **68**, 032316 (2003).
- [72] Sanaka, K., Jennewein, T., Pan, J.-W., Resch, K. & Zeilinger, A. Experimental Nonlinear Sign Shift for Linear Optics Quantum Computation. *Phys Rev Lett* **92**, 017902 (2004).
- [73] Gasparoni, S., Pan, J.-W., Walther, P., Rudolph, T. & Zeilinger, A. Realization of a Photonic Controlled-NOT Gate Sufficient for Quantum Computation. *Phys Rev Lett* **93**, 020504 (2004).
- [74] Lanyon, B. *et al.* Experimental Demonstration of a Compiled Version of Shor’s Algorithm with Quantum Entanglement. *Phys Rev Lett* **99**, 250505 (2007).
- [75] Lu, C.-Y., Browne, D., Yang, T. & Pan, J.-W. Demonstration of a Compiled Version of Shor’s Quantum Factoring Algorithm Using Photonic Qubits. *Phys Rev Lett* **99**, 250504 (2007).
- [76] Anderlini, M. *et al.* Controlled exchange interaction between pairs of neutral atoms in an optical lattice. *Nature* **448**, 452–456 (2007).

- [77] Mandel, O. *et al.* Controlled collisions for multi-particle entanglement of optically trapped atoms. *Nature* **425**, 937–940 (2003).
- [78] Leibfried, D., Blatt, R., Monroe, C. & Wineland, D. Quantum dynamics of single trapped ions. *Reviews of Modern Physics* **75**, 281–324 (2003).
- [79] Blatt, R. & Wineland, D. Entangled states of trapped atomic ions. *Nature* **453**, 1008–1015 (2008).
- [80] Monz, T. *et al.* 14-Qubit Entanglement: Creation and Coherence. *Phys Rev Lett* **106**, 130506 (2011).
- [81] Cirac, J. & Zoller, P. Quantum Computations with Cold Trapped Ions. *Phys Rev Lett* **74**, 4091–4094 (1995).
- [82] Monroe, C., Meekhof, D., King, B., Itano, W. & Wineland, D. Demonstration of a Fundamental Quantum Logic Gate. *Phys Rev Lett* **75**, 4714–4717 (1995).
- [83] Leibfried, D. *et al.* Experimental demonstration of a robust, high-fidelity geometric two ion-qubit phase gate. *Nature* **422**, 412–415 (2003).
- [84] Chiaverini, J. Implementation of the Semiclassical Quantum Fourier Transform in a Scalable System. *Science* **308**, 997–1000 (2005).
- [85] Home, J. P. *et al.* Complete Methods Set for Scalable Ion Trap Quantum Information Processing. *Science* **325**, 1227–1230 (2009).
- [86] Barrett, M. D. *et al.* Deterministic quantum teleportation of atomic qubits. *Nature* **429**, 737–739 (2004).
- [87] Riebe, M. *et al.* Deterministic quantum teleportation with atoms. *Nature* **429**, 734–737 (2004).
- [88] Olmschenk, S. *et al.* Quantum teleportation between distant matter qubits. *Science* **323**, 486–489 (2009).
- [89] Julsgaard, B., Sherson, J., Cirac, J. I., Fiurášek, J. & Polzik, E. S. Experimental demonstration of quantum memory for light. *Nature* **432**, 482–486 (2004).
- [90] Reim, K. F. *et al.* Towards high-speed optical quantum memories. *Nature Photon* **4**, 218–221 (2010).
- [91] Langer, C. *et al.* Long-lived qubit memory using atomic ions. *Phys Rev Lett* **95**, 60502 (2005).
- [92] Cohen-Tannoudji, C., Dupont-Roc, J. & Grynberg, G. *Photons and Atoms*. Introduction to Quantum Electrodynamics (Wiley, 1997).

- [93] Purcell, E. M. Spontaneous Emission Probabilities at Radio Frequencies. *Phys. Rev.* **69**, 681 (1946).
- [94] Jaynes, E. & Cummings, F. Comparison of quantum and semiclassical radiation theories with application to the beam maser. *IEEE Proc.* **51**, 89–109 (1963).
- [95] Law, C. & Eberly, J. Arbitrary Control of a Quantum Electromagnetic Field. *Phys Rev Lett* **76**, 1055–1058 (1996).
- [96] Law, C. K. & Kimble, H. J. Deterministic generation of a bit-stream of single-photon pulses. *Journal of Modern Optics* **44**, 2067–2074 (1997).
- [97] Kuhn, A., Hennrich, M., Bondo, T. & Rempe, G. Controlled generation of single photons from a strongly coupled atom-cavity system. *Appl Phys B-Lasers and Optics* **69**, 373–377 (1999).
- [98] Cirac, J., Zoller, P., Kimble, H. & Mabuchi, H. Quantum State Transfer and Entanglement Distribution among Distant Nodes in a Quantum Network. *Phys Rev Lett* **78**, 3221–3224 (1997).
- [99] Kimble, H. J. The quantum internet. *Nature* **453**, 1023–1030 (2008).
- [100] Duan, L. M., Wang, B. & Kimble, H. J. Robust quantum gates on neutral atoms with cavity-assisted photon scattering. *Phys Rev A* **72**, 032333 (2005).
- [101] Su, C.-H., Greentree, A., Munro, W., Nemoto, K. & Hollenberg, L. High-speed quantum gates with cavity quantum electrodynamics. *Phys Rev A* **78**, 062336 (2008).
- [102] Himsforth, M., Nisbet, P., Dille, J., Langfahl-Klabes, G. & Kuhn, A. EIT-based quantum memory for single photons from cavity-QED. *Appl. Phys. B* **103**, 579 (2011).
- [103] Kuhn, A., Hennrich, M. & Rempe, G. Deterministic Single-Photon Source for Distributed Quantum Networking. *Phys Rev Lett* **89**, 067901 (2002).
- [104] McKeever, J. *et al.* Deterministic generation of single photons from one atom trapped in a cavity. *Science* **303**, 1992–1994 (2004).
- [105] Nussmann, S. *et al.* Submicron positioning of single atoms in a micro-cavity. *Phys Rev Lett* **95**, 173602 (2005).
- [106] Hijlkema, M. *et al.* A single-photon server with just one atom. *Nature Physics* **3**, 253–255 (2007).
- [107] Keller, M., Lange, B., Hayasaka, K., Lange, W. & Walther, H. Continuous generation of single photons with controlled waveform in an ion-trap cavity system. *Nature* **431**, 1075–1078 (2004).

- [108] Pinkse, P. W. H., Fischer, T., Maunz, P. & Rempe, G. Trapping an atom with single photons. *Nature* **404**, 365–368 (2000).
- [109] Fischer, T., Maunz, P., Pinkse, P., Puppe, T. & Rempe, G. Feedback on the Motion of a Single Atom in an Optical Cavity. *Phys Rev Lett* **88**, 163002 (2002).
- [110] Maunz, P. *et al.* Cavity cooling of a single atom. *Nature* **428**, 50–52 (2004).
- [111] Nußmann, S. *et al.* Vacuum-stimulated cooling of single atoms in three dimensions. *Nature Physics* **1**, 122–125 (2005).
- [112] Wilk, T., Webster, S., Specht, H., Rempe, G. & Kuhn, A. Polarization-Controlled Single Photons. *Phys Rev Lett* **98**, 063601 (2007).
- [113] Legero, T., Wilk, T., Kuhn, A. & Rempe, G. Characterization of single photons using two-photon interference. *Advances In Atomic, Molecular, and Optical Physics* **53**, 253–289 (2006).
- [114] Legero, T., Wilk, T., Hennrich, M., Rempe, G. & Kuhn, A. Quantum beat of two single photons. *Phys Rev Lett* **93**, 70503 (2004).
- [115] Legero, T., Wilk, T., Kuhn, A. & Rempe, G. Time-resolved two-photon quantum interference. *Appl Phys B-Lasers and Optics* **77**, 797–802 (2003).
- [116] Wilk, T., Webster, S., Kuhn, A. & Rempe, G. Single-Atom Single-Photon Quantum Interface. *Science* **317**, 488–490 (2007).
- [117] Boozer, A. D., Boca, A., Miller, R., Northup, T. E. & Kimble, H. Reversible State Transfer between Light and a Single Trapped Atom. *Phys Rev Lett* **98**, 193601 (2007).
- [118] Specht, H. P. *et al.* A single-atom quantum memory. *Nature* **473**, 190–193 (2011).
- [119] Kuhn, A. & Ljunggren, D. Cavity-based single-photon sources. *Contemporary Physics* **51**, 289–313 (2010).
- [120] Kuhn, A. & Rempe, G. Optical cavity QED: Fundamentals and application as a single-photon light source. *Proceedings-International School Of Physics Enrico Fermi* **148**, 37–66 (2001).
- [121] Dotsenko, I. *Single atoms on demand for cavity QED experiments*. Ph.D. thesis, Rheinischen Friedrich-Wilhelms-Universität Bonn (2012).
- [122] Bandres, M. A. & Gutiérrez-Vega, J. C. Ince–Gaussian modes of the paraxial wave equation and stable resonators. *JOSA A* **21**, 873–880 (2004).

- [123] Steck, D. A. Rubidium 87 D Line Data (2008). URL <http://steck.us/alkalidata>.
- [124] Black, E. D. An introduction to Pound-Drever-Hall laser frequency stabilization. *American Journal of Physics* **69**, 79–87 (2001).
- [125] Wallner, O., Leeb, W. & Winzer, P. Minimum length of a single-mode fiber spatial filter. *JOSA A* **19**, 2445–2448 (2002).
- [126] Dilley, J. *A Single Photon Source for Quantum Networking*. Ph.D. thesis, Oxford (2012).
- [127] Atutov, S. *et al.* Fast and efficient loading of a Rb magneto-optical trap using light-induced atomic desorption. *Phys Rev A* **67**, 053401 (2003).
- [128] Burchianti, A. *et al.* Light-induced atomic desorption from porous silica. *Europhys Lett* **67**, 983 (2004).
- [129] Smith, D. & Hughes, I. The role of hyperfine pumping in multilevel systems exhibiting saturated absorption. *American Journal of Physics* **72**, 631 (2004).
- [130] Maguire, L., Szilagyi, S. & Scholten, R. High performance laser shutter using a hard disk drive voice-coil actuator. *Rev Sci Instrum* **75**, 3077–3079 (2004).
- [131] Kubanek, A. *et al.* Photon-by-photon feedback control of a single-atom trajectory. *Nature* **462**, 898–901 (2009).
- [132] Brown, R. H. & Twiss, R. Q. Interferometry of the Intensity Fluctuations in Light. I. Basic Theory: The Correlation between Photons in Coherent Beams of Radiation. *Proceedings of the Royal Society A: Mathematical, Physical and Engineering Sciences* **242**, 300–324 (1957).
- [133] Brown, R. H. & Twiss, R. Q. Interferometry of the Intensity Fluctuations in Light II. An Experimental Test of the Theory for Partially Coherent Light. *Proceedings of the Royal Society A: Mathematical, Physical and Engineering Sciences* **243**, 291–319 (1958).
- [134] Grangier, P., Roger, G. & Aspect, A. Experimental-Evidence for a Photon Anticorrelation Effect on a Beam Splitter - a New Light on Single-Photon Interferences. *Europhys Lett* **1**, 173–179 (1986).
- [135] Fox, M. *Quantum Optics - An Introduction* (Oxford University Press, 2006), 1 edn.
- [136] Ljunggren, D. *Entanglement in Quantum Communication*. Ph.D. thesis, Thesis, KTH (2006).

- [137] Hennrich, M., Legero, T., Kuhn, A. & Rempe, G. Photon statistics of a non-stationary periodically driven single-photon source. *New J. Phys.* **6**, 86 (2004).
- [138] Vasilev, G. S., Ljunggren, D. & Kuhn, A. Single photons made-to-measure. *New J. Phys.* **12**, 063024 (2010).
- [139] Hong, C., Ou, Z. & Mandel, L. Measurement of subpicosecond time intervals between two photons by interference. *Phys Rev Lett* **59**, 2044–2046 (1987).
- [140] Collaboration, T. O. *et al.* Measurement of the neutrino velocity with the OPERA detector in the CNGS beam. *arXiv* 1109.4897 (2011).
- [141] Mosley, P. *et al.* Heralded Generation of Ultrafast Single Photons in Pure Quantum States. *Phys Rev Lett* **100**, 133601 (2008).
- [142] Barros, H. G. *et al.* Deterministic single-photon source from a single ion. *New J. Phys.* **11**, 103004 (2009).
- [143] Soeller, C., Cohen, O., Smith, B. J., Walmsley, I. A. & Silberhorn, C. High-performance single-photon generation with commercial-grade optical fiber. *Phys Rev A* **83**, – (2011).
- [144] Parkins, A., Marte, P., Zoller, P., Carnal, O. & Kimble, H. Quantum-state mapping between multilevel atoms and cavity light fields. *Phys Rev A* **51**, 1578–1596 (1995).
- [145] Tan, S. A computational toolbox for quantum and atomic optics. *Journal of Optics B: Quantum and Semiclassical Optics* **1**, 424 (1999).
- [146] Nisbet-Jones, P. B. R., Dille, J., Ljunggren, D. & Kuhn, A. Highly efficient source for indistinguishable single photons of controlled shape. *New J. Phys.* **13**, 3036 (2011).
- [147] Grice, W. P. & Walmsley, I. A. Spectral information and distinguishability in type-II down-conversion with a broadband pump. *Phys Rev A* **56**, 1627 (1997).
- [148] Grice, W. P., Erdmann, R., Walmsley, I. A. & Branning, D. Spectral distinguishability in ultrafast parametric down-conversion. *Physical Review A (Atomic)* **57**, 2289 (1998).
- [149] Keller, T. & Rubin, M. Theory of two-photon entanglement for spontaneous parametric down-conversion driven by a narrow pump pulse. *Phys Rev A* **56**, 1534–1541 (1997).
- [150] Pittman, T. *et al.* Two-photon geometric optics. *Phys Rev A* **53**, 2804–2815 (1996).

- [151] Pittman, T. *et al.* Can two-photon interference be considered the interference of two photons? *Phys Rev Lett* **77**, 1917–1920 (1996).
- [152] Brendel, J., Gisin, N., Tittel, W. & Zbinden, H. Pulsed Energy-Time Entangled Twin-Photon Source for Quantum Communication. *Phys Rev Lett* **82**, 2594–2597 (1999).
- [153] Marcikic, I., de Riedmatten, H., Tittel, W., Zbinden, H. & Gisin, N. Long-distance teleportation of qubits at telecommunication wavelengths. *Nature* **421**, 509–513 (2003).
- [154] de Riedmatten, H. *et al.* Long Distance Quantum Teleportation in a Quantum Relay Configuration. *Phys Rev Lett* **92**, 047904 (2004).
- [155] Marra, G., Margolis, H. S., Lea, S. N. & Gill, P. High-stability microwave frequency transfer by propagation of an optical frequency comb over 50 km of optical fiber. *Opt. Lett.* **35**, 1025 (2010).
- [156] Specht, H. P. *et al.* Phase shaping of single-photon wave packets. *Nature Photon* **3**, 469–472 (2009).
- [157] Sansoni, L. *et al.* Two-Particle Bosonic-Fermionic Quantum Walk via Integrated Photonics. *Phys Rev Lett* **108**, 010502 (2012).
- [158] Matthews, J. C. F. *et al.* Simulating quantum statistics with entangled photons: a continuous transition from bosons to fermions. *arXiv quant-ph*, 1106.1166v1 (2011).
- [159] Dilley, J., Nisbet-Jones, P., Shore, B. W. & Kuhn, A. Single-photon absorption in coupled atom-cavity systems. *Phys Rev A* **85**, 023834 (2012).